Numerical Study of the Dynamics and Sound Generation of a Turbulent Vortex Ring

Thesis by

Hongyu Ran

In Partial Fulfillment of the Requirements

for the Degree of

Doctor of Philosophy

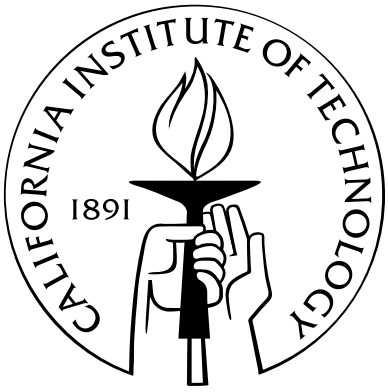

California Institute of Technology

Pasadena, California

2004

(Submitted June 08, 2004)

Acknowledgements

The time I have spent at Caltech was certainly fruitful and enjoyable. Caltech not only opened the door to scientific research, but also broadened my knowledge in many other areas. I feel very grateful to the institute and the people working here.

I would like to thank my advisor, Professor Tim Colonius, for his patience, support and guidance through the years. He has always been available for consultations and inspirations. I want to thank my committee members, Professor T. Colonius, Anthony Leonard, Mory Gharib and Melany Hunt, for their comments and encouragement.

I have enjoyed working with people in our lab. I had fruitful collaboration with Kamran Mohseni during the study of vortex ring formation, and got a lot of help from him on three-dimensional computation. I thank Dr. Takao Suzuki for answering my countless questions, and Michel Tanguay for administrating the computer systems. My numerical simulation is made possible with the computer time provided by CACR and Professor Oscar Bruno's group. I want to thank Mark Bartelt and Chad Schmutzer for their assistance.

I must thank my parents and my sister in China, for their continuous support and encouragement. Most importantly I want to thank my lovely fiance and best friend, Lan Yang, for her unlimited love and confidence in me.

Abstract

In the present study, Direct Numerical Simulations (DNS) of the fully compressible, three-dimensional Navier-Stokes equations are used to generate an axisymmetric vortex ring to which three-dimensional stochastic disturbances are added. The radiated acoustic field is computed directly in the near field, and by solving the wave equation in a spherical coordinate system in the far field.

At high Reynolds number, a vortex ring will undergo an instability to azimuthal waves. The instability produces higher azimuthal modes and induces nonlinear interaction between the modes, and will cause the vortex ring to break down and transition to turbulence. The early stages of the simulation agree well with the linear instability theory. Nonlinear stage of instability, transition, formation of axial flow and streamwise vorticity are analyzed and compared with experimental results. After turbulent transition, the evolution of statistical quantities becomes independent of viscosity and the initial geometry, and the flow become self-similar. The temporal evolution of quantities including total circulation, axial velocity profile, vortex ring displacement and vorticity profile agrees well with the self-similarity law. Turbulent energy spectrum, Reynolds stresses and turbulence production are also presented.

The unsteady vorticity field generates acoustic waves with higher azimuthal modes, each mode with a distinctive spectrum and directivity. The ensemble averaged peak frequency, bandwidth, and the sound pressure level agrees qualitatively with reported experimental results. The directivity of each azimuthal mode is compared with predictions of vortex sound theory. The sound generation consists of three stages. The first is a deterministic stage when linear instability waves emerge and grow and generate relatively weak sound. The second stage is nonlinear interaction and vortex breakdown; at this stage the sound pressure level reaches a peak value. The third stage is the turbulent asymptotic decay of the acoustic field. Based on the self-similar decay of the turbulent near field, the self-similar

decay of the sound field is investigated. Connection between the acoustic field and the vortex ring oscillations is also studied with vortex sound theory. Finally, we note some similarities between the sound radiated by a train of de-correlated vortex rings and turbulent jet noise. The sound pressure level, spectrum, and directivity of the train of vortex rings is similar to the sound field from a jet with similar Reynolds number and Mach number.

Contents

Acknowledgements iii

Abstract iv

1 Introduction 1

1.1 Motivation 1

1.2 Dynamics of a turbulent vortex ring 2

1.3 Aeroacoustic theory and jet noise 4

1.4 Vortex sound 7

1.5 The sound field of a turbulent vortex ring 9

1.6 Accomplishments 11

1.7 Organization of this thesis 12

2 Numerical Techniques 13

2.1 Compressible Navier-Stokes equations 13

2.2 Numerical method 15

2.3 The far field solution 23

2.4 Generation of a vortex ring 24

2.4.1 Generation of vortex rings with non-conservative body force 25

2.4.2 Introduction of azimuthal disturbances 27

2.5 Parallel implementation 28

2.6 Grid convergence 29

3 Instability, Transition and Turbulent Decay 31

3.1 Choice of Reynolds number 31

3.2 Three-dimensional vortex ring instabilities 34

3.3 Turbulent transition 39
3.4 Azimuthal flow and streamwise vorticity 45
3.5 Mean flow and turbulence statistics 47
3.6 Self-similar decay of vortex ring 59

4 Sound Field of a Turbulent Vortex Ring 63
4.1 The acoustic field 63
4.2 Sound pressure level and spectrum 65
4.3 Comparison with vortex sound theory 68
4.4 Vortex core oscillation 71
4.5 Asymptotic decay of the sound field 75
4.6 Comparison with jet noise 79

5 Conclusions and Future Work 85

A Comparison of nonimpulsive forcing with the cylinder/piston mechanism 89

Bibliography 91

List of Figures

2.1 Schematic diagram of computational domain 20
2.2 Grid stretching in axial and radial direction 20
2.3 Forcing function profile 27
2.4 Temporal evolution of turbulent energy 28
2.5 Convergence study 30

3.1 Temporal evolution of kinetic energy with different Reynolds numbers. 33
3.2 Decaying of total circulation and Reynolds number 34
3.3 Side view of azimuthal vorticity at $\theta = 0$ and $\theta = \pi$ 35
3.4 Contours of azimuthal vorticity on a plane across the ring axis 36
3.5 Mode shape plots for $n = 4$, 5, 6, 7 at $\tilde{t} = 9.18$ 37
3.6 Mode shape plots of ω_θ at $\tilde{t} = 71.2$ 38
3.7 Radial mode of vorticity 39
3.8 Azimuthal wave numbers at three axial locations 40
3.9 Evolution of kinetic energy during linear stage 41
3.10 Isosurface and contour of vorticity during transition 42
3.11 Side view of the temporal evolution of azimuthal vorticity at $\theta = 0$ and π . . 43
3.12 Temporal evolution of the kinetic energy of mode $n = 8$ and harmonics. . . . 44
3.13 Evolution of azimuthal component of kinetic energy 45
3.14 Contour plot of azimuthal velocity at $\tilde{t}$ =173 46
3.15 Temporal evolution of the streamwise vorticity ω_z 48
3.16 Iso-surface of streamwise vorticity ω_z 49
3.17 Ensemble average of total circulation 50
3.18 One-dimensional energy spectra in θ direction 50
3.19 Decay of vortex ring circulation 51

3.20 Vortex ring trajectory and translational velocity. 52

3.21 Radial profile of mean velocity and Reynolds stresses 54

3.22 ensemble-averaged axial and radial velocity 55

3.23 ensemble-averaged Reynolds stress $< \overline{u'_x u'_x}/U^{*2} >$ 56

3.24 ensemble-averaged Reynolds stress $< \overline{u'_r u'_r}/U^{*2} >$ 56

3.25 ensemble-averaged Reynolds stress $< \overline{u'_\theta u'_\theta}/U^{*2} >$ 57

3.26 ensemble-averaged Reynolds stress $< \overline{u'_x u'_r}/U^{*2} >$ 57

3.27 Turbulence production terms 58

3.28 Total turbulence production 59

3.29 Peak axial velocity along the centerline vs. axial location and time 60

3.30 Axial velocity in similarity variables 62

4.1 Contour plot of pressure at the far field 64

4.2 Azimuthal components of acoustic field 65

4.3 Acoustic signal of mode $n = 1$ 66

4.4 Sound pressure level measured at point $\chi = 52°$, $16.1R_0$ 66

4.5 Spectrum of different azimuthal modes at different polar angles 69

4.6 Polar distribution of sound pressure level 72

4.7 Pressure perturbation predicted with Möhring's formula 73

4.8 Radial velocity across the core 75

4.9 Azimuthal averaged vorticity contour during laminar stage 76

4.10 Azimuthal averaged vorticity contour during transition stage 77

4.11 Decay of acoustic field at ($|x| = 15R_0$, $\chi = 37.2°$) 78

4.12 Transform between moving frame and stationary frame 80

4.13 Acoustic field of a train of vortex rings 83

4.14 Spectrum of replicated vortex rings at $|x| = 60R$ 84

4.15 Polar distribution of total sound pressure level 84

A.1 Distance of the vortex center from the forcing location 90

A.2 Axial velocity at the center of the forcing region 90

List of Tables

2.1 Parameters for absorbing layer 23

3.1 Parameters for computations 32

Nomenclature

Latin characters

c	Sound speed
D	Cylinder diameter
e	Sum of kinetic and internal energy
f	Frequency
I	Total impulse
j	Radial number
L	Piston stroke length
L_x,L_r	Length of computational domain
n	Azimuthal number
N_{ens}	Number of realizations in an ensemble
N_x, N_r, N_θ	Grid size in axial, radial and azimuthal directions
p	Pressure
Q	Moments of vorticity in Möhring's equation
q	Heat flux
R	Ring radius
T	Temperature, duration of forcing
t	Time

T_{ij} Lighthill stress tensor

$\tilde{t}$ Nondimensional time $t\Gamma/R^2$

U_l, U_r,U_t Maximum artificial convection velocities in the sponge

U_p Piston velocity

v Velocity

Greek characters

χ Polar angle

γ Ratio of specific heats

Γ Circulation

μ Core-ring radius ratio

ν Kinematic viscosity

Ω Equivalent uniform vorticity

ω Vorticity, rotation rate

Φ Irreversible viscous dissipation

ρ Density

σ Core radius

σ_l, σ_r, σ_t Damping coefficients in the sponge

τ Viscous stresses

θ Azimuthal angle

ε Amplitude of initial disturbance, strain rate

ξ, η Self-similar coordinates

Acronyms and abbreviations

CFL Courant-Friedrichs-Lewy number

DNS Direct Numerical Simulations

M Mach number

Pr Prandtl number

Re Reynolds number

rms Root-mean-square

SPL Sound pressure level

St Strouhal number

Subscripts

$()_\infty$ Value of quantity at infinity

Superscripts

$()^*$ Dimensional quantities

$\bar{()}$ Reynolds average over azimuthal direction

$<>$ Ensemble average

Chapter 1

Introduction

1.1 Motivation

The vortex ring is the among the simplest three-dimensional vortical structures, and is a well know and popular object of theoretical and experimental investigations. Vortex rings are common in nature (e.g. Rogers 1958, Rayfield & Reif 1963, Lugt 1983, Lundgren & Mansour 1991) and in engineering applications (e.g. Chahine & Genoux 1983, Akhmetov 1980, Lundgren, Yao & Mansour 1992, Krueger & Gharib 2003). Investigations of vortex rings began in the 19th century when Lord Kelvin considered them as a model of the vortex theory of atoms (Kelvin 1867*a*), and later extended to many areas of fluid dynamics. Saffman (1981) said "Their formation is a problem of vortex sheet dynamics, the steady state is a problem of existence, their duration is a problem of stability, and if there are several we have a problem of vortex interactions." Shariff & Leonard (1992) gave an extensive review of major features of vortex ring dynamics, including the formation, steady state and azimuthal instability of vortex rings. However, some important issues related to the later stage of turbulent transition and the turbulent stage remain unresolved, which is a motivation of this study.

In addition, vortex rings have been studied for the generation of sound. In low Mach number flows, the sound field can be expressed directly in terms of vorticity unsteadiness (Möhring 1978), which led Müller & Obermeier (1988) to make the statement that vortices should also be called the "voice of the flow", adding to the statement that vortices are the "muscles and sinews" of fluid motion from Küchemann (1965). Kambe and coworkers used vortex ring as a subject for aeroacoustics experiments. They were able to successfully identify sound sources associated with collisions of rings, and the measured sound field

agreed well with theoretical modeling. (e.g. Kambe & Minota 1981, Kambe & Minota 1983). In these investigations, the vorticity unsteadiness arises from interactions between vortex rings or interaction between a vortex ring and a solid boundary. However, when a single vortex ring becomes unstable and transitions to turbulence, it also generates sound as has been investigated by Zaitsev, Kopiev, Munin & Potokin (1990). Compared with more complicated flow such as jet flow, the vorticity field of a vortex ring is relatively compact, which make it amenable to treatment with vortex sound theory. Thus another motivation of this study is to investigate the acoustic field associated with the vortex ring, and to explore the connections between vortex ring instabilities and its sound generation.

1.2 Dynamics of a turbulent vortex ring

A vortex ring can be generated in the laboratory by the motion of a piston pushing a column of fluid through an orifice or nozzle. Glezer (1988) categorized the generating conditions for vortex rings and classifies the conditions under which a given vortex generator produces either an initially laminar or turbulent ring. A transition map is constructed, which is based on two parameters: $Re = \Gamma/\nu$, where Re is the Reynolds number, Γ is total circulation of the flow and ν is the kinetic viscosity; and stroke ratio L/D, where L is the stroke length of the piston and D is the diameter of the cylinder. For a moderate stroke number $L/D = 1$, the critical Reynolds number is about 10^4. With moderate Reynolds number, a laminar vortex ring can be generated initially, but the vortex ring is unstable to azimuthal disturbance, and will break down into a turbulent vortex ring.

The transition from laminar to turbulent flow in a vortex ring begins with azimuthal instabilities in the form of bending mode. Experiments discovered that well-formed vortex ring could undergo an instability to azimuthal waves (Maxworthy 1972, Widnall & Sullivan 1973, Maxworthy 1974, Maxworthy 1977). The growth and breakdown of the waves proceeds the transition of the vortex ring. Widnall *et al.* (Widnall & Sullivan 1973, Widnall, Bliss & Tsai 1974, Widnall & Tsai 1977) proposed an inviscid model for a thin ring with a core of constant vorticity. When oscillations are imposed with a strain field due to the curvature of the ring, certain azimuthal modes with a specific radial structure become unstable. The most linearly amplified mode, the growth rate, and the radial structure can be obtained from the model. Saffman (1978) used a vortex sheet roll-up model for ring formation and

also considered viscous diffusion of the core, which gave more realistic vorticity profiles in the stability calculation. The number of waves is found to be dependent on Reynolds number, and the prediction agreed well with the experiments.

In addition to theoretical and experimental studies of the azimuthal instability, there are several numerical studies. Knio & Ghoniem (1990) constructed a 3-D vortex method for simulation of inviscid incompressible flow, and calculated linear growth of azimuthal instability waves. The mode frequency and growth rate are in agreement with theory of Widnall *et al.* They observed generation of small scales in the form of hair-pin vortex structures at the edge of the core, and the shape of the turbulent vortex ring is in qualitative agreement with experimental observations (Lugt 1983, Dyke 1982). Shariff, Verzicco & Orlandi (1994) used finite-difference calculations to study the instability of viscous vortex ring with a thicker core, with Reynolds number as high as 5500. Random and single-mode perturbations were added to the vortex ring, and multiple bands of wave numbers are amplified, each band having a distinct radial structure. Temporal evolution of kinetic energy associated with each azimuthal mode was calculated. They also found a viscous correction factor to the peak inviscid growth rate. The computation was carried on to the nonlinear growth stage before it run out of resolution. A wake structure with many layers of the hairpin vortices was formed, which showed some characters of turbulent vortex ring. However, due to the complexity of the problem, detailed study of the vorticity dynamics during the transition process was not attempted, and quantitative study of the turbulent stage was not available.

At the late nonlinear stage, Maxworthy (1977) observed a single wave propagating along the vortex ring, which induces a flow in the azimuthal direction. It is conjectured that this is a result of the nonuniform breaking of instability waves. He also discovered that for low Reynolds number flow, the azimuthal flow is very weak, the core structure breaks down much more rapidly and the ring grows much faster than vortex ring with high Reynolds number. Many researchers suggest that this azimuthal flow has the effect of stabilizing the turbulent vortex ring. For example, Yuan (1973) has shown that for long waves, axial flow reduce growth rate of unstable disturbances on a two dimensional vortex column. Moore & Saffman (1975) suggested the same effect for short waves which are observed on a vortex ring. The theory shows that the necessary condition for instability is that the dispersion equation for infinitesimal waves on an isolated vortex is degenerate, i.e. two waves, with

different angular dependence around the core but the same axial wave length, have the same speed. If there is no axial velocity along the core, the waves will degenerate due to symmetry, therefore become unstable. However, with axial flow, the steady disturbance is not necessarily degenerate and may not give rise to instability.

Among experimental studies of the turbulent vortex ring, Glezer & Coles (1990) investigated the self similar properties of the ensemble averaged flow. When the flow is turbulent, there will be dispersion in the trajectories of individual rings, and ensemble averages must be carefully implemented. Profiles of axial mean velocity, radial mean velocity, and Reynolds stress were measured. Weigand & Gharib (1994) and Auerbach (1990) observed periodic shedding of vorticity from the vortex ring to the wake, which resulted in the reduction of circulation and Reynolds number.

1.3 Aeroacoustic theory and jet noise

Acoustic waves can be associated with the pressure fluctuations in unsteady flow, particularly turbulent flow. Lighthill (1952) rearranged the equations of fluid motions into a quadrupole-driven wave equation,

$$\frac{\partial^2 \rho}{\partial t^2} - c^2 \nabla^2 \rho = \frac{\partial^2 T_{ij}}{\partial x_i \partial x_j}, \tag{1.1}$$

where ρ is the density, c is the ambient sound speed, and $T_{ij} = \rho v_i v_j + (p - \rho a_\infty^2)\delta_{ij} - \tau_{ij}$ is the Lighthill tensor, v_j, p, and τ_{ij} are the velocity, pressure, and viscous stresses. δ_{ij} is the Kronecker delta. The right-hand side of the equation are regarded as equivalent sound sources that would act in an otherwise quiescent medium. If we assume that the small eddies in turbulent flow are the quadrupole sources, a noise scaling law can be derived with dimensional analysis. Lighthill demonstrated that the acoustic power radiated by a jet should vary as the eighth power of the jet velocity. In addition, the eddies are convected downstream by the mean flow, and tend to radiate more noise in the direction of motion. The convection of acoustic source has significant effect on the directivity of jet noise (Lighthill 1954, FfowcsWilliams 1963).

In the seventies, it was discovered that turbulence in jets and free shear layers consist of large-scale turbulent structures as well as fine-scale turbulence (Crow & Champagne 1971, Brown & Roshko 1974, Winant & Broward 1974). The large scale structures are more

deterministic than the fine-scale motion. It has been suggested that turbulent mixing noise from high-speed jets consists of two essentially independent components - the noise from large turbulent structures in the form of Mach wave radiation and fine-scale turbulent noise (Tam & Chen 1994, Seiner & Krejsa 1989, Tam 1995, Tam, Golebiowski & Seiner 1996). The first part of the noise is highly directional and dominant in downstream direction, the second part is nearly uniform and dominant in the sideline and upstream directions. For the first part, linear stability theories have been used to calculate the Mach wave radiation from high Mach number jet, whereas for the second part, there is no satisfactory theory or computational result available to describe the sound field. Tam & Auriault (1999) developed a semi-empirical theory for the prediction of the fine-scale turbulence noise from high-speed jet, where the turbulence information is supplied by the $k-\epsilon$ model.

For cold subsonic jets, many researchers attempted to relate jet noise to large scale vortex structure interactions (Moore 1977, Kibens 1979, Laufer & Yen 1983, Bridges & Hussain 1992). Mankdabi & Liu (1984) attempted to incorporate the dynamics of large scale structures in the form of linear instability waves into sound source models and produced results that agrees qualitatively with experiments. Laufer & Yen (1983) observed that the far-field sound of a forced subsonic round jet was highly directive with a strong dependence on the angle from jets axis. The sound wave propagating near the axis is refracted to larger polar angles by the mean flow velocity, therefore the sound pressure level dropped near the jet axis. Bridges & Hussain (1992) used a M=0.08 cold jet and obtained relatively complete knowledge of the flow field. They employed vortex sound theory to predict the sound field. The measured sound field directivity of vortex ring pairing in circular jets was very similar to that predicted with theory: a stationary, axisymmetric, lateral quadrupole. The difference of directivity with unforced jets suggested that pairing of purely axisymmetric coherent structure was not the dominant sound source in low-Mach-number jets and that vortex asymmetry must be an essential aspect of vortex motions which produces noise in such jets. They suggested that the breakdown of large-scale vortical structures and turbulent transition towards the close of potential core can be important source of sound generation.

In numerical simulations, Colonius, Lele & Moin (1997) used direct numerical simulation (DNS) to study the sound generated by vortex pairing in a mixing layers. The acoustic field was found to be highly directive, the amplitude of the waves being greatest at shallow angles to the downstream axis of the layer, similar to jet noise experiments of Laufer & Yen

(1983). The directivity at the pairing frequencies also agreed well with a heuristic model for superdirective acoustic sources (Crighton & Huerre 1990). Mitchell, Lele & Moin (1999) computed the sound generated by vortex pairing in an axisymmetric jet. In order to induce the roll-up and pairing of vortex rings, the flow was perturbed with the jet fundamental frequency (the frequency at which disturbances acquire the largest spatial amplification rate) and its first few subharmonics. At low Mach numbers, the far-field sound had angle of extinction in the range of 60° to 70° from the jet's downstream axis, as observed in Bridges & Hussain (1992). The first DNS study of turbulent jet noise was conducted by Freund (2001) on a jet with Mach number 0.9 and Reynolds number 3600. The results showed agreement with experimental data for both mean flow development and the radiated sound. The Lighthill source was computed and analyzed.

As a summary of these previous studies, the sound field of a turbulent jet results from many components and their interactions, therefore very complicated. The jet forms an annular mixing layer at the exit of the nozzle, whereas near the centerline, the flow remain laminar and is usually referred as the *potential core*. The jet velocity profile leads to instability and roll-up of vortices in the mixing layer. The roll-up and interactions of these vortices radiate sound with a peak frequency which is related to the most unstable mode of the jet, and the sound radiation dominates at lower angles. Further downstream, these vortical structures break down and transition to turbulence towards the close of potential core, which is another mechanism that radiates sound. After turbulent transition, the fine scale turbulence radiates sound with relatively higher frequency, and dominates at higher polar angles. In addition, the sound waves propogating near the axis is bent away from the downstream flow direction by the mean jet velocity. On the other hand, a vortex ring is the simplest model of large coherent structure with relative compact vorticity field. It enables us to separate the sound generation by large-scale structures from effects of vortex interactions and mean flow refraction, and use vortex sound theory to model the sound generation. A turbulent vortex ring is also comprised of two components, i.e. large-scale vorticity structure and finer-scale turbulence. In the core region, many families of unstable modes can be excited. The lower order modes are found to be more efficient in radiating sound. In outer region and wake, fine turbulence exists and radiates sound with different frequency and directivity.

1.4 Vortex sound

In some cases, it is advantageous to rewrite Lighthill's quadrupole source T_{ij} in a form which emphasizes the contribution of local vorticity. One reason is that vortical regions of the flow are often more compact than the region over which T_{ij} is nonzero. In addition, the dynamics of the vorticity field is easier to be described than the turbulent velocity field.

Crow (1970) used the method of matched asymptotic expansions to investigate the sound generated by a turbulent eddy. To lowest order in the Mach number, he wrote the acoustic source in the form of $\rho_0 \partial^2 v_i v_j / \partial x_i \partial x_j$, where $\boldsymbol{v}$, the velocity field in a hypothetical incompressible flow, can be described by

$$\boldsymbol{v} = \mathrm{curl} \int \frac{\boldsymbol{\omega}(\boldsymbol{y}) \mathrm{d}^3 \boldsymbol{y}}{4\pi |\boldsymbol{x} - \boldsymbol{y}|}, \tag{1.2}$$

with $\boldsymbol{\omega}$ being the vorticity vector.

The Green function of the wave equation is then used to calculate the density perturbation generated by the source,

$$\rho'(\boldsymbol{x}, t) = \int \rho_0 \frac{\partial^2 v_i v_j}{\partial y_i \partial y_j} \frac{\delta(t - \tau - |\boldsymbol{x} - \boldsymbol{y}|/c)}{4\pi c^2 |\boldsymbol{x} - \boldsymbol{y}|} d^3 \boldsymbol{y} d\tau. \tag{1.3}$$

Howe (1975) rearranged the equation to demonstrate the dependence of the acoustic field on the vorticity. In the far field, the leading term in the density perturbation has the form

$$\rho'(\boldsymbol{x}, t) = -\frac{\rho_0}{4\pi c^4 |\boldsymbol{x}|^3} \frac{\partial^2}{\partial t^2} \int (\boldsymbol{x} \cdot \boldsymbol{y})(\boldsymbol{x} \cdot \boldsymbol{\omega} \times \boldsymbol{v})(\boldsymbol{y}, t - \frac{|\boldsymbol{x}|}{c}) d^3 \boldsymbol{y}. \tag{1.4}$$

Thus $\boldsymbol{\omega} \times \boldsymbol{v}$ is the source term, which enables the acoustic field to be found by integration only over regions where vorticity is nonzero.

Möhring (1978) presented the acoustic density perturbation in a form that does not contain the flow velocity, and depends linearly on the vorticity field. This enables the contribution from several vortices to add up linearly. However, it relies on the existence of a vector Green function, which is only possible with low Mach number. Möhring's equation has the form

$$\rho'(\boldsymbol{x},t) = \frac{\rho_0}{12\pi c^4|\boldsymbol{x}|^3}\frac{\partial^3}{\partial t^3}\int(\boldsymbol{x}\cdot\boldsymbol{y})\boldsymbol{y}\cdot(\boldsymbol{\omega}\times\boldsymbol{x})d^3\boldsymbol{y}. \tag{1.5}$$

This formula was used to calculate the sound pressure generated by a circular vortex ring of radius R centered at a position $\boldsymbol{a}$, with circulation Γ. The far field pressure perturbation is:

$$p'(\boldsymbol{x},t) = \frac{\rho_0}{4c^2|\boldsymbol{x}|^3}\frac{\partial^3}{\partial t^3}\left[\Gamma R^2\left\{(\boldsymbol{x}\cdot\boldsymbol{a})(\boldsymbol{x}\cdot\boldsymbol{n}) - \frac{1}{3}|\boldsymbol{x}|^2\boldsymbol{a}\cdot\boldsymbol{n}\right\}\right], \tag{1.6}$$

where $\boldsymbol{n}$ is a unit vector normal to the ring. If the ring moves in the direction of $\boldsymbol{n}$, $\boldsymbol{a} = z\boldsymbol{n}$, the formula simplifies,

$$p'(\boldsymbol{x},t) = \frac{\rho_0}{4c^2|\boldsymbol{x}|^3}\frac{\partial^3}{\partial t^3}\left[\Gamma R^2 z\left\{(\boldsymbol{x}\cdot\boldsymbol{n})^2 - \frac{1}{3}|\boldsymbol{x}|^2\right\}\right]. \tag{1.7}$$

thus the sound field of axisymmetric vortex rings has the directivity of that produced by a lateral quadrupole and an isotropic quadrupole.

Obermeier (1985) and Kambe (1986) gave vortex sound theory rigorous treatment by using matched asymptotic expansions and singular perturbation methods. Kambe presented a general solution for vortex-induced sound in the presence of a solid surface by matching a multipole expansion of the far-field pressure P_F from wave equation with a near field P_l of the vortex field. Möhring's formula was recovered for vortex flow without solid boundary interaction. For a series of co-axial axisymmetric vortex rings, the far-field pressure perturbation is given by

$$p'(\boldsymbol{x},t) = \frac{\rho_0}{4c^2|\boldsymbol{x}|}\left(\cos^2\chi - \frac{1}{3}\right)\dddot{Q}(t-|\boldsymbol{x}|/c), \tag{1.8}$$

where $Q(t) = -2\Gamma R^2 z(t)$ and χ is the polar angle of the observer. Eq. (1.8) reveals two important facts about sound generation of axisymmetric vortex systems: the magnitude of p' scales on $\rho_0 U_0^4 R_0/c^2|\boldsymbol{x}|$, where U_0 is the initial speed of the ring. The directivity of a series of axisymmetric vortex rings is $(\cos^2\chi - \frac{1}{3})$, and there is an angle of distinction at $\chi = \cos^{-1}(3^{-\frac{1}{2}}) = 54.7°$. Both amplitude and directivity were confirmed in the experiments of Kambe *et al.*

1.5 The sound field of a turbulent vortex ring

The first experimental investigation of sound generated by a turbulent vortex ring in an anechoic chamber was reported by Zaitsev et al. (1990). The vortex ring has initial Reynolds number $Re = V_0 D/\nu = 6.8 \times 10^4$. Over the period of acoustic sampling, the vortex ring has a core-to-ring radius ratio of about $\mu = 0.12$. Acoustic signal shows a peak of the spectrum in a narrow frequency band of $\Delta f \approx 300Hz$, with the maximum frequency $f_0 \approx 1200Hz$. When the peak frequency is scaled with the initial vortex ring velocity and diameter of the orifice, it has a Strouhal number of $St = fD/U = 2.0$. On the other hand, when the peak frequency is scaled with vortex ring parameters over the period of acoustic sampling, the Strouhal number is around 8.4. As the vortex ring moved downstream, the peak frequency drifted to lower frequency. In a more recent experiment, Zaitsev, Kopiev & Kotova (2001) used a circular array of microphones in order to extract quadrupole components from the total noise. Average contributions of different azimuthal components were studied, and their directivity was compared with prediction from vortex sound theory (Möhring 1978). However, since the microphone array was placed in one circular plane, instantaneous polar distribution of acoustic signal could not be measured, and had to be obtained from the analysis of the time evolution of different harmonics. The non-stationary character of the mean flow complicated the analysis.

To study the sound generation mechanism, Kopiev & Chernyshev (1997) modeled the vortex ring as an oscillating system with an infinite number of degrees of freedom. There are two family of vortex ring oscillations, one is short-wave oscillations in azimuthal direction, which are the bending mode discussed in Section 1.2. Another family is long-wave oscillations, which are related to core oscillations. The oscillations are characterized by 3 numbers: a discrete frequency ω_m, which is scaled with $\Omega/2$ and Ω is the uniform vorticity in the core; n , azimuthal number, which is the number of waves along the ring; and j, a radial number that represents the radial structure of the mode in the core section.

Eigen-oscillations are defined by a displacement field $\epsilon(\mathbf{r}, t)$ to the boundary, which is in the form

$$\epsilon(\mathbf{r}, t) = \epsilon^i(\sigma, \psi)\exp(in\theta - i\omega t). \tag{1.9}$$

σ, ψ are coordinates fixed on the core. A system of equations with boundary conditions can

be derived for $\epsilon(\mathbf{r}, t)$. Solving the system can give eigen-frequency ω_m and the forms of eigen-oscillation. After all the modes are obtained, the acoustic field is calculated with formula of Möhring. It is found that the most efficient sound radiating modes have azimuthal number $n = 0,1,2$, and frequency $\omega_m = 1$. They include one axisymmetric mode (1,0,0), 2 isolated modes of (1,1,0) and (1,2,0), and infinite number of Bessel modes $(1,1,j)$,$(1,2,j)$. The sound pressure level and directivity associated with each mode can be obtained.

The theory was derived for vortex ring with uniform vorticity distribution and thin core, but it is valid for any vortex ring with steady vorticity distribution differing from uniform by $O(\mu^2)$. The theory reproduced some of the experimental observations: the peak frequency corresponds to modes with $\omega_m = 1$, which includes several families of oscillations and expand in the interval $\Delta\omega/\omega = (-4\mu, 4\mu)$, where $\mu = \sigma/R$ is the core-ring ratio. With the experimental parameters of the vortex ring, the predicted peak frequency and bandwidth agreed well with experiments.

Other researchers have tried to explain the measured acoustic signal to aspects of vortex ring dynamics. Shariff, Leonard & Ferziger (1989) tried to fit the frequency to lower azimuthal mode ($n = 2$ mode) and Moore's axisymmetric elliptic core ring (Moore 1980). They found that the second mechanism agrees better with the experiment. The non-circular core structure caused oscillation in both aspect ratio and orientation angle. Using vortex sound theory, the acoustic signal was found to be sinusoidal at twice the frequency of the core rotation. However, the elliptic core ring is an ideal case. When a vortex ring is generated in laboratory, it goes through a relaxation process to the steadily translational stage close to the Norbury family of vortex rings (Norbury 1973), and the axisymmetric oscillation can only be sustained for several eddy turnover times, therefore the elliptic mode alone can not be the sound generation mechanism after the vortex ring formation. The problem was also studied using contour dynamics (Tang & Ko 2000, Tang & Ko 2003), and it is found that the two basic vortex sound generation mechanisms are vortex core deformation and the vorticity centroid dynamics, and are independent of the specific vortex system. Rivoalen, Huberson & Knio (2003) used an axisymmetric vortex particle method to study the sound production by isolated vortex rings for both nominally steady and unsteady cores. The acoustic signals reveal a dominant period that is approximately half the eddy turnover time. In addition, the amplitude of the radiated sound from unsteady cores is substantially higher than that of similar steady rings. In addition to core oscillations, Weigand & Gharib

(1994) and Auerbach (1990) found that a turbulent vortex ring will periodically eject hair-pin vortices into the wake, and speculated that the vortex shedding was the source of the sound generation.

In the present study, the acoustic field of the vortex ring is calculated directly. The spectrum and sound pressure level is compared with experimental data and the theoretical models. Possible sound generation mechanism by the vortex ring is discussed.

1.6 Accomplishments

In this section we review the progress we have made in meeting the objectives set out in Section 1.1.

- It is the first DNS study of a turbulent vortex ring with its sound field. Detailed information on instability, turbulent transition and decay is obtained. The simulated flow field shows good agreement with theories and experimental data on linear instability and turbulent self-similar decay.

- DNS provides detailed information on acoustic sources not available in experiments. Because the flow field is non-stationary, large number of realizations are computed to get accurate ensemble average. It increases the amount of computation by an order of amplitude than previous numerical simulations, and also increases the complexity in data process.

- The spectrum and sound pressure level agree well with experiments, and the simulation results confirms the scaling of peak frequency and bandwidth proposed by the model of Kopiev & Chernyshev (1997).

- We analyzed the temporal evolution of sound pressure level and directivity associated with each azimuthal modes, which are not available from previous experiments. The peak sound radiation occurs during late transition stage and turbulent breakdown. The acoustic field then decays with self-similarity. The directivity of each azimuthal mode, after corrected with Doppler factor, agrees well with vortex sound theory.

- The sound radiation by a train of de-correlated vortex rings is compared with turbulent jet noise. The sound pressure level, spectrum, and directivity of the train of vortex

rings is similar to the sound field from a jet with similar Reynolds number and Mach number. It confirms that the vortex ring is a good model for sound generated by large-scale coherent structures in turbulent jet.

1.7 Organization of this thesis

In Chapter 2, the numerical schemes to solve three-dimensional compressible Navier-Stokes equations are presented, and spatial and time discretization, boundary condition and centerline treatment are discussed. The solution is extended to the far field by solving a wave equation utilizing spherical harmonics. The method of generating a vortex ring and adding three dimensional stochastic perturbation to the ring is introduced. A further comparison between this method and the piston/cylinder mechanism in laboratory can be found in Appendix A.

In Chapter 3, we study the turbulent transition process, including the early linear azimuthal instability, nonlinear amplification of the higher azimuthal modes, breaking of the azimuthal waves, and the instantaneous vortical structure of the turbulent vortex ring. The numerical results are compared with linear instability theories, experiments, and previous numerical simulations. Self-similarity of the turbulent flow is evaluated by averaging an ensemble of simulations.

In Chapter 4, we investigate the acoustic field generated by the vortex motion, with focus on frequency spectrum, sound pressure level, and directivity of the acoustic signal with different azimuthal numbers. The result is compared with experimental data of Zaitsev et al. (1990) and theoretical model of Kopiev & Chernyshev (1997). Comparison with vortex sound theory is also discussed. In addition, the sound field of a train of de-correlated vortex rings is studied and compared with the sound field of turbulent jets with similar Mach number and Reynolds number.

Conclusions and future extension of the study are discussed in Chapter 5.

Chapter 2

Numerical Techniques

2.1 Compressible Navier-Stokes equations

The flow field of a turbulent vortex ring and its acoustic field are both governed by the compressible Navier-Stokes equations. In the numerical simulations, the physical quantities are nondimensionalized based on the initial vortex ring radius, R_0, ambient density, ρ_∞, and ambient sound speed, a_∞. Therefore,

$$x = \frac{x^*}{R_0} \qquad r = \frac{r^*}{R_0} \qquad u_x = \frac{u_x^*}{a_\infty} \qquad v_r = \frac{v_r^*}{a_\infty} \qquad v_\theta = \frac{v_\theta^*}{a_\infty} \qquad t = \frac{t^* a_\infty}{R_0}$$
$$\rho = \frac{\rho^*}{\rho_\infty} \qquad p = \frac{p^*}{\rho_\infty a_\infty^2} \qquad T = \frac{T^* c_p}{a_\infty^2} \qquad e = \frac{e^*}{\rho_\infty a_\infty^2},$$

where the superscript $()^*$ denotes a dimensional quantity, and e is the total energy per unit volume. In the cylindrical coordinate system (x, r, θ), the mass conservation equation is

$$\frac{\partial \rho}{\partial t} + \frac{\partial}{\partial x}(\rho u_x) + \frac{1}{r}\frac{\partial}{\partial r}(r\rho v_r) + \frac{1}{r}\frac{\partial}{\partial \theta}(\rho v_\theta) = 0, \tag{2.1}$$

and the equations of momentum conservation in the axial, radial and azimuthal directions are

$$\frac{\partial}{\partial t}(\rho u_x) + \frac{\partial}{\partial x}(\rho u_x u_x) + \frac{1}{r}\frac{\partial}{\partial r}(r\rho u_x v_r) + \frac{1}{r}\frac{\partial}{\partial \theta}(\rho u_x v_\theta) = -\frac{\partial p}{\partial x} + V_x, \tag{2.2}$$

$$\frac{\partial}{\partial t}(\rho v_r) + \frac{\partial}{\partial x}(\rho v_r u_x) + \frac{1}{r}\frac{\partial}{\partial r}(r\rho v_r v_r) + \frac{1}{r}\frac{\partial}{\partial \theta}(\rho v_r v_\theta) - \frac{\rho v_\theta^2}{r} = -\frac{\partial p}{\partial r} + V_r, \tag{2.3}$$

$$\frac{\partial}{\partial t}(\rho v_\theta) + \frac{\partial}{\partial x}(\rho v_\theta u_x) + \frac{1}{r}\frac{\partial}{\partial r}(r\rho v_\theta v_r) + \frac{1}{r}\frac{\partial}{\partial \theta}(\rho v_\theta v_\theta) + \frac{\rho v_r v_\theta}{r} = -\frac{1}{r}\frac{\partial p}{\partial \theta} + V_\theta, \tag{2.4}$$

respectively, where V_x, V_r, and V_θ are the viscous terms that are defined later. The energy equation is

$$\begin{aligned}\frac{\partial e}{\partial t}+\frac{\partial}{\partial x}[u_x(e+p)]+\frac{1}{r}\frac{\partial}{\partial r}[rv_r(e+p)]+\frac{1}{r}\frac{\partial}{\partial\theta}[v_\theta(e+p)]=\\ -\frac{\partial q_x}{\partial x}-\frac{1}{r}\frac{\partial}{\partial r}(rq_r)-\frac{1}{r}\frac{\partial q_\theta}{\partial\theta}+u_xV_x+v_rV_r+v_\theta V_\theta+\Phi,\end{aligned} \tag{2.5}$$

where Φ is the irreversible viscous dissipation and q_x, q_r, and q_θ are the heat fluxes. The viscous dissipation and the heat fluxes are defined later. The sum of the internal and kinetic energy, e , is given by

$$e=\frac{p}{\gamma-1}+\frac{\rho}{2}(u_x^2+v_r^2+v_\theta^2), \tag{2.6}$$

where the ratio of specific heats, γ , is taken to be 1.4. From the ideal gas law, the nondimensional temperature is given by

$$T=\frac{\gamma}{\gamma-1}\frac{p}{\rho}. \tag{2.7}$$

The viscous terms appearing in the momentum equations are

$$V_x = \frac{\partial\tau_{xx}}{\partial x}+\frac{1}{r}\frac{\partial r\tau_{xr}}{\partial r}+\frac{1}{r}\frac{\partial\tau_{x\theta}}{\partial\theta} \tag{2.8}$$

$$V_r = \frac{\partial\tau_{xr}}{\partial x}+\frac{1}{r}\frac{\partial r\tau_{rr}}{\partial r}+\frac{1}{r}\frac{\partial\tau_{r\theta}}{\partial\theta}-\frac{1}{r}\tau_{\theta\theta} \tag{2.9}$$

$$V_\theta = \frac{\partial\tau_{x\theta}}{\partial x}+\frac{1}{r}\frac{\partial r\tau_{\theta r}}{\partial r}+\frac{1}{r}\frac{\partial\tau_{\theta\theta}}{\partial\theta}+\frac{1}{r}\tau_{r\theta}. \tag{2.10}$$

The viscous dissipation term Φ is

$$\begin{aligned}\Phi=&\tau_{xx}\frac{\partial u_x}{\partial x}+\tau_{xr}\frac{\partial v_r}{\partial x}+\tau_{x\theta}\frac{\partial v_\theta}{\partial x}\\ &+\tau_{xr}\frac{\partial u_x}{\partial r}+\tau_{rr}\frac{\partial v_r}{\partial r}+\tau_{r\theta}\frac{\partial v_\theta}{\partial r}\\ &+\frac{\tau_{x\theta}}{r}\frac{\partial u_x}{\partial\theta}+\frac{\tau_{r\theta}}{r}\frac{\partial v_r}{\partial\theta}+\frac{\tau_{\theta\theta}}{r}\frac{\partial v_\theta}{\partial\theta}+\frac{v_r\tau_{\theta\theta}}{r}-\frac{v_\theta\tau_{r\theta}}{r}.\end{aligned} \tag{2.11}$$

We assume a Newtonian fluid. Since the Mach number is less than 0.3, temperature variations are small; hence, we assume the viscosity is constant throughout the flow field.

With these assumptions, the viscous stresses in cylindrical coordinates are

$$\mathrm{Re}_a \tau_{xx} = 2\frac{\partial u_x}{\partial x} - \frac{2}{3}\Theta + \frac{\mu_B}{\mu}\Theta, \tag{2.12}$$

$$\mathrm{Re}_a \tau_{xr} = \frac{\partial v_r}{\partial x} + \frac{\partial u_x}{\partial r}, \tag{2.13}$$

$$\mathrm{Re}_a \tau_{x\theta} = \frac{\partial v_\theta}{\partial x} + \frac{1}{r}\frac{\partial u_x}{\partial \theta}, \tag{2.14}$$

$$\mathrm{Re}_a \tau_{rr} = 2\frac{\partial v_r}{\partial r} - \frac{2}{3}\Theta + \frac{\mu_B}{\mu}\Theta, \tag{2.15}$$

$$\mathrm{Re}_a \tau_{r\theta} = \frac{\partial v_\theta}{\partial r} + \frac{1}{r}\frac{\partial v_r}{\partial \theta} - \frac{v_\theta}{r}, \tag{2.16}$$

$$\mathrm{Re}_a \tau_{\theta\theta} = 2\left(\frac{1}{r}\frac{\partial v_\theta}{\partial \theta} + \frac{v_r}{r}\right) - \frac{2}{3}\Theta + \frac{\mu_B}{\mu}\Theta, \tag{2.17}$$

where Θ is dilatation of the velocity field, given by

$$\Theta = \frac{\partial u_x}{\partial x} + \frac{1}{r}\frac{\partial r v_r}{\partial r} + \frac{1}{r}\frac{\partial v_\theta}{\partial \theta}, \tag{2.18}$$

and Re_a is the Reynolds number based on the speed of sound:

$$\mathrm{Re}_a = \frac{\rho_\infty a_\infty R_0}{\mu_\infty}. \tag{2.19}$$

In the simulations, it is assumed that the bulk viscosity is related to the shear viscosity by a constant ratio of $\mu_B/\mu = 0.6$, which is the value given for air by Thompson (1991).

The heat fluxes in the energy equation are given by Fourier's Law:

$$q_x = \frac{-1}{\mathrm{RePr}}\frac{\partial T}{\partial x}, \qquad q_r = \frac{-1}{\mathrm{RePr}}\frac{\partial T}{\partial r}, \qquad q_\theta = \frac{-1}{\mathrm{RePr}}\frac{1}{r}\frac{\partial T}{\partial \theta}, \tag{2.20}$$

where the Prandtl number $\mathrm{Pr} = c_p\mu/k = 0.7$.

2.2 Numerical method

Equations 2.1 to 2.20 were solved using high-order-accurate methods in order to simulate both fine-scale turbulent flow and the acoustic field.

Axial and radial discretization

In the axial and radial directions, a sixth-order Padé scheme (Lele 1992) was applied.

The first derivative of a function f at the ith grid point, f'_i, was calculated implicitly with

$$f'_{i+1} + 3f'_i + f'_{i-1} = \frac{7}{3}\frac{f_{i+1} - f_{i-1}}{\Delta s} + \frac{1}{12}\frac{f_{i+2} - f_{i-2}}{\Delta s}, \tag{2.21}$$

where Δs is the grid spacing of a uniform mesh.

At the end-points of the domain, lower-order compact schemes were used. At the 2nd point next to the boundary ($i = 2$ and $N - 1$), we used a fourth-order central-differencing scheme:

$$f'_1 + 4f'_2 + f'_3 = 3\frac{f_3 - f_1}{\Delta s} \tag{2.22}$$

$$f'_{N-2} + 4f'_{N-1} + f'_N = 3\frac{f_N - f_{N-2}}{\Delta s}. \tag{2.23}$$

At the boundary point ($i = 1$ and N), a one-sided third-order scheme was applied:

$$4f'_2 + 2f'_1 = \frac{-5f_1 + 4f_2 - f_3}{\Delta s} \tag{2.24}$$

$$4f'_{N-1} + 2f'_N = \frac{5f_N - 4f_{N-1} + f_{N-2}}{\Delta s}. \tag{2.25}$$

These differencing scheme lead to a tridiagonal system that was solved with the Thomas algorithm to get the derivatives at each point. Second derivatives were calculated with compact difference schemes of the same order as the first derivatives. Specifically, at the inner points, a sixth-order Padé scheme was applied:

$$2f''_{i-1} + 11f''_i + 2f''_{i+1} = 12\frac{f_{i+1} - 2f_i + f_{i-1}}{\Delta s^2} + \frac{3}{4}\frac{f_{i+2} - 2f_i + f_{i-2}}{\Delta s^2}. \tag{2.26}$$

The points at $i = 2$ and $N - 1$ were solved with a fourth-order compact scheme:

$$f''_3 + 10f''_2 + f''_1 = \frac{12f_3 - 24f_2 + 12f_1}{\Delta s^2}, \tag{2.27}$$

$$f''_N + 10f''_{N-1} + f''_{N-2} = \frac{12f_N - 24f_{N-1} + 12f_{N-2}}{\Delta s^2}, \tag{2.28}$$

and the second derivatives at points $i = 1$ and N were solved with a third-order one-sided

scheme:

$$f_1'' + 11 f_2'' = \frac{13 f_1 - 27 f_2 + 15 f_3 - f_4}{\Delta s^2}, \tag{2.29}$$

$$f_N'' + 11 f_{N-1}'' = \frac{13 f_N - 27 f_{N-1} + 15 f_{N-2} - f_{N-3}}{\Delta s^2}. \tag{2.30}$$

Azimuthal discretization

Since the azimuthal grid is periodic, a Fourier spectral method was used in this direction. Flow quantities were transformed into the Fourier space, and azimuthal derivatives were calculated with multiplication by ik_θ for the first derivative, and by $-k_\theta^2$ for the second derivative.

The maximum allowable time step for convective problems is usually determined by the Courant-Friedrichs-Lewy (CFL) number. When explicit time advancement is used, the time step will depend on the minimum mesh spacing in any of the three coordinate directions. In cylindrical coordinates, the very fine azimuthal mesh spacing near $r = 0$ imposes a severe time step limitation. However, the fine mesh is unnecessary because no fine scales needs to be resolved near the centerline. Therefore, we can alleviate this constraint by explicitly filtering the results in the θ direction. When taking derivatives, a sharp spectral filter was used to filter out the azimuthal modes that were higher than a cut off wave number $N_m(r_j)$ at the first several circles around $r = 0$. By choosing the appropriate cut off wave numbers, the time step can be the same order of Δr, not $\Delta r \Delta\theta$. A detailed description of the filtering was presented by Mohseni & Colonius (2000). However, energy in the discarded wave numbers can slowly grow due to nonlinear products from lower wave numbers. This energy is not dissipated nor convected, therefore needs to be removed numerically. For this purpose, the conservative variables were filtered at the end of every time step using the same cut off wave numbers.

Computational Grid

The computational domain is shown schematically in Figure 2.1. A nonuniform mesh

is used in both the axial and radial directions. In the axial direction, grid spacing is nearly uniform over the region from $-5R_0$ to $5R_0$, where high resolution is needed to resolve the turbulent structure of the vortex ring. In the far field, only the acoustic waves need to be resolved, a coarser grid can be used. In the radial direction, the fine grid extends from 0 to $3R_0$, and was most compressed around the region of $r = R_0$, where the vortex ring core was located.

To determine the optimal grid stretching scheme, we require estimates for the size of the computation domain and the grid resolution that is necessary. The computational domain needs to be large enough to include at least one wave length of the sound wave. From the experimental results of Zaitsev et al. (1990), a vortex ring will generate sound with a peak Strouhal number around $\mathrm{St} = 2fR/u = 2.0$, where u is the translational velocity. Thus, the corresponding wavelength is $\lambda/R = a/u = 1/M$, where M is the translational Mach number. The domain needs to be very large when the Mach number is small. In the present study, the vortex rings had the maximum translational Mach number between 0.14 to 0.28, therefore, the characteristic wavelength varied from $3.6R_0$ to $7.1R_0$. This gives the estimate of the domain size as well as the largest grid spacing in the far field.

On the other hand, the grid must be fine enough to resolve the smallest turbulent scale. The Kolmogorov length scale, $l = (\nu^3/\epsilon)^{1/4}$, has been used as a measure for the smallest scale, where ν is the kinematic viscosity, ϵ is the energy dissipation. l decreases with an increased Reynolds number, with the relationship $l \sim \mathrm{Re}^{-3/4}$. A initially laminar vortex will become turbulent at a Reynolds number higher than 2000, which provides a lower limit to the simulations. In practice, the fine grid width has to be determined by convergence study at different Reynolds numbers (see section 2.6).

Once the extent and grid spacing are determined, grid stretching is accomplished by mapping the axial and radial mesh onto a uniform mesh with smooth functions $x = g(s)$ and $r = h(s)$. The differentiation with respect to x and r are related to derivatives on the uniform grid with the mapping function. For example,

$$\frac{\partial f}{\partial x} = \frac{1}{g'}\frac{\partial f}{\partial s}, \qquad \frac{\partial^2 f}{\partial x^2} = \frac{1}{g'^2}\frac{\partial^2 f}{\partial s^2} + \frac{g''}{g'^3}\frac{\partial f}{\partial s}. \tag{2.31}$$

The forms of g' and h' are specified first because they are directly proportional to the grid spacing. In the axial direction, the uniform grid s extends from -1 to 1, and $g'(s)$ is

given by

$$g'(s) = \frac{\Delta x_0}{\Delta s}\left[1 + g_{\max}\left(1 + \mathrm{erf}\left(\frac{s-1}{\sigma_x}\right) + 1 - \mathrm{erf}\left(\frac{s+1}{\sigma_x}\right)\right)\right], \tag{2.32}$$

where $\Delta s = \frac{2}{N}$ is the grid width in s, Δx_0 is the mapped grid width in the middle of the domain, where the grid is nearly uniform. The maximum grid spacing near the boundary is given by $\Delta x_0(1 + g_{\max})$. σ_x controls the extent of the region with nearly uniform grid. In the present simulations, we chose $\Delta x_0 = 0.03$, $g_{\max} = 30.0$, and $\sigma_x = 0.1$.

Once equation(2.32) is given, the mapping functions $g(s)$ and its second derivative $g''(s)$ can be calculated. With 320 grid points, the computation domain extended to $-12R_0$ and $12R_0$, with a nearly uniform grid from $-4R_0$ to $4R_0$.

In the radial direction, similar mapping function was used, but the uniform grid extends from 0 to 1, and the r grid points should be most compressed near the region $r = 1.0R_0$. Therefore, h' takes the form:

$$h'(s) = \frac{\Delta r_0}{\Delta s}\left[1 + g_{\max}\left(1 + \mathrm{erf}\left(\frac{s-1}{\sigma_{r1}}\right)\right) + g_{\min}\left(1 - \mathrm{erf}\left(\frac{s-r_m}{\sigma_{r2}}\right)\right)\right], \tag{2.33}$$

where the constant r_m was determined iteratively so that the minimum grid width was achieved around $r = 1.0R_0$. The value used in the simulations was $r_m = -0.3$, and the values of the other constants were $g_{\max} = 20.0$, $g_{\min} = 3.0$, $\sigma_{r1} = \sigma_{r2} = 0.2$. With 160 grid points, the computation domain extended to about $15R_0$, and minimum grid spacing was located between $0.5R_0$ and $2.5R_0$.

Centerline treatment

In cylindrical coordinates, some terms in the Navier-Stokes equations are geometrically singular at $r = 0$. A variety of numerical methods have been proposed to deal with this problem. These include developing pole conditions (Huang & Sloan 1993), changing variables to avoid singularity(Verzicco, Orlandi, Eisenga, van Heijst & Carnevale 1996), or solving the equations in Cartesian coordinates at the singular point(Thompson 1987, Mitchell, Lele & Moin 1995, Freund, Lele & Moin 1997).

In the present study, the approach by Mohseni & Colonius (2000) was adopted. New radial coordinates are defined over both positive radius (where the azimuthal angle is between 0 and π) and negative radius (where the azimuthal angle is between π and 2π); the first

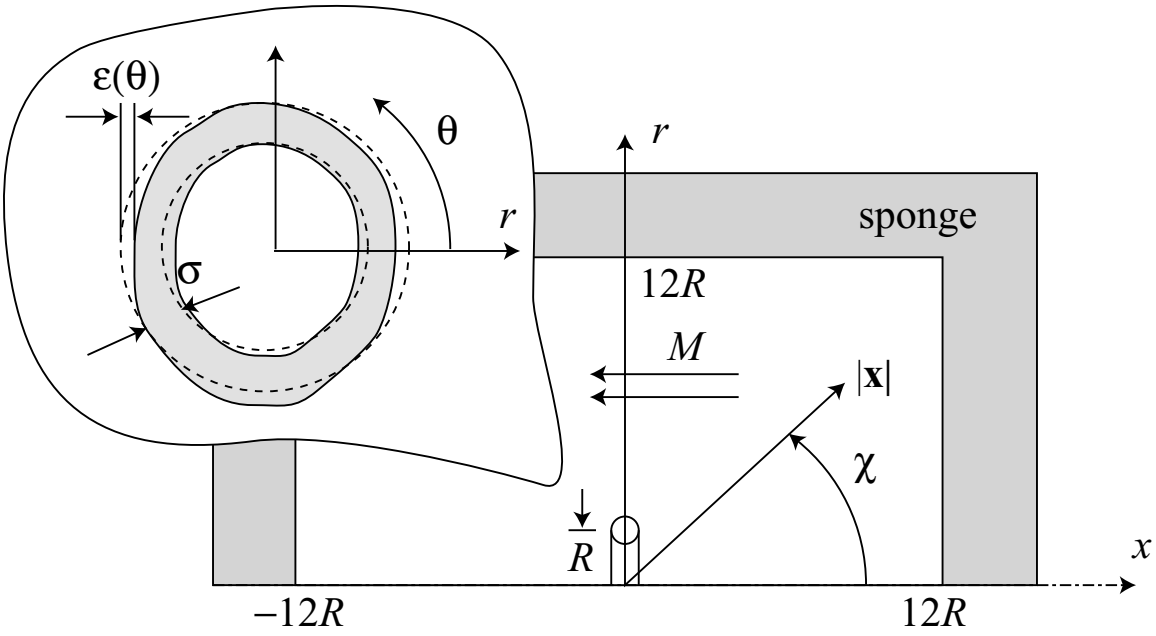

Figure 2.1: Schematic diagram of computational domain for the vortex ring.

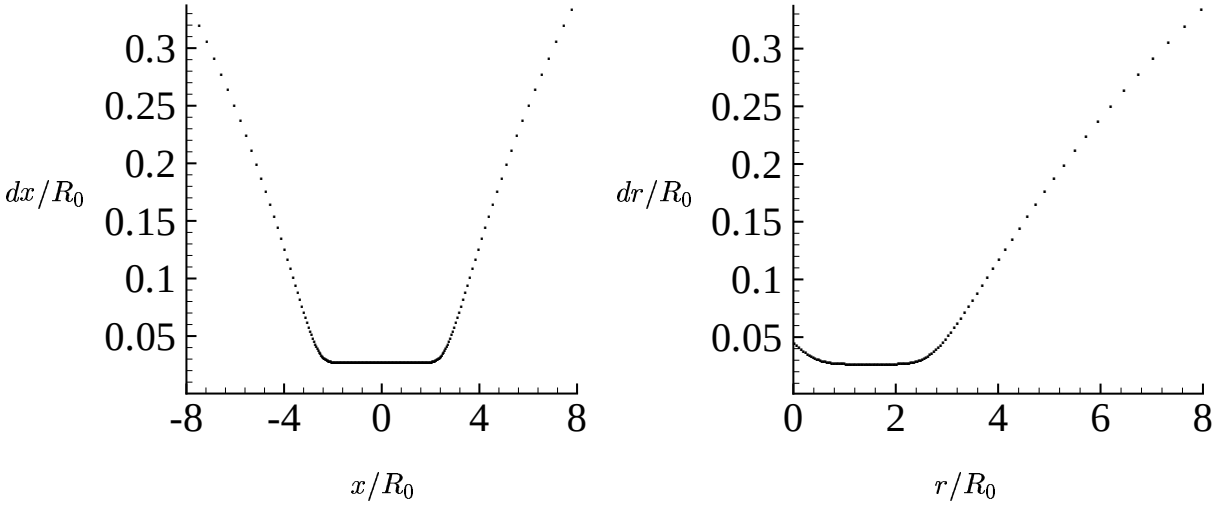

Figure 2.2: Grid stretching in axial and radial direction.

two radial points were placed in $r_1 = \Delta r/2$ and $r_{-1} = -\Delta r/2$, which avoids the singularity; in addition, scalar and vector quantities must be transformed appropriately across the centerline. This approach is easy to implement and resulted in negligible reflection from the centerline. Constantinescu & Lele (2002) proposed a numerical method with nonstaggered grids, and governing equations for the flow at the polar axis are derived using series expansions near r = 0. Flow variables and their radial derivatives are needed to calculate the coefficients in these equations, and the derivatives are calculated using a similar mapping of the flow domain from $(0, R) \times (0, 2\pi)$ to $(-R, R) \times (0, \pi)$.

Time advancement scheme

The N-S equations were explicitly advanced in time with a standard fourth-order Runge-Kutta scheme. Although it requires more CPU time per step and memory than other schemes, it significantly reduces the phase and amplitude errors related to wave propagation, and also gives a larger stable time step and good overall efficiencies. Combining the compact difference scheme and the fourth-order Runge-Kutta time advancement, the time step restriction for a model one-dimensional convection equation is

$$\mathrm{CFL} = \frac{c\Delta t}{\Delta s} \leq 1.43, \tag{2.34}$$

and for a one-dimensional diffusion equation is

$$\frac{\nu \Delta t}{(\Delta s)^2} \leq .422. \tag{2.35}$$

In the present simulations, we used a time step of $c\Delta t/R_0 = .012$, which corresponds to a maximum CFL of 0.4, in order to satisfy both stability and accuracy requirements.

Nonreflecting boundary condition

The acoustic disturbances generated by the turbulent flow will propagate to infinity; however, the computation domain must be truncated within a finite length. Numerical boundary conditions must be designed to minimize the reflection from this artificial

boundary. Various nonreflecting boundary conditions have been reviewed in Givoli (1991), Tsynkov (1998), and Colonius (2004). For linear problems or for problems that can be linearized with specified accuracy near the boundary, boundary conditions can be derived from mathematical analysis (Engquist & Majda 1979, Bayliss & Turkel 1982, Giles 1990, Tam & Webb 1993, Rowley & Colonius 2000). On the other hand, when nonlinear effects are significant near the boundary, there is no rigorous mathematical theory to guide the design of nonreflecting boundary conditions, and various absorbing layer techniques have been used with improved accuracy (Colonius, Lele & Moin 1993, Hu 1996, Freund 1997, Colonius & Ran 2002). There are a set of parameters associated with the absorbing layer that can be tuned to minimize reflection into the domain.

In the present study, the inflow/outflow boundary conditions proposed by Freund (1997) was adopted. Convection terms $U(x)$ and $U(r)$ were added to the momentum and energy equations in the absorbing layer to accelerate the flow to supersonic. Therefore, all the characteristics at a boundary are incoming or outgoing, and simple boundary condition can be used. In addition, damping terms $\sigma(x)$ and $\sigma(r)$ are added to the equations to damp the disturbances in the layer. Thus the equations in the entire domain have the form

$$\frac{\partial \boldsymbol{Q}}{\partial t} + U(x)\frac{\partial \boldsymbol{Q}}{\partial x} + \frac{\partial \boldsymbol{E}}{\partial x} + U(r)\frac{\partial \boldsymbol{Q}}{\partial r} + \frac{\partial \boldsymbol{F}}{\partial r} + \frac{1}{r}\frac{\partial \boldsymbol{G}}{\partial \theta} + \boldsymbol{H} = \boldsymbol{I} - (\sigma(x) + \sigma(r))(\boldsymbol{Q} - \boldsymbol{Q}_0), \quad (2.36)$$

where the target state $\boldsymbol{Q}_0$ is the state of zero perturbation. A form with compact support in the buffer zone is chosen for $U(x)$, $U(r)$, and σ:

$$\begin{aligned}
U(x) &= U_l\left[1 + \tanh\left(-\mathrm{w_l(x - x_{min})}\right)\right] + U_r\left[1 + \tanh\left(\mathrm{w_r(x - x_{max})}\right)\right], && (2.37)\\
U(r) &= U_t\left[1 + \tanh\left(\mathrm{w_t(r - r_{max})}\right)\right], && (2.38)\\
\sigma(x) &= \sigma_l\left[1 + \tanh\left(-\mathrm{w_l(x - x_{min})}\right)\right] + \sigma_r\left[1 + \tanh\left(\mathrm{w_r(x - x_{max})}\right)\right], && (2.39)\\
\sigma(r) &= \sigma_t\left[1 + \tanh\left(\mathrm{w_t(r - r_{max})}\right)\right], && (2.40)
\end{aligned}$$

where the subscripts l, r and t denote values at left, right, and top boundaries, respectively. U_l, U_r and U_t are the maximum artificial convection velocities in the absorbing layers, and σ_l, σ_r and σ_t are the maximum damping coefficients. w_l, w_r and w_t control the width of the layer.

The corresponding coefficients used in the present study are given in table 2.1.

U_l/a_∞	-1.5	U_r/a_∞	1.5	U_t/a_∞	1.0
σ_l	1.5	σ_r	1.5	σ_t	1.5
w_l	0.4	w_r	0.4	w_t	0.4

Table 2.1: Parameters for absorbing layer.

2.3 The far field solution

The solution is extended to far field by solving a wave equation in a spherical coordinate system ($|x|$, χ, θ), where $|x|$ is the radial distance to the vortex ring, χ is the polar angle, and θ is the azimuthal angle. The DNS solution on a sphere of radius $10R$ is decomposed into spherical harmonics, and a one-dimensional wave equation in the radial direction is solved for each spherical harmonic on a domain $10R < |x| < 90R$. The wave equation is

$$\frac{\partial^2 p}{\partial t^2} - \nabla^2 p = 0, \tag{2.41}$$

where

$$p = p(|x|, \chi, \theta), \tag{2.42}$$

which is solved with inner boundary condition

$$p(r_0, t) = p_{\mathrm{NS}}(r_0, t), \tag{2.43}$$

where $p_{\mathrm{NS}}(r_0, t)$ is the solution of the Navier Stokes equations on the circle $|x| = r_0$; and non-reflecting boundary condition at the outer boundary.
In spherical coordinates, the solution can be written as

$$p = \sum_{l=0}^{\infty} \sum_{m=-l}^{l} R_l^m(|x|, t) Y_l^m(\chi, \theta), \tag{2.44}$$

where

$$Y_l^m(\chi, \theta) = \sqrt{\frac{2l+1}{4\pi} \frac{(l-m)!}{(l+m)!}} P_l^m(\cos\chi) \mathrm{e}^{\mathrm{i}m\theta}, \tag{2.45}$$

are the spherical harmonics, and P_l^m is the associated Legendre polynomial. m and l are azimuthal number and polar number, respectively.

The coefficient $R_l^m(|x|,t)$ is solved with a one-dimensional wave equation

$$\frac{\partial^2 R}{\partial t^2} - \frac{1}{|x|}\frac{\partial^2(|x|R)}{\partial |x|^2} + \frac{1}{|x|^2}l(l+1)R = 0, \tag{2.46}$$

and on the inner boundary, the DNS solution on a sphere of radius $10R$ is decomposed into spherical harmonics

$$R_l^m(r_0,t) = \int_0^{2\pi}\int_0^{\pi} p_{\rm NS}(r_0,t)Y_l^m(\chi,\theta)\sin\chi d\chi d\theta \tag{2.47}$$

The spatial discretization and time marching scheme are the same as the Navier-Stokes equation solver. However, since the relevant sound wave has much larger wavelength than the near field fine scale, larger grid spacing and time step can be used. In the present study, we use a grid size of $0.2R_0$ and time step of $0.1R_0/a_\infty$.

2.4 Generation of a vortex ring

There are several ways to model the vortex generation process. A given vorticity distribution and its corresponding velocity field may be used as the initial condition (Stanaway & Cantwell 1988). A vortex sheet model was implemented by Nitsche & Kransy (1994) to reproduce vortex generation experiments by Didden (1979) for small stroke ratios. James & Madnia (1996) used numerical solutions of the low Mach number Navier-Stokes equations for small stroke ratios. Another method is to prescribe an axial velocity profile $U_x(r)$ at an inlet, in an attempt to model the injection of fluid through the nozzle of the experimental apparatus (Verzicco et al. 1996).

An alternative method of numerically generating vortex rings is to apply a non-conservative force directly in the equations of motion. We view this as a "generic" vortex ring generator, independent of any particular geometry, but note that in the laboratory, such a force could in principle be generated by imposing currents in the fluid with a magnetic field. This method has previously been used, for impulsive forces, in order to generate vortex rings with certain desired properties (McCormack & Crane 1973, Swearingen, Crouch & Handler 1995), This is the method adopted in the present study. The same method was used by Mohseni, Ran & Colonius (2001) to study vortex ring pinch-off.

2.4.1 Generation of vortex rings with non-conservative body force

The body force is aligned with the axial coordinate of a cylindrical-polar coordinate system (x, r) and has the form:

$$f_x(r, x, t) = C\ F(t)\ G(x)\ H(r), \tag{2.48}$$

where C is an amplitude constant with units of circulation, and F, G are functions with units of inverse time and inverse length, respectively, and H is nondimensional function.

For the temporal profile, we use a regularized step function for F:

$$F(t) = -\frac{1}{2T}\big(\tanh[\alpha_t(t_0 - t)] + \tanh[\alpha_t(t - t_0 - T)]\big), \tag{2.49}$$

where T is the duration of the force and α_t is a time scale which controls the smoothness in turning on and off the force. When α_t is too large, a strong dipolar acoustic wave will be generated and contaminate the acoustic field of the vortex ring. We have experimented with different values of α_t, and the results presented below use $\alpha_t = 0.4R^2/C$, where R is the radial extent of the forcing region.

The functions G and H control the spatial variation of the flow generated by the force. For the radial distribution, we use:

$$H(r) = \frac{1}{2}\ \mathrm{erfc}\big(\sqrt{\alpha}\ \frac{r - R}{\alpha_r}\big), \tag{2.50}$$

where α is a nondimensional constant discussed below. This a smoothed "top-hat" function. α_r is analogous to the boundary layer thickness at the exit of the nozzle in experiments. It controls the shear layer thickness of the resulting flow, therefore the thickness of the vortex ring core. For the axial distribution, we again use a regularized delta function:

$$G(x) = \frac{\sqrt{\alpha}}{\alpha_x\sqrt{\pi}}\ e^{-\alpha(\frac{x}{\alpha_x})^2}, \tag{2.51}$$

where α_x controls the axial extent over which the force is smeared. The axial, radial and temporal profile of the forcing function is shown in figure 2.3.

With a short forcing duration, the azimuthal vorticity field generated by the force is

given, to leading order (e.g., Saffman 1992), by:

$$\omega_\theta(x,r) = -\frac{\partial f_x(x,r)}{\partial r}. \tag{2.52}$$

Thus for an impulsive force, the vorticity field is an approximately Gaussian distribution (for $\alpha_r \ll R$):

$$\omega_\theta = \frac{C\alpha}{\pi\alpha_x\alpha_r}\ e^{-\alpha\left((\frac{r-R}{\alpha_r})^2+(\frac{x}{\alpha_x})^2\right)}, \tag{2.53}$$

which is the rationale for the specific functional dependence chosen for H and G given above. Weigand & Gharib (1997) showed that vortex rings generated by a piston/cylinder arrangement also possess an approximately Gaussian vorticity distribution in their core. Note that the constant factor $\alpha = 1.25643\cdots$ is used so that the maximum tangential velocity in the core is located at $r = R \pm \alpha_r$ when $\alpha_r \ll R$. With nonimpulsive force, the elongated vortex layer will later roll up into a thicker vortex ring, and its properties are independent of α_x and α_r.

To relate the parameters in vortex ring generation with a non-conservative force and the cylinder-piston mechanism, we can calculate the equivalent L/D number from the forcing with specific amplitude C and duration T. The total impulse generated by the forcing is

$$I = \int_0^T F(t)dt \cdot \int f_x(x,r)dv. \tag{2.54}$$

$f_x(x,r)$ is integrated within the volume where the force is applied. On the other hand, the total impulse produced by pushing a slug of fluid in a cylinder with piston velocity U_p during time T is,

$$I = \pi R^2 L U_p = \pi R^2 L^2/T, \tag{2.55}$$

where R is the radius of the cylinder, $U_p = L/T$. Plugging Eq. (2.48) and (2.54) into Eq. (2.55), we obtain

$$\frac{L}{D} = \frac{L}{2R} = \frac{T_{eff}}{2R^2}\sqrt{\frac{C}{\pi}\int G(x)H(r)dv}, \tag{2.56}$$

where $T_{\text{eff}} = \int_0^T F(t)dt$. The equivalent piston velocity U_p is given by

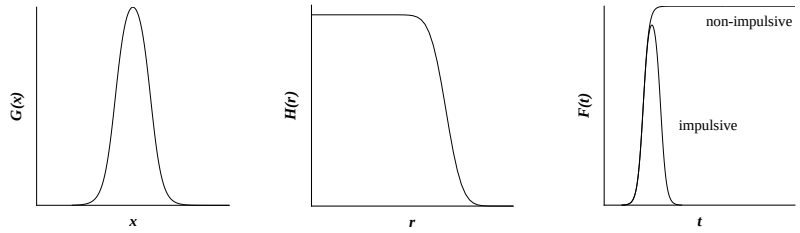

Figure 2.3: Forcing function, a) axial profile; b)radial profile; c) temporal profile.

$$U_p = \frac{L}{T_{\text{eff}}} = \frac{1}{R}\sqrt{\frac{C}{\pi}\int G(x)H(r)dv}. \tag{2.57}$$

With the same forcing profile $G(x)$ and $H(r)$, the piston velocity varies linearly with $\sqrt{C}$ and the equivalent L/D is determined by $T_{\text{eff}}\sqrt{C}$.

In what follows, we characterize the ring by its properties upon completion of the formation stage. There are four nondimensional parameters that control the formed ring: the ratio of core to ring radius, σ/R; the circulation of the formed vortex ring, $\Gamma T/R^2$, which can be mapped to a specific L/D in the cylinder/piston mechanism; the circulation-based Reynolds number, Γ/ν (where ν is the constant kinematic viscosity), and a Mach number, for example Γ/Ra_∞. For convenience, we define a nominal translation Mach number M that is based on the estimated average translation speed of the ring. With the chosen forcing parameters in the current studies, the corresponding stroke length is about $L/D = 1.5$, and the nominal translational Mach number of the vortex ring is varied from 0.14 to 0.28. Once formed, the laminar vortex ring has an initial Reynolds number Γ/ν that varies from 1260 to 4500, and a core thickness around $\sigma/R = 0.34$. Unless otherwise noted, quantities are made nondimensional with circulation Γ and vortex ring radius R. For example, the nondimensional time is defined as $\tilde{t} = t\Gamma/R^2$.

2.4.2 Introduction of azimuthal disturbances

In the present study, azimuthal instability was excited by adding azimuthal perturbations to the spatial distribution of the forcing function. We imposed a random radial displacement on the toroidal radius of the ring $r'(\theta) = r_0\,[1 + \varepsilon(\theta)]$. It should be noted that the disturbance field was divergence free in order to minimize the sound generated by the force.

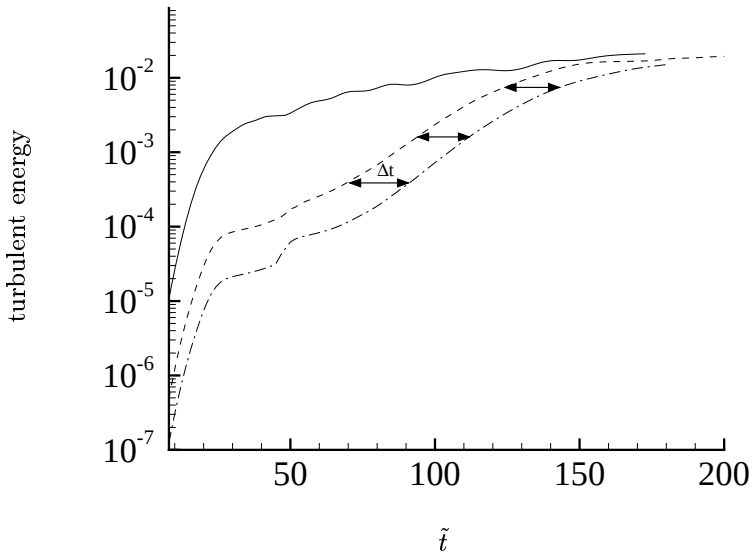

Figure 2.4: Temporal evolution of turbulent energy for different initial disturbance, scaled with mean kinetic energy. ε = (——) 0.05, (----) 0.02, (—·—) 0.01. For case 3, 5, 6 in Table 3.1

When ε is too large, nonlinear effects appear right after vortex ring formation. In Figure 2.4 we plot the evolution of turbulent kinetic energy, scaled with mean kinetic energy. We found that when ε is less than 0.02, the growth rate of the linear instability is independent of the perturbation level, the difference in initial perturbation levels only leads to a time shift in the saturation of turbulent energy. In the simulations presented below, we use $\varepsilon = 0.01$.

In the present numerical studies, we added a uniform flow with speed M, in the direction opposite to the vortex ring translation that was estimated as the average translation speed of the ring. In this way the vortex structure was (approximately) centered in the computation domain.

2.5 Parallel implementation

To implement the numerical method on distributed memory machines, MPI (Message Passing Interface) was used to accomplish communication between individual processors. The computational domain was decomposed along the axial direction and the azimuthal direction. Specifically, with N_p processors, the full $N_x \times N_r \times N_\theta$ domain was first decomposed

into N_p parts of $N_x \times N_r \times N_\theta/N_p$, and the axial and radial derivatives were computed on each processor simultaneously; then the full domain was decomposed into N_p parts of $N_x/N_p \times N_r \times N_\theta$ to calculate azimuthal derivatives. Transposing between these two decompositions take place twice per Runge-Kutta sub-step.

2.6 Grid convergence

In the present study, the highest Reynolds number is $Re = \Gamma/\nu = 4500$. The equations were discretized with as many as $240 \times 120 \times 128$ mesh points in the axial (x), radial (r), and azimuthal (θ) directions, respectively. The grid spacing is $\frac{1}{33}R$ in the vortex ring region, and the time step is $0.012R/a_\infty$ where a_∞ is the sound speed. We compared the numerical results of the fine grid with a reduced grid size of $160 \times 80 \times 64$, and plots in Figure 2.5. Results from two grid are identical except at time $\tilde{t} = 302$, when the vortex ring moves to the stretched grid, and the grid spacing with the reduced grid size become too large to resolve the fine scales. It shows that at this Reynolds number, the transition and turbulent stages of the vortex ring are well resolved on the $240 \times 120 \times 128$ mesh.

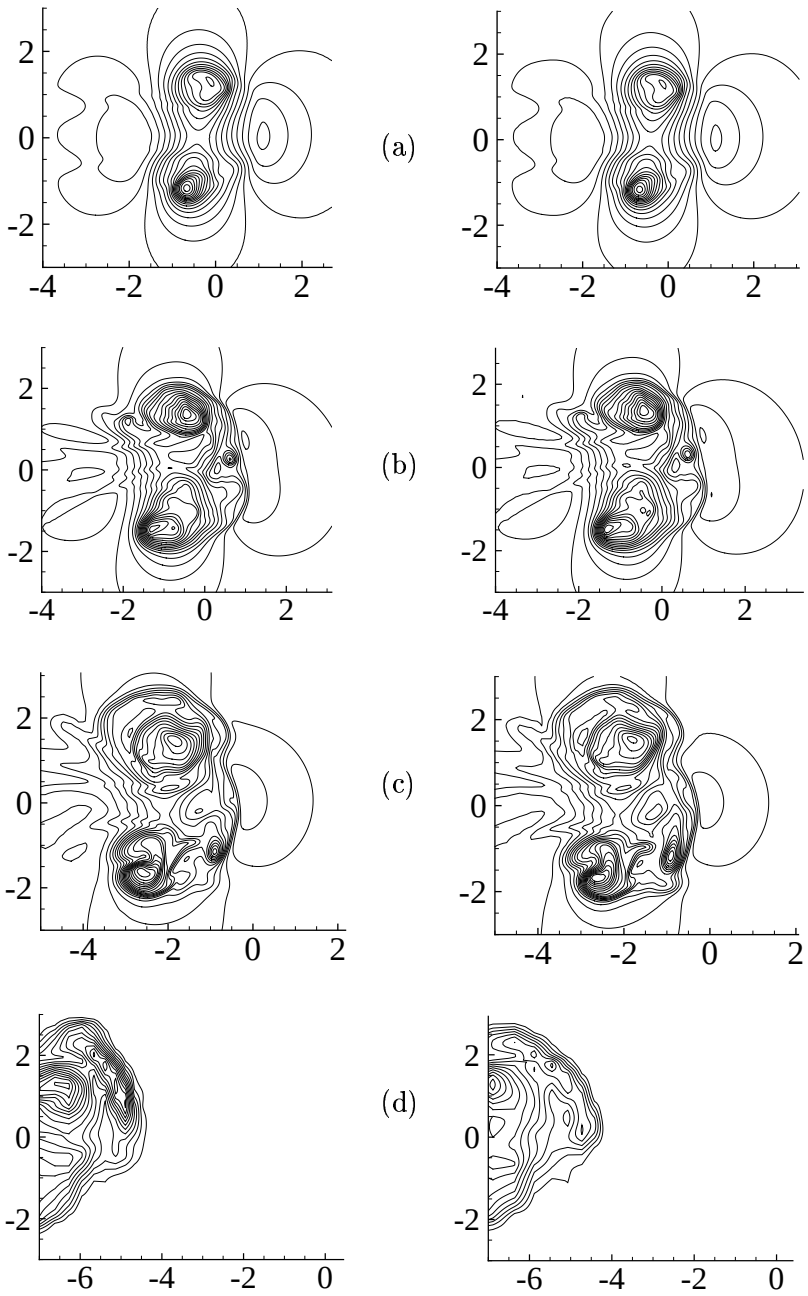

Figure 2.5: Density contour $\rho - \rho_\infty$ with grids $240 \times 120 \times 128$ (left) and $160 \times 80 \times 64$ (right), and with 20 evenly spaced contour levels. (a) $\tilde{t} = 43.2$, min.$= -0.27$, max.$= 0.06$; (b) $\tilde{t} = 130$, min.$= -0.13$, max.$= 0.02$; (c) $\tilde{t} = 216$, min.$= -0.10$, max.$= 0.01$; (d)$\tilde{t} = 302$, min.$= -0.05$, max.$= 0.01$.

Chapter 3

Instability, Transition and Turbulent Decay

In this chapter, we examine results for the near field (hydrodynamic field) evolution during instability, transition and turbulent decay. Some unresolved issues related to the vortex ring instability and transition are discussed. During the fully turbulent stage, detailed information on the mean flow and turbulent statistics is presented. The parameters for all the cases considered are given in Table 3.1. The cases with smaller domain $6R \times 3R$ are used to study the vortex ring instability and transition, whereas cases with larger domain calculate both near field and far field.

3.1 Choice of Reynolds number

Our choice of Reynolds number is dictated by requiring a high enough value to produce a turbulent ring, but sufficiently low to keep computational run times reasonably short. Saffman (1978) has showed that the vortex ring instability is dependent on the Reynolds number. When the Reynolds number is sufficiently small, the vortex ring will remain laminar (Didden 1979). Previous studies (Maxworthy 1972, Didden 1979, Rosenfeld, Rambod & Gharib 1998) have shown that the limiting Re for the vortex ring instability is in the range of 1000 to 1800, depending on the formation conditions. For unstable vortex rings, Shariff et al. (1994) found a viscous correction factor for the growth rate, $1 - \alpha(\sigma)/Re$, where σ is the core thickness. Thus when Re is lower than a critical value, the growth rate becomes negative and the ring will remain laminar. Since the critical Re depends on formation conditions, we examine results for Reynolds number $Re = \Gamma/\nu = 1260$, 2880 and

Case	Γ/ν	M	ε	$N_x \times N_r \times N_\theta$	$L_x \times L_r$	N_{ens}
1	1260	0.14	0.01	$208 \times 101 \times 128$	$6R \times 3R$	1
2	2880	0.14	0.01	$208 \times 101 \times 128$	$6R \times 3R$	1
3	4500	0.14	0.01	$208 \times 101 \times 128$	$6R \times 3R$	1
4†	4500	0.14	0.01	$208 \times 101 \times 32$	$6R \times 3R$	1
5	4500	0.14	0.02	$208 \times 101 \times 128$	$6R \times 3R$	1
6	4500	0.14	0.05	$208 \times 101 \times 128$	$6R \times 3R$	1
7	4500	0.14	0.01	$288 \times 145 \times 128$	$40R \times 20R$	5
8	4500	0.28	0.01	$240 \times 121 \times 128$	$24R \times 12R$	15
9	4500	0.28	0.01	$160 \times 81 \times 64$	$24R \times 12R$	1
10	4500	0.28	0.01	$480 \times 161 \times 128$	$50R \times 16R$	1

†, only $n = 8$ is excited, and computational domain is $\pi/4$ in azimuthal direction.

Table 3.1: Parameters for computations.

4500. Figure 3.1 shows the evolution of kinetic energy associated with azimuthal modes 1, 2, 4, 8 and 16, scaled with total initial kinetic energy E_0 of the formed vortex ring, for each case. The kinetic energy levels reach 10^{-4} after $\tilde{t} = 40$, when the vortex ring is formed. $\tilde{t}$ is defined by $t\Gamma/R^2$. The energy then evolves at different rates. For case 1, lower modes remain at this level, while higher modes decay rapidly, and the ring remains laminar throughout the simulation. At $Re = 2880$ and 4500, the energy grows and saturates at a level around 10^{-2}, and the rings go unstable and transition to turbulence. The higher Reynolds number reaches saturation in shorter time. We use $Re = 4500$ for the rest of the study.

Next we present the evolution of total circulation for case 8. Circulation is calculated from line integral of axial velocity along the centerline. Three different realizations, along with the average of the entire ensemble, are shown in Figure 3.2. The evolution of the vortex ring can be roughly separated into 4 stages. During stage I, the vortex ring is formed by application of the non-conservative body force, and the circulation grows linearly. The forcing also produces a spherically spreading dipolar acoustic wave. By applying the force slowly on the acoustic timescale, the amplitude of this acoustic transient is minimized. During stage II, three-dimensional instabilities occur while the overall circulation decays slightly due to (laminar) viscous diffusion across the centerline. Depending on the rate at which the body force is applied, there is overlap between stages I and II with formation and instabilities occurring simultaneously. The azimuthal vorticity field after ring formation is plotted in Figure 3.3. Toward the end of stage II, nonlinear interactions of the unstable

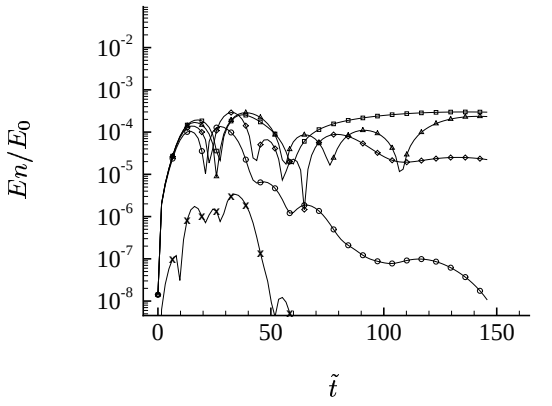

(a)

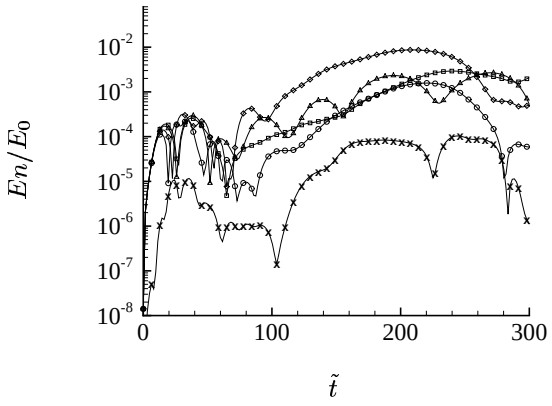

(b)

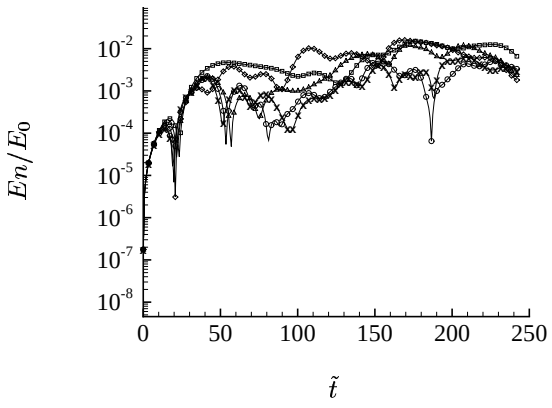

(c)

Figure 3.1: Temporal evolution of kinetic energy, scaled with total kinetic energy E_0, a) $Re = 1260$; b) $Re = 2880$; c) $Re = 4500$. $n =$ (□) 1, (△) 2, (◇) 4, (○) 8, (x) 16.

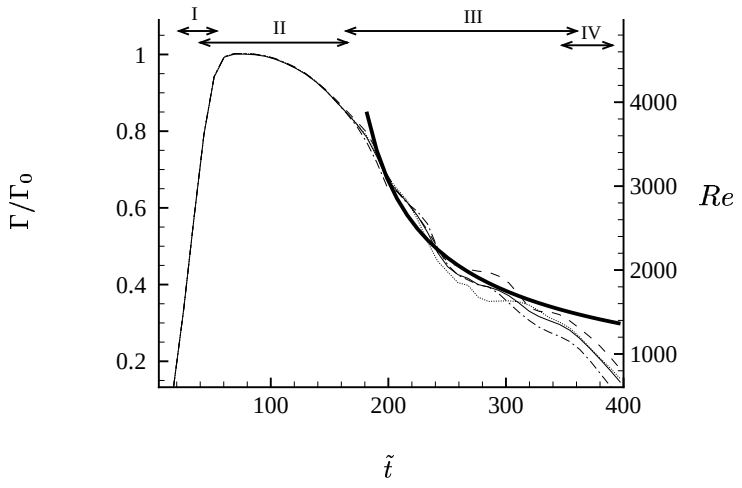

Figure 3.2: Decaying of total circulation and Reynolds number of 3 vortex ring realizations of case 8 (----), (—·—), (·····), and the ensemble average (——). The thicker line is $\sim \tilde{t}^{-1/2}$. Stage I, II, III and IV are described in this section.

modes cause transition to turbulent flow. Until this time there are no significant differences in circulation amongest the ensemble. During stage III, the flow is turbulent and circulation decays at faster rate due to viscous diffusion and cancellation of opposite-signed vorticity across the ring axis (brought about by turbulent mixing and the shedding of vorticity from the ring). The decay approximately follows a $t^{-1/2}$ law predicted by Glezer & Coles (1990), and shows dispersion between individual runs. As the circulation of the ring decays, its translational velocity becomes smaller than the nominal translation velocity and the ring moves upstream relative to the computational domain. During the final stage IV, part of the vortex ring exits the computational domain and the circulation decreases rapidly.

3.2 Three-dimensional vortex ring instabilities

Three-dimensional stochastic perturbation is introduced during vortex ring formation, and leads to different oscillations. Linear oscillations of the vortex ring can be described with

$$\tilde{q} = q(r,z)\exp(in\theta - i\Omega t), \tag{3.1}$$

and are characterized by azimuthal wave number n, a radial mode number, j, which indicates the number of vorticity layers in the radial direction, and rotation rate Ω. In addition,

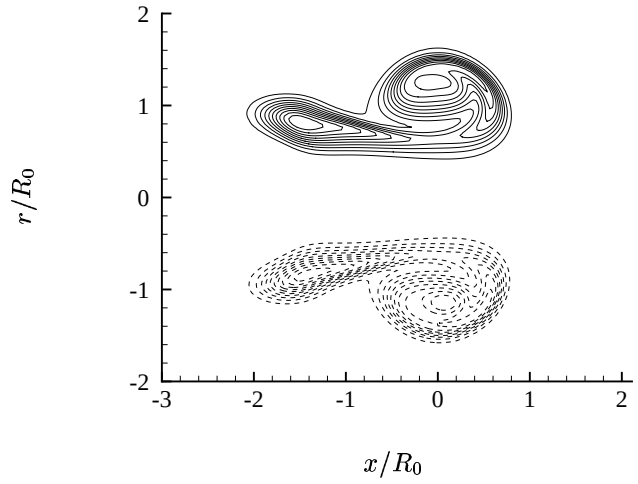

Figure 3.3: Side view of azimuthal vorticity at $\theta = 0$ and $\theta = \pi$ just after formation, with 20 evenly spaced contours between -2.4 and 2.4, $\tilde{t} = 43.2$.

the vortex core is strained by the geometry of the ring. If Ω is smaller than the strain rate ϵ, the mode become unstable. When the flow is viscous, higher radial modes will usually be damped and the unstable modes with the lowest mode number will be amplified.

To study the instability process and compare with theory, a vortex ring with M=0.14 (case 3) is simulated; the forcing time is made shorter in order to separate the ring formation (stage I) and the instabilities (stage II). The instability can be visualized with contours of azimuthal vorticity, shown in Figure 3.4. At earlier times $\tilde{t} = 3.7$ and 15.0, only the boundary of the vortex core is distorted, the radial profile of vorticity has only one peak, and no single azimuthal mode is dominant. However, after time $\tilde{t} = 30.0$, when the vortex ring has moved about 2 diameters downstream, the radial profile of vorticity develops two peaks, illustrating the second radial mode. At one section, the contours in the inner region of the core are bent toward the ring axis, whereas contours at the outer region are bent outward. A strong response with $n = 7$ is evident. This mode is non-rotating, and its amplitude increase in time. At time $\tilde{t} = 71.2$, the distortion of the iso-vorticity contours become comparable with the core radius, and the instability reaches the nonlinear phase. The peak vorticity level also increases due to intensification by vortex stretching.

Figure 3.5 plot the end view of azimuthal vorticity at time $\tilde{t} = 16.5$, for azimuthal mode $n = 4$ to 7. Six layers of vorticity develop in the radial direction, showing radial modes $j =$ 3. According to the heuristic linear instability model of Widnall & Tsai (1977), a particular

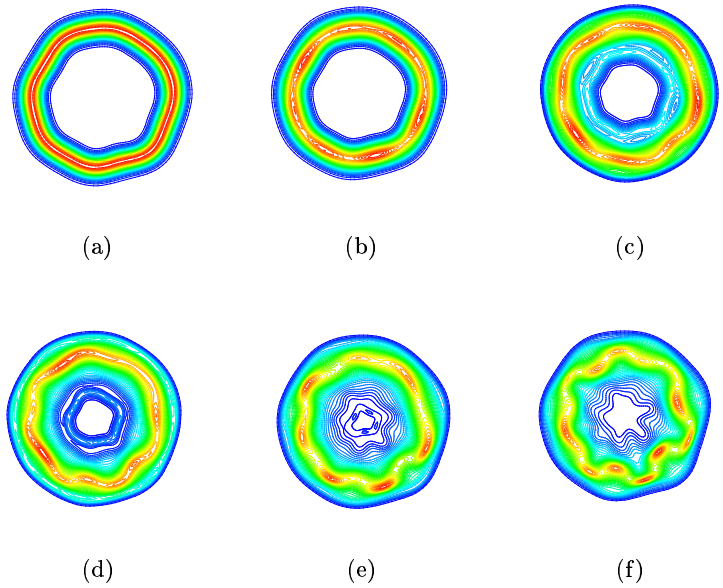

Figure 3.4: Contours of azimuthal vorticity on a plane across the ring axis. $\tilde{t}$ = (a) 3.7, (b) 15.0, (c) 30.0, (d) 45.0, (e) 60.0, (f) 71.2, with contour levels in a): max.=0.022, min.=0.001, increment=0.001; in (b) to (f), max.=0.7, min.=0.02, increment=0.02.

azimuthal number is unstable only for a certain radial mode. For example, $n = 5$ to 8 should be unstable to a second radial mode ($j = 2$), $n = 9$ and 10 should be unstable to the third radial mode ($j = 3$). These unstable modes will grow and other modes will be damped during the linear stage. Figure 3.6 shows an end view of the contours of azimuthal vorticity and three-dimensional isosurface at $\tilde{t} = 71.2$, illustrating the radial structure of each azimuthal mode. The radial profiles of vorticity for each azimuthal modes at $\theta = 0$ are shown in Figure 3.7. The group $n = 5$ to 8 has structure with $j = 2$, and $n = 9$ to 11 shows higher radial mode. The contour levels show that modes $n = 6$ and 7 are dominant.

According to the inviscid theory, the unstable azimuthal wavelengths are proportional to core radius σ so that $k\sigma$ is a constant κ for these waves ($\kappa = 2.5$ for second radial mode, 4.35 for third radial mode, etc.). If an integer number of these waves will fit on the ring, the ring will be unstable to that number of waves. For a given core to ring ratio μ, $n = \kappa/\mu$, therefore the most amplified azimuthal wave number of a second-radial mode is given by

$$n = 2.51R/\sigma. \tag{3.2}$$

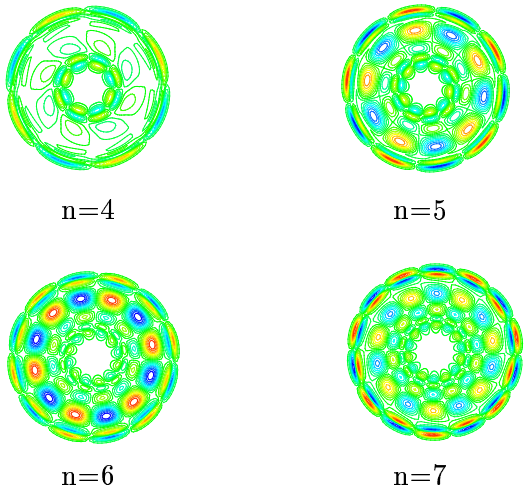

Figure 3.5: Mode shape plots for $n = 4$, 5, 6, 7 at $\tilde{t} = 9.18$, with 20 contours between the $\omega_{\max}$ and $-\omega_{\max}$. $\omega_{\max}$ =, a) 0.044, b) 0.035, c) 0.037, d) 0.027.

In our case, $\sigma/R = 0.34$, which gives $n = 7.4$, and agrees with the numerical result. To demonstrate the dependence of azimuthal wavenumber on core thickness, Figure 3.8 (a) plots the azimuthal and radial distribution of vorticity at three axial stations at $\tilde{t} = 69.1$, for one run in case 8. At this moment the leading vortex ring is separating from the trailing vortices. Station I is across the center of the leading vortex, where the core is thick, and six waves form along the ring. Station II is near the separation point, where the vortex layer is the thinnest, and about 14 to 15 waves develop. Location III is across the center of the trailing vortex ring, which is thinner than the leading ring. At this station the wave number is around 11. Radial vorticity distributions at these three stations are depicted in Figure 3.8 (b), which show the relative thickness of vortex layers. The local vortex ring radius is estimated to be the distance from centerline to the outer boundary of vorticity, which gives $R = 1.9R_0$ at station I, $1.1R_0$ at station II and III. The core radius σ is estimated to be half the distance between maximum tangential velocity across the core (Figure 3.8 (c)), and we obtain $\sigma = 0.75R_0$, $0.20R_0$ and $0.28R_0$ at station I, II and III, respectively. From Eq. (3.2), the number of azimuthal waves at the three stations are predicted to be 6, 14, 10, which agrees well with simulation results. In laboratory, the number of waves developed around the vortex ring can be used to estimate the core thickness using Eq. (3.2) (Maxworthy 1977). The dependence of unstable wavenumber on ring core thickness also explain why the vortex ring will stay laminar at low Reynolds number: with higher viscous

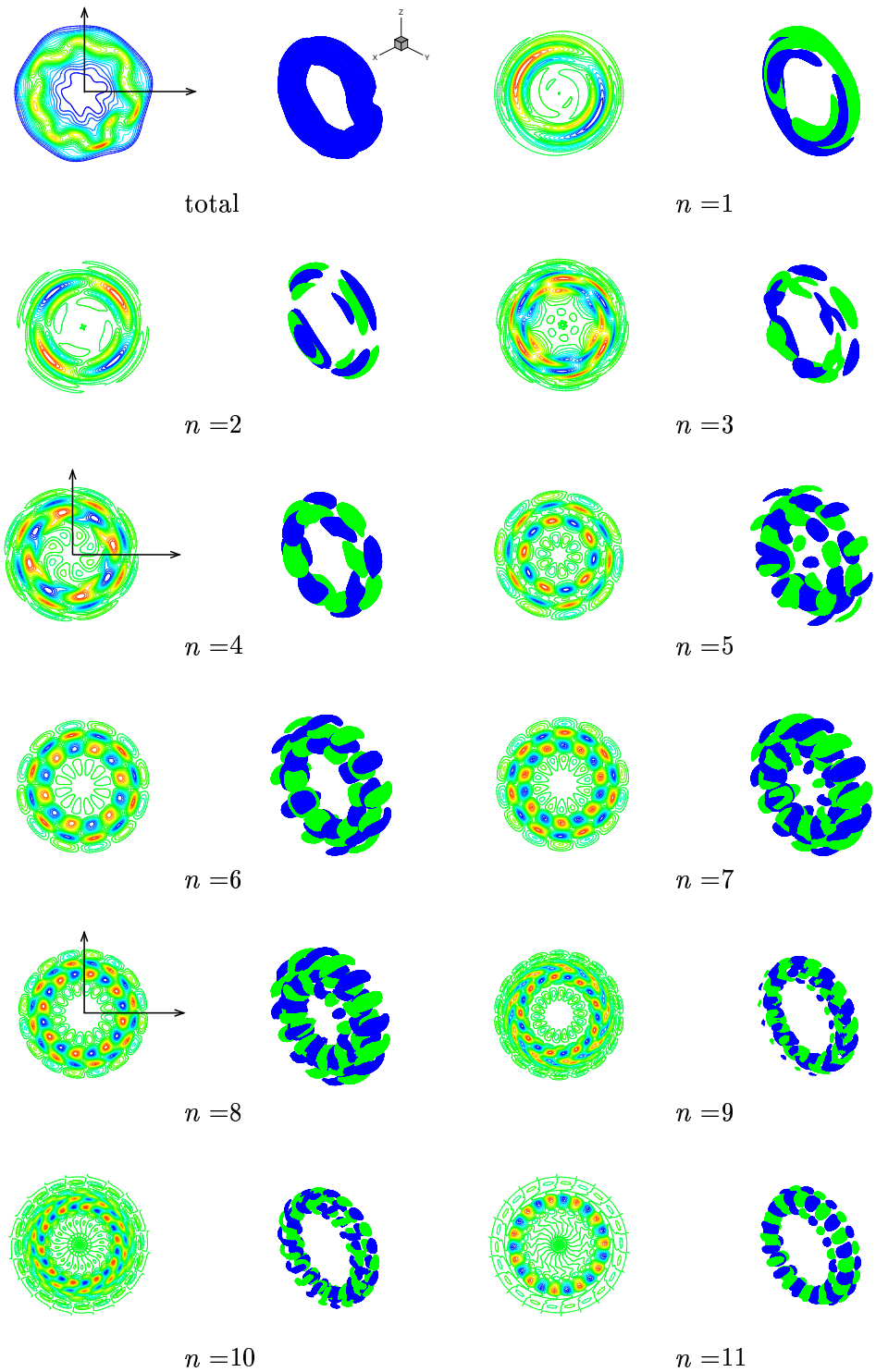

Figure 3.6: Left: mode shape plots of ω_θ at $\tilde{t} = 71.2$, with 20 contours between $\omega_{\max}$ and $-\omega_{\max}$ except for total vorticity. Total: min.=0.04, max.=0.84, $n = 1$ to 11: $\omega_{\max} = 0.068$, 0.065, 0.028, 0.048, 0.071, 0.13, 0.11, 0.071, 0.015, 0.011, 0.037. Right: three-dimensional isosurface.

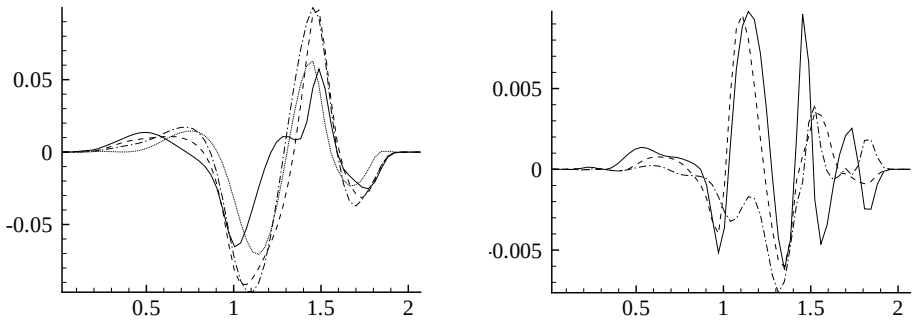

Figure 3.7: Radial profile of vorticity for different azimuthal modes. a) (——) $n = 5$, (----) $n = 6$, (—·—) $n = 7$, (·····) $n = 8$. b) (——) $n = 9$, (----) $n = 10$, (—·—) $n = 11$.

diffusion of the core, growth of the core with time could continually keep the ring from remaining unstable to a given mode long enough to be noticeably amplified (Saffman 1978).

To demonstrate the temporal evolution of the instability waves, the kinetic energy associated with different azimuthal modes are plotted in Figure 3.9. Up to time $\tilde{t} = 75$, the evolution goes through three phases: transient, linear, and early nonlinear. All the modes have the same initial perturbation level, and oscillate during the early transient stage. However, after $\tilde{t} = 30$, linearly growing eigenmodes n= 6, 7 and 8 begin to dominant, whereas other modes start to decay. The most amplified mode during the linear stage is n=7. These unstable modes extract energy from the axisymmetric mean flow, and feed into other modes during the later nonlinear stage.

3.3 Turbulent transition

The nonlinear and transition stages take place at about 6 to 8 ring diameters downstream. During this stage, several phenomena occur: harmonics of the most linearly amplified waves (e.g., n =12 to 16, 24 to 32, etc.) are amplified; lower azimuthal modes arise from nonlinear interactions of adjacent unstable modes; and the three-dimensional disturbance of vorticity leads to the growth of azimuthal velocity and streamwise vorticity. In experiments, Maxworthy (1977) found that as the azimuthal waves grow, the initially sinusoidal waves take on an increasingly sawtoothed form with a typical amplitude to wavelength ratio of up to 1/2. The wave then breaks into a cascade of chaotic vortices and generate intense stirring

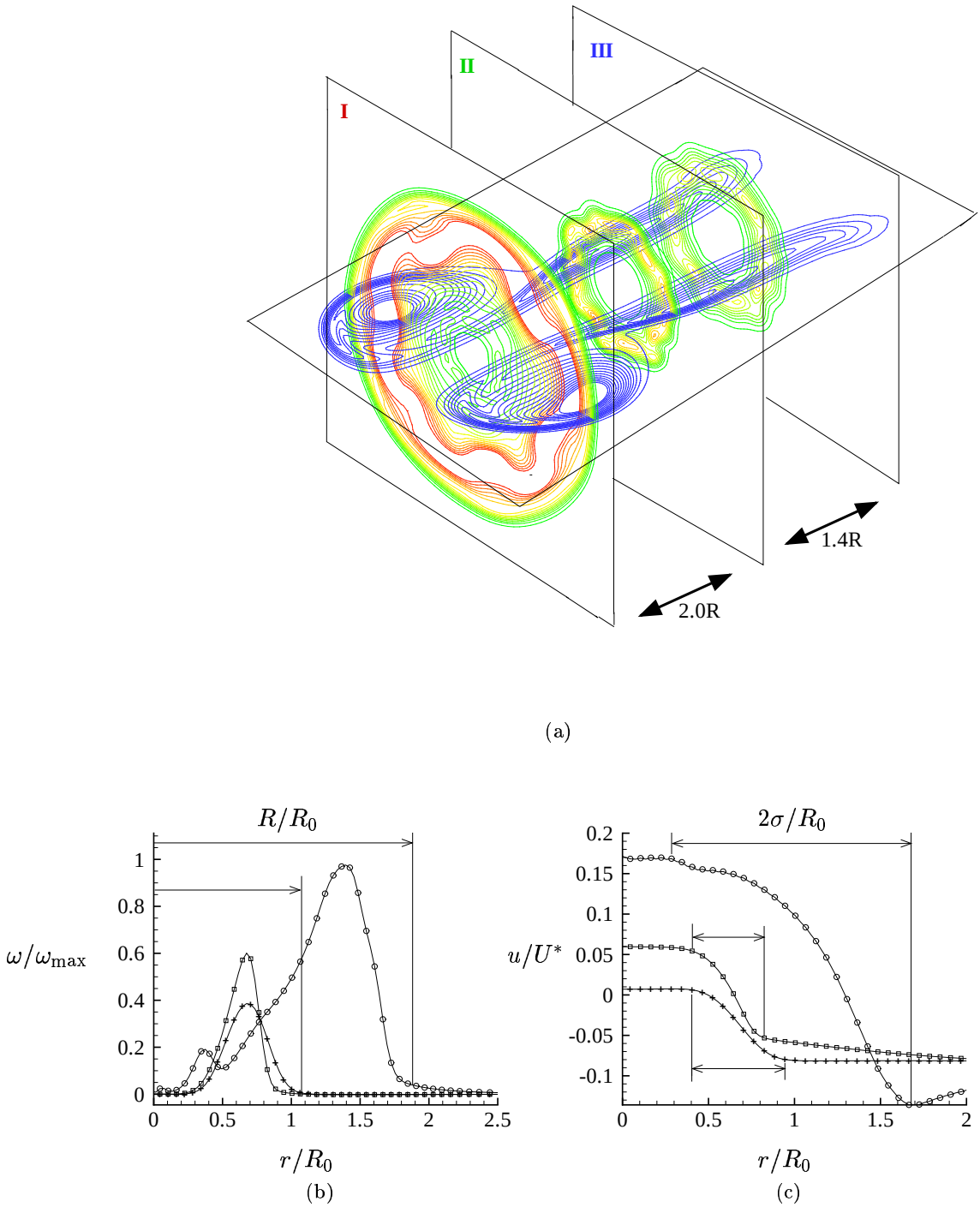

Figure 3.8: a) Azimuthal wave numbers at three axial locations at $\tilde{t} = 69.1$; b) radial vorticity distribution at the three axial stations; (c) tangential velocity across the core, ($\circ$) station I, ($\square$) station II, ($+$) station III.

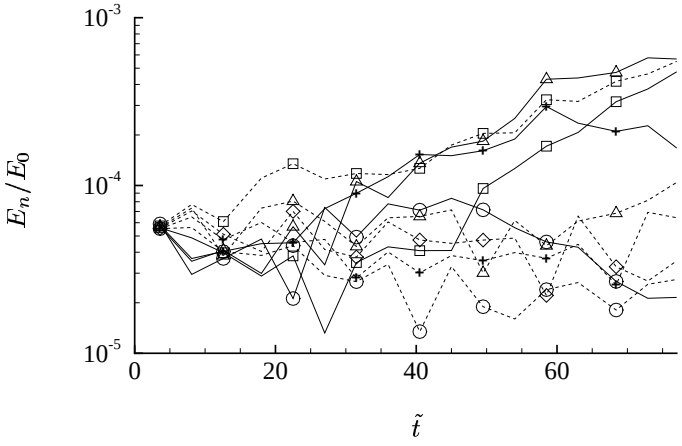

Figure 3.9: Evolution of kinetic energy during linear stage, scaled with total energy E_0 (----), $n = 1$ to 5: (□),1; (△), 2; (⋄), 3; (+), 4; (○), 5; (——), $n = 6$ to 9: (□), 6; (△), 7; (+), 8; (○), 9.

of ambient fluids. He also discovered the growth of lower modes, and suggested that these low-order modes of the vorticity are most efficient in turbulent mixing because the Biot-Savart velocity induced by higher order modes decays much faster from the core. These lower modes of unsteadiness entrain ambient irrotational fluid and detrain weakly vortical fluid into the wake of the ring.

The process is visualized in Figure 3.10 for case 8 ($M = 0.28$). After the vortex ring is formed, some extra vorticity is shed from the leading vortex ring. In the mean time, unstable bending modes begin to grow, as shown in Figure 3.10 (b), and six waves appears around the vortex ring. At $\tilde{t} = 86.4$, higher harmonics with n =12 appears due to nonlinear effect. These modes also have a finer radial structure. The higher radial modes change the distribution of vorticity inside the core, with one vorticity peak bent inward, and the next vorticity peak bent outward, and cause the bulging shape in the isosurface contour. The concentration of vorticity is not evenly distributed around the ring, with the top region of the vortex ring more intensified and inducing a higher strain on the vorticity around it. The increased strain field further accelerate the instability at the upper corner and finally cause the vortex ring to breakdown. In addition, regions with lower vorticity around the periphery of the vortex ring form hairpin vortices and start to detach from the vortex ring, as depicted in Figure 3.10 (e) (f).

Figure 3.11 plots contours of vorticity normal to an axial slice of the ring ($\theta = 0$ and

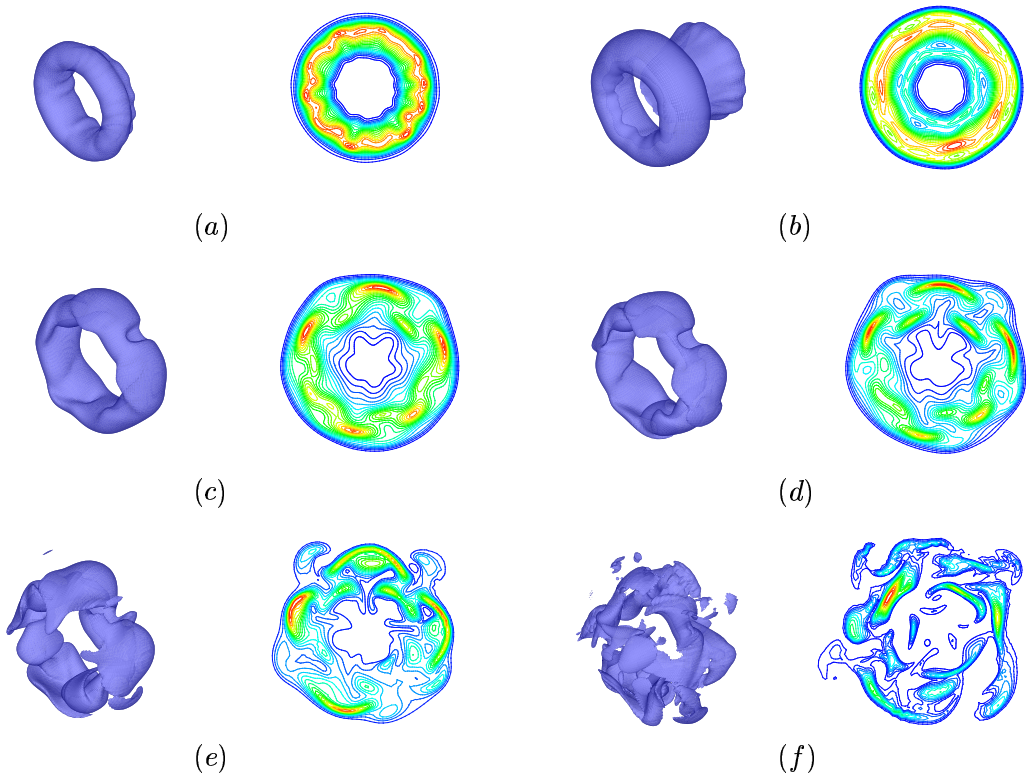

Figure 3.10: Left, isosurface of vorticity level 0.5 at $\tilde{t} = 25.9, 43.2, 86.4, 103.6, 129.6, 172.8$. Right, end view of vorticity with 20 evenly spaced contours between 0 and the maximum vorticity. $\omega_{\max} =$, a) 1.6, b) 1.2, c) 1.3, b) 1.6, e) 1.6, f) 2.2.

(a)

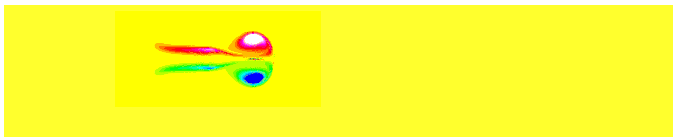

(b)

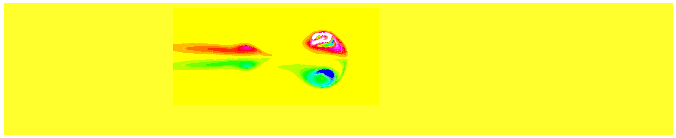

(c)

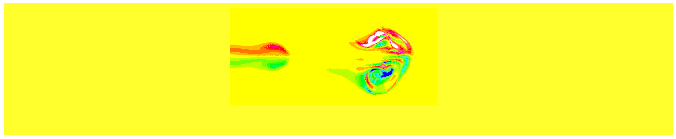

(d)

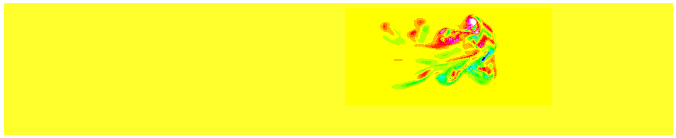

(e)

(f)

Figure 3.11: Side view of the temporal evolution of azimuthal vorticity at $\theta = 0$ and $\theta = \pi$, with 22 evenly spaced contours between -0.5 and 0.5 at $\tilde{t} =$ a) 43.2, b) 86.4, c) 130, d) 173, e) 259, f) 346.

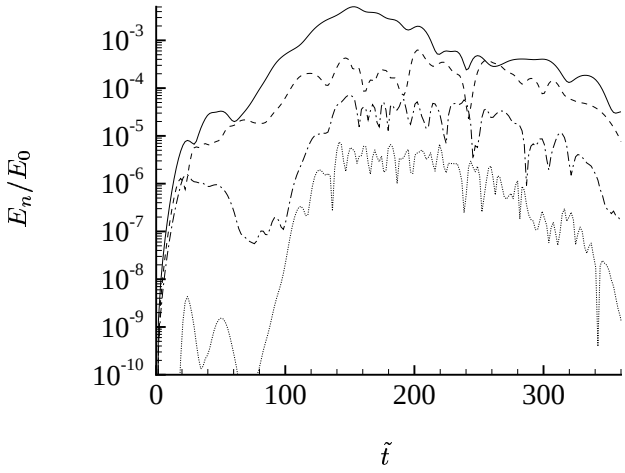

Figure 3.12: Temporal evolution of the modal energy of $n = 8$ and harmonics. $n = 8$ (——); 16 (----) 16; 32 (—·—).

$\theta = \pi$). During the initial stage, the vorticity is symmetric but with opposite sign in the upper and lower core, and the contour levels decrease smoothly from the center of the core to the outer region. This indicates that the core structure is laminar and concentrated. At $\tilde{t}$ =130 and 173, the deformation of the upper and lower core becomes asymmetric, and shows signs of turbulent breakup, which is indicated by the increased concentration of vorticity in the periphery of the core region. This vorticity will be later shed into the wake. At later time, finer structure develops, vorticity continuously shed into the wake region. The vortex shedding is asymmetric, and causes dispersion in the vortex ring trajectory. In this realization, the vortex ring tilts upward.

Figure 3.12 plots the azimuthal modes of the kinetic energy for $n = 8$ and its harmonics 16, 32. Mode $n = 8$ begins to grow exponentially after $\tilde{t} = 20$, $n = 16$ also increases, but at lower rate. The harmonic $n = 32$ decays in the beginning, then begin to grow after $\tilde{t} = 80$ as a result of nonlinearity. All the modes saturate around $\tilde{t} = 140$, when the vortex ring breaks down and transitions to turbulence. The results indicate that the onset of turbulence in the core is associated with harmonics of the unstable mode, excited in the form of a discrete energy cascade. The energy of all the modes begin to decay at $\tilde{t} = 200$, after the transition is finished. The turbulent vortex ring has much larger energy dissipation rate than the laminar rings.

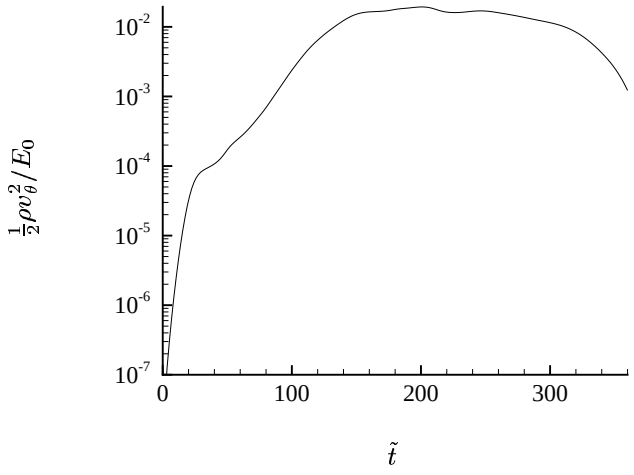

Figure 3.13: Evolution of azimuthal component of kinetic energy $\frac{1}{2}\rho v_\theta^2$ scaled with total kinetic energy $E_0 = \frac{1}{2}\rho(v_z^2 + v_r^2 + v_\theta^2)$, ensemble-averaged with $N = 12$.

3.4 Azimuthal flow and streamwise vorticity

To study the growth of the azimuthal velocity, Figure 3.13 shows the evolution of azimuthal component of the kinetic energy $\rho v_\theta^2/2$. The energy starts from zero and grows rapidly after $\tilde{t} = 30$, which is the beginning of the instability stage. The energy reaches a maximum value at $\tilde{t} = 140$. The azimuthal velocity contours on plane $\theta = 0$ and π at $\tilde{t} = 173$, which is at the initial stage of vortex breakdown, is plotted in Figure3.14 (a). The velocity is scaled with $U^* = \Gamma/R$, where Γ is the total circulation after the ring is formed. The contours show opposing streams across the ring core, because angular momentum should be conserved. It also reveals that the azimuthal flow is not limited to the core, but extends into the wake region. Figure 3.14 (b) plots the front view of the azimuthal velocity contour, the axial flow is unevenly distributed in the azimuthal direction, as a result of the uneven breakup of azimuthal wave.

Another effect caused by the three-dimensional vortex ring instability is the growth of streamwise vorticity,

$$\omega_z = \frac{1}{r}\frac{\partial}{\partial r}(rv_\theta) - \frac{1}{r}\frac{\partial v_r}{\partial \theta}. \tag{3.3}$$

The equation shows that the growth of azimuthal velocity will create the streamwise vorticity. The temporal evolution of the streamwise vorticity is shown in Figure 3.15. The

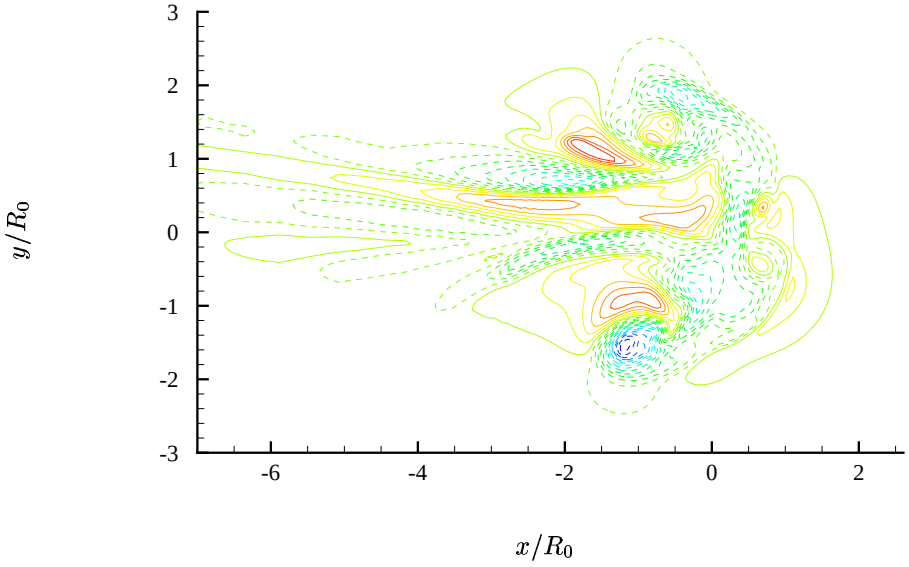

(a)

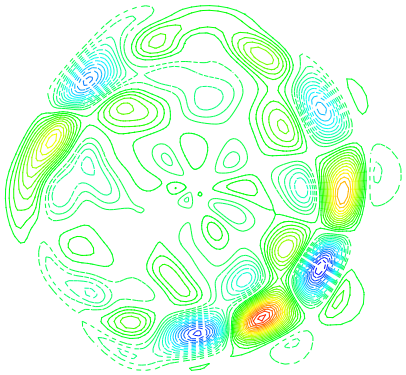

(b)

Figure 3.14: (a) Contour plot of axial velocity v_θ/U^* at $\tilde{t}$ =173. (——), in the direction of mean azimuthal vorticity, (·····), opposite to the mean azimuthal vorticity, min= -0.078, max=0.039, increment=0.0056. (b)Azimuthal distribution of axial velocity, min= -0.033, max=0.033, increment=0.0028.

vorticity grows in time as the azimuthal instability develops. The streamwise filaments are elongated by the high field strain and are pulled outward from the axis of the ring, and then shed into the wake. Periodic shedding of hairpin vortices was observed in previous experiments (Glezer & Coles 1990, Auerbach 1990) and numerical simulations (Shariff et al. 1994) of turbulent vortex ring. Shedding of vorticity reduces the circulation of the vortex ring, and sometime cause the ring to relaminarize (Weigand & Gharib 1994). On the other hand, from Figure 3.11, the azimuthal vorticity is confined in the core region during the transition stage. Figure 3.16 plots the three-dimensional isosurface and contours of streamwise vorticity ω_z in an axial slice of the ring ($\theta = 0$ and π), at $\tilde{t} = 151$. The streamwise vorticity has alternating signs in the radial and azimuthal directions. Near the centerline, filaments are stretched and are pulled outward from the core.

3.5 Mean flow and turbulence statistics

Two types of averages are used to separate turbulent fluctuations from the mean flow. The first is designated with an overbar, e.g., $\bar{f}$, and is a Reynolds average taken over the homogeneous flow direction θ. In case 8, there are 15 realizations with the same flow parameters but different initial perturbations, and the azimuthal averaged quantities are further ensemble averaged to increase the statistical sample size. The ensemble average is denoted with <> and is defined as

$$< \bar{f} >= \frac{1}{N_{\text{ens}}} \sum_{l=1}^{N_{\text{ens}}} \bar{f}_l. \tag{3.4}$$

Averaging the flow equation in this manner generates terms involving density and velocity correlations such as $\overline{\rho' u_x'}$. However, since the maximum Mach number studied is less than 0.3, the maximum density fluctuation $\rho'/\bar{\rho}$ is found to be less than 5 percent. In addition, we do not study the balance of turbulent energy budget; therefore we assume constant density when computing quantities such as Reynolds stresses.

To confirm the convergence of the ensemble average, total circulation in the computational domain is computed for each run, and 4 runs are plotted in Figure 3.2. During the formation and laminar translation stage, there is no dispersion of circulation among the realizations, but as the vortex ring become turbulent, the circulation will vary between

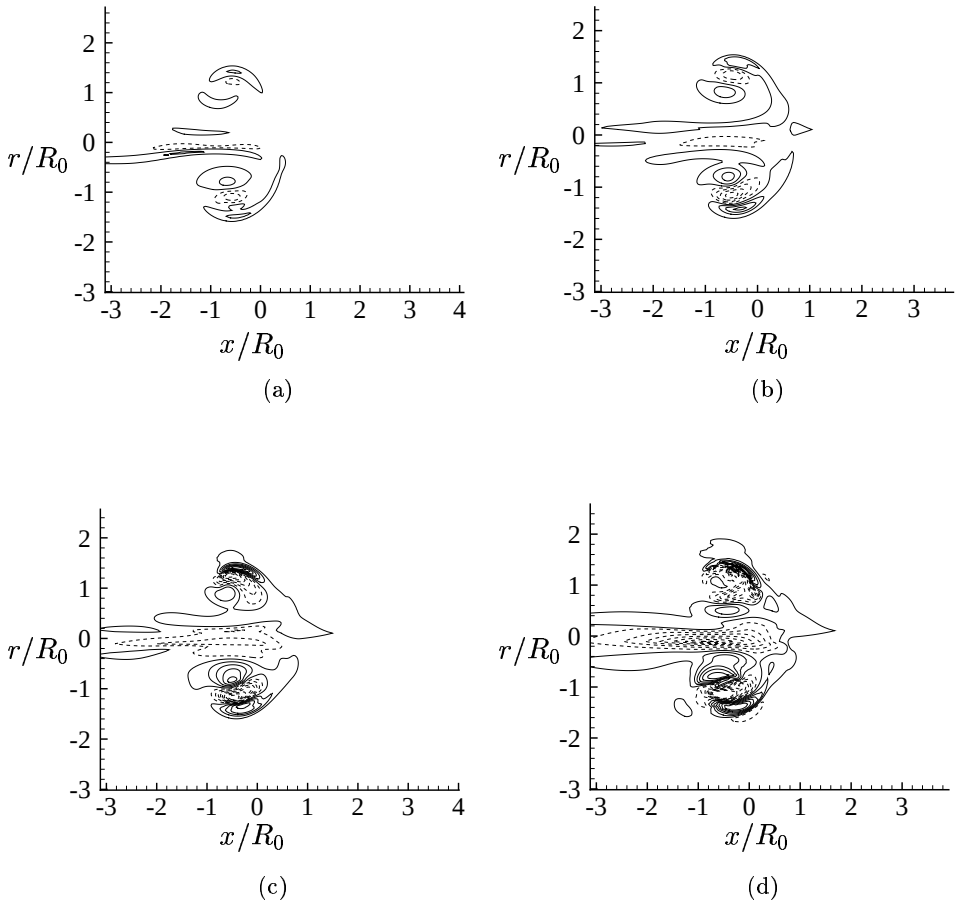

Figure 3.15: Temporal evolution of the streamwise vorticity ω_z. a) $\tilde{t}$ =102; b) $\tilde{t}$ =127; c) $\tilde{t}$ =154; d) $\tilde{t}$ =180. Max.=0.8, min.=-0.8, increment=0.1.

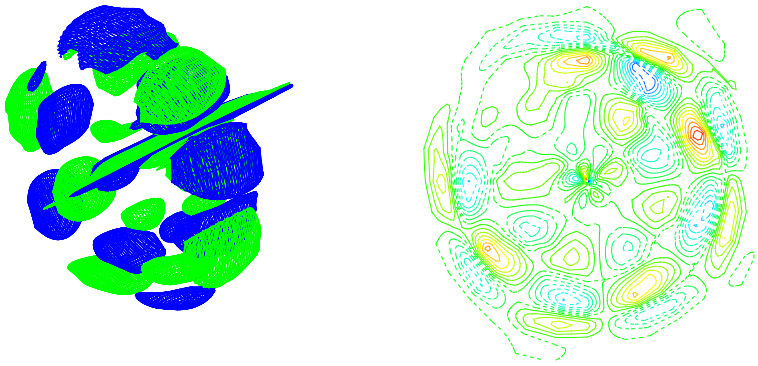

(a) (b)

Figure 3.16: a) Iso-surface of streamwise vorticity ω_z at $\tilde{t} = 180$, level=-0.15, 0.15; b) contours of ω_z in the plane $\theta = 0$ and π, with 20 evenly spaced contours between -0.6 and 0.6. (——) positive, (----) negative.

different realizations due to irregular shedding and cancellation of vorticity. The average of the circulation during turbulent stage is computed with number of ensembles from 1 to 7 and is plotted in Figure 3.17. The circulation is scaled with $\Gamma_{\max}$, the maximum circulation after ring formation. The average circulation converge to the mean sequence with more than 6 realizations. For other quantities such as energy spectrum and Reynolds stresses, more realizations are needed to achieve accurate averages.

Figure 3.18 plots the ensemble-averaged one-dimensional energy spectra in the azimuthal direction. In the initial stage, only wave numbers from 1 to 32 are excited, and higher wave numbers have zero initial energy. During the transition stage the spectra are dominated by the low azimuthal modes, and all the energy components increase rapidly as energy is extracted from the mean flow. At later stage of the instability, higher modes are excited by nonlinear interactions between lower modes, and the spectra broaden as turbulence energy cascade is established. The spectrum achieves a quasi-steady state after $\tilde{t} = 110$. Although the flow is not statistically stationary, the slope of the spectrum is invariant and decays slowly due to turbulent dissipation.

To compute the circulation of the vortex ring alone (i.e without the wake), we set the vorticity to zero outside of a closed iso-contour of vorticity around the leading vortex core, at which point the vorticity is 2 % of the maximum vorticity in the core right after formation.

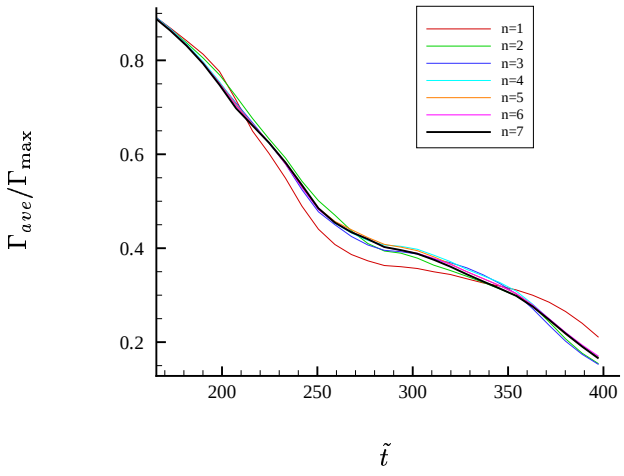

Figure 3.17: Averaged circulations with number of ensembles from 1 to 7.

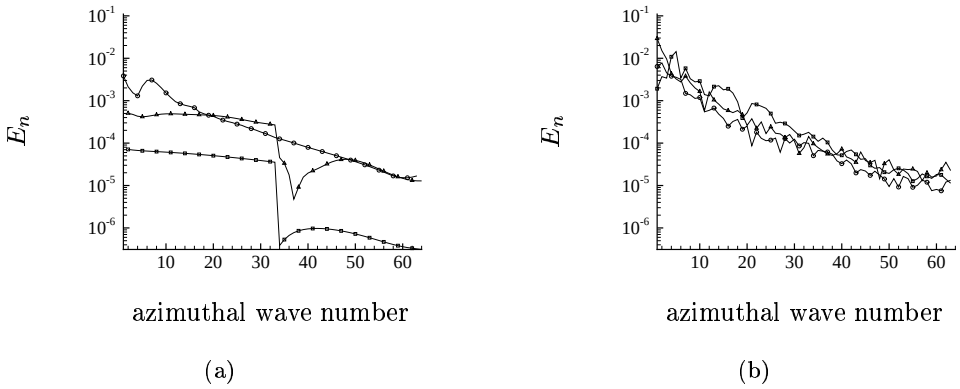

Figure 3.18: One-dimensional energy spectra in θ direction. (a) laminar stage, (□) $\tilde{t} = 8.6$; (△) $\tilde{t} = 43.2$; (o) $\tilde{t} = 86.4$; (b) turbulent stage, (□) $\tilde{t} = 130$; (△) $\tilde{t} = 216$; (o) $\tilde{t} = 302$.

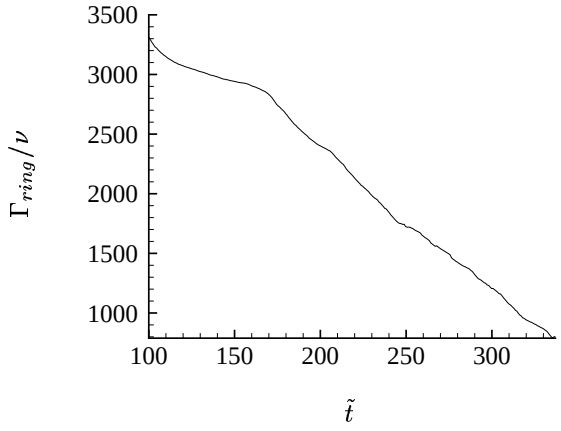

Figure 3.19: Decay of vortex ring Reynolds number Γ_{ring}/ν, one run in case 8.

The circulation within the contour is computed with

$$\Gamma_{ring} = \int \omega dx dr. \tag{3.5}$$

which is integrated numerically with a 4th-order accurate quadrature scheme. Figure 3.19 plots the decay of Reynolds number of the vortex ring Γ_{ring}/ν. Unlike total circulation in Figure 3.2, which decays as $t^{-\frac{1}{2}}$ during the turbulent stage, decay of the vortex ring circulation can be approximated as a linear function of time, similar to the experimental observation of Weigand & Gharib (1994).

Once formed, the vortex ring translates downstream with self-induced velocity. Figure 3.20 (a) plots the ensemble-averaged trajectory of the vortex rings. The vortex ring centroid is calculated with (Saffman 1978)

$$X = \frac{\int \omega x r^2 dx dr}{\int \omega r^2 dx dr}. \tag{3.6}$$

Translational velocity of the vortex ring is depicted in Figure 3.20 (b), and is compared with the velocity of a viscous laminar vortex ring (Saffman 1970) with the same flow parameters, i.e. Reynolds number, circulation, core radius, etc. Unlike the smooth decay of the laminar ring, decay of velocity of the turbulent vortex ring follows a stair-like fashion, similar to that reported by Weigand & Gharib (1994). It is caused by the periodic shedding of vorticity from the vortex ring into the wake. Decay of the translation velocity in the turbulent stage

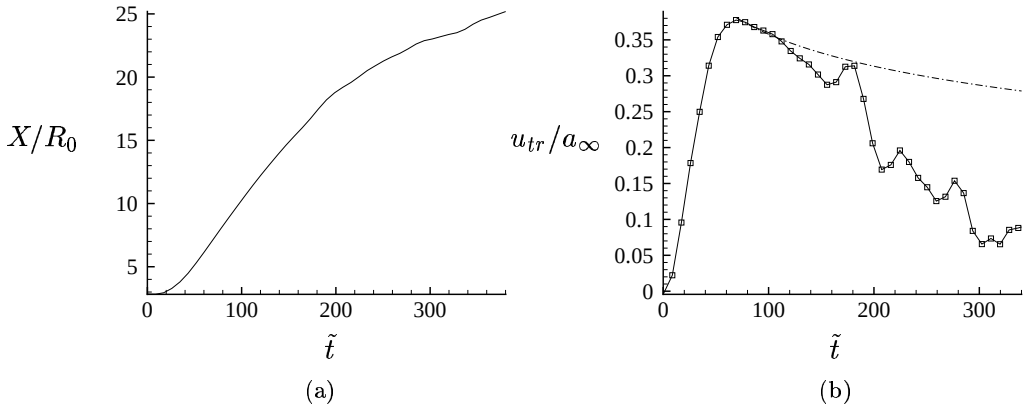

Figure 3.20: (a) Trajectory of the centroid of the vortex ring in case 8, ensemble-averaged with $N = 12$. (b) (□) ensemble-averaged translational velocity of the turbulent vortex ring, (—·—) of a laminar vortex ring with the same ring properties.

is much faster than the laminar vortex ring.

The instability waves extract energy from the mean flow, and feed energy into smaller scales, the energy cascade is established with Reynolds stresses. In Figure 3.21, we plot the radial profile of the ensemble-averaged axial velocity, and two components of Reynolds stresses across the center of the vortex ring, all scaled with $U^* = UR/\Gamma$. Because of the dispersion among trajectories of vortex rings, the centroid of each vortex ring has to be computed individually, and the radial profiles are measured at that location. After the formation of the vortex ring, the peak value of the mean axial flow decreases due to viscous diffusion. The Reynolds stresses are negligible during the linear instability stage. However, during the nonlinear stage, both Reynolds stresses rise rapidly and reach maximum values at $\tilde{t} = 173$, suggesting the end of turbulence transition. The saturation value for the component $< \overline{u'_x u'_x} >$ is $0.047 U_j^2$, which is about same value with the numerical simulation of a turbulent jet with similar Reynolds number (Freund 2001). Glezer & Coles (1990) measured the distribution of Reynolds stresses $< \overline{u'_x u'_x} >$, $< \overline{u'_r u'_r} >$ and $< \overline{u'_x u'_r} >$, as well as the turbulence production terms. However, the azimuthal Reynolds stress $< \overline{u'_\theta u'_\theta} >$ was not measured, therefore the turbulence production terms are incomplete. They estimated the upper bound of the term to be the sum of the other two Reynolds normal stresses. In the present study, we use as many as 15 runs to obtain ensemble-averaged mean velocity and all

major components of Reynolds stresses, which are plotted in Figure 3.22 to 3.26. The radial and azimuthal components of the Reynolds stresses have about the same amplitude, and the axial component is about twice of the amplitude. The amplitude of the shearing stress $< \overline{u'_x u'_r} >$ is about 50 percent of the normal stress. We observe that both the radial and azimuthal normal stresses have a wake region, which confirm the existence of streamwise vorticity discussed in the previous section.

To investigate how turbulence is produced by the vortex ring. We compute the incompressible turbulent kinetic energy balance

$$< \frac{dk}{dt} >=< P > + < T > - < \epsilon >, \tag{3.7}$$

where

$$< k >=< \frac{1}{2}\overline{u'_i u'_i} > \tag{3.8}$$

is the total turbulence energy, and

$$< P > = < \boldsymbol{\tau} \cdot \nabla \boldsymbol{U} >=< -\overline{u'_x u'_x}\frac{\partial \overline{u}_x}{\partial x} > - < \overline{u'_x u'_r}\left(\frac{\partial \overline{u}_x}{\partial r} + \frac{\partial \overline{u}_r}{\partial x}\right) > \tag{3.9}$$

$$- < \overline{u'_r u'_r}\frac{\partial \overline{u}_r}{\partial r} > - < \overline{u'_\theta u'_\theta}\frac{\overline{u}_r}{r} >, \tag{3.10}$$

is the turbulence production term,

$$< T >=< \nabla \left(\overline{\boldsymbol{u}} \cdot (\frac{1}{2}\overline{u'_i u'_i} + \frac{p'}{\rho}) \right) > \tag{3.11}$$

is mean flow transport term, and

$$< \epsilon >=< \nu \overline{S'_{ij} S'_{ij}} > \tag{3.12}$$

is viscous dissipation. We concentrate on the turbulent production terms. Eq. 3.9 differs from the corresponding equation for plane flow only in the last term. The term u_r/r represents stretching or contracting of circular vortex lines due to mean radial motion, and $\overline{u'_\theta u'_\theta}$ represents the contribution from the azimuthal flow studied in the previous section.

Figure 3.27 plot the distribution of the 4 terms of P at $\tilde{t} = 173$, when the Reynolds stresses reach the maximum value, and Figure 3.28 plot the sum P. At this moment, the

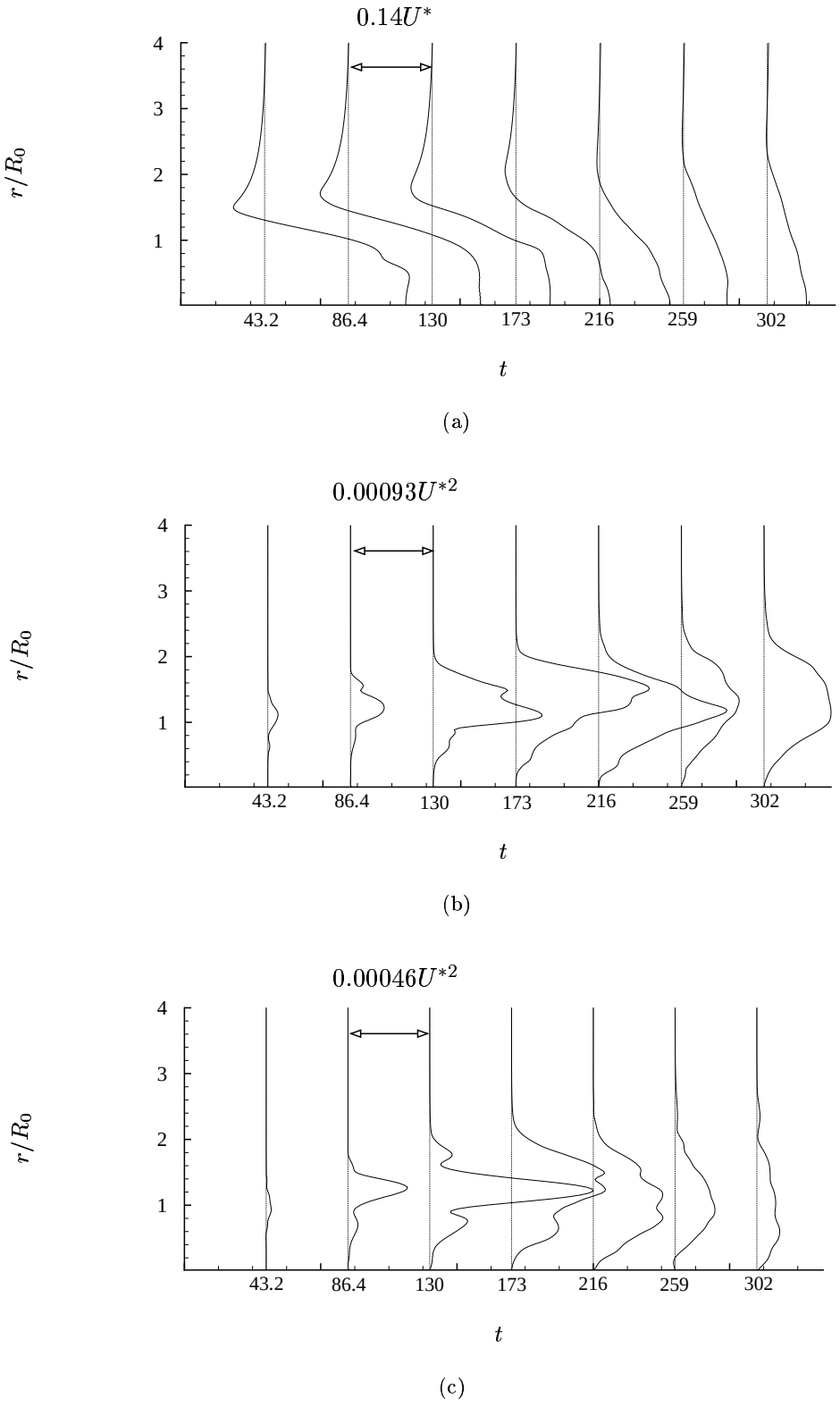

Figure 3.21: (a) Radial distribution of ensemble-averaged axial velocity $< \overline{u}_x/U^* >$ at $\tilde{t} =$ 43.2, 86.4, 130, 173, 216, 259, 302. (b) Reynolds stress component $< \overline{u'_x u'_x}/U^{*2} >$, (c) Reynolds stress component $< \overline{u'_x u'_r}/U^{*2} >$.

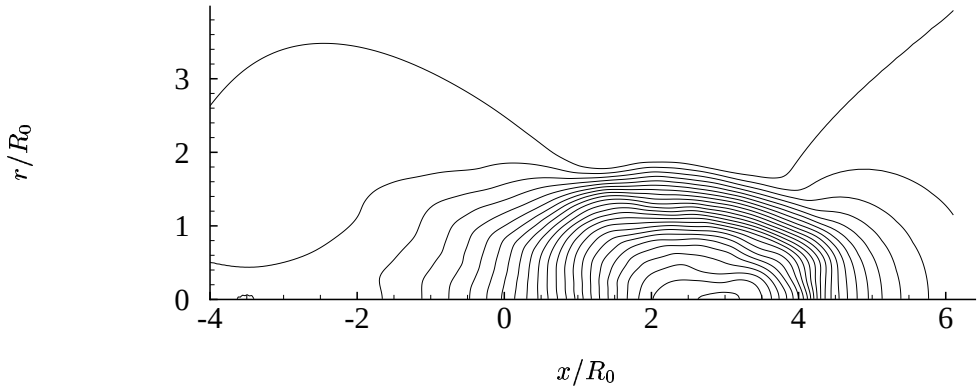

(a)

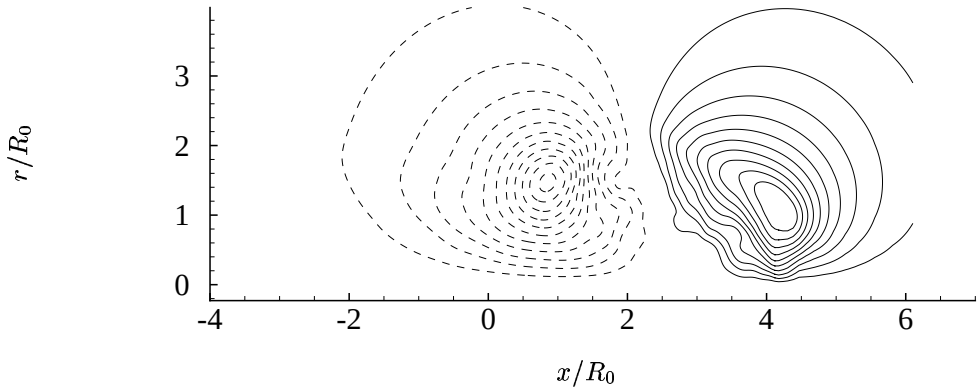

(b)

Figure 3.22: (a) Contour plot of ensemble-averaged axial velocity $\overline{u_x}/U^*$ ($N = 15$, case 8), min.=0.0056, max.=0.13, increment=0.0056; (b) ensemble-averaged radial velocity $\overline{u_r}/U^*$, min.=-0.03, max.=0.03, increment=0.0028.

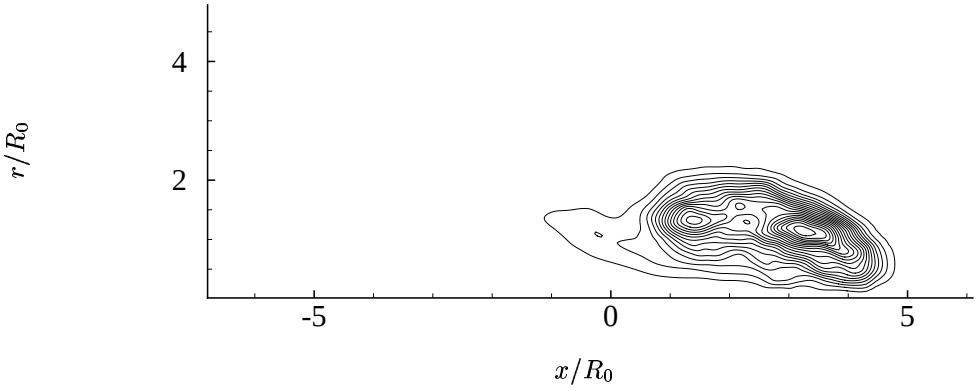

Figure 3.23: Contour plot of ensemble-averaged Reynolds stress $< \overline{u'_x u'_x}/U^{*2} >$, min.=$7.7 \times 10^{-5}$, max.=$1.5 \times 10^{-3}$, increment=$7.7 \times 10^{-5}$.

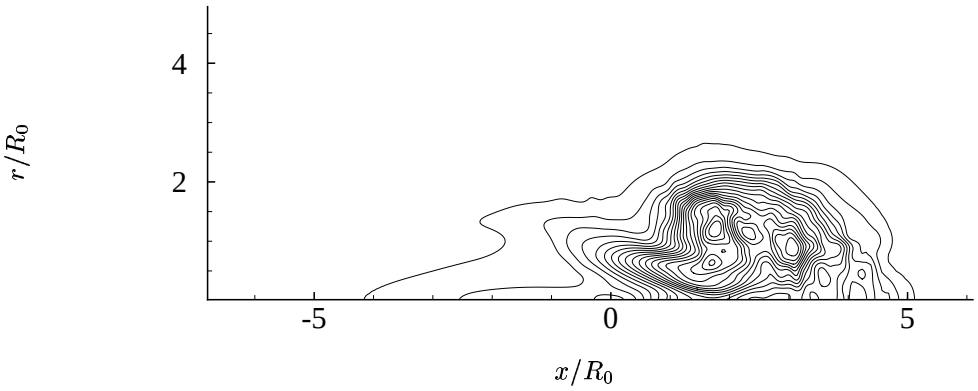

Figure 3.24: Contour plot of ensemble-averaged Reynolds stress $< \overline{u'_r u'_r}/U^{*2} >$, min.=$3.9 \times 10^{-5}$, max.=$7.7 \times 10^{-4}$, increment=$3.9 \times 10^{-5}$.

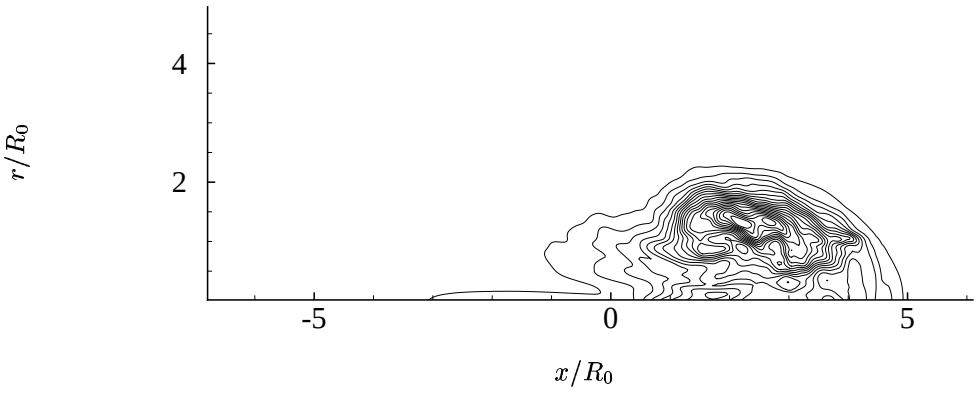

Figure 3.25: Contour plot of ensemble-averaged Reynolds stress $< \overline{u'_\theta u'_\theta}/U^{*2} >$, min.=$3.9 \times 10^{-5}$, max.=$9.3 \times 10^{-4}$, increment=$3.9 \times 10^{-5}$.

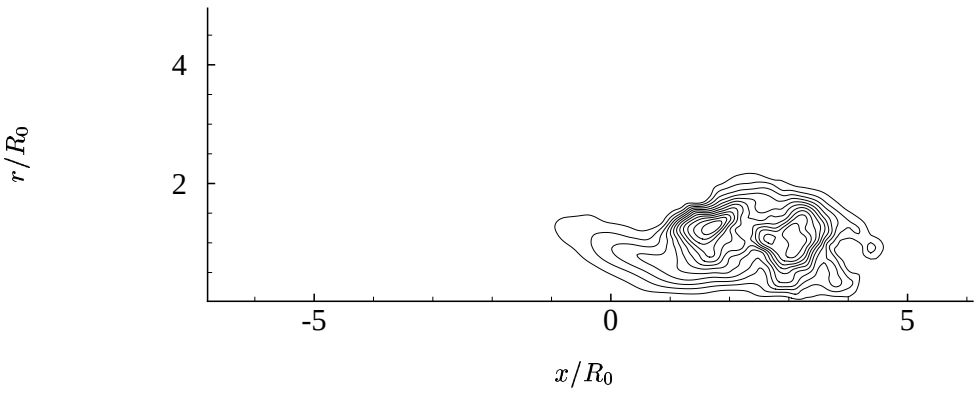

Figure 3.26: Contour plot of ensemble-averaged Reynolds stress $\overline{<}u'_x u'_r/U^{*2} >$, min.=$3.9 \times 10^{-5}$, max.=$4.6 \times 10^{-4}$, increment=$3.9 \times 10^{-5}$.

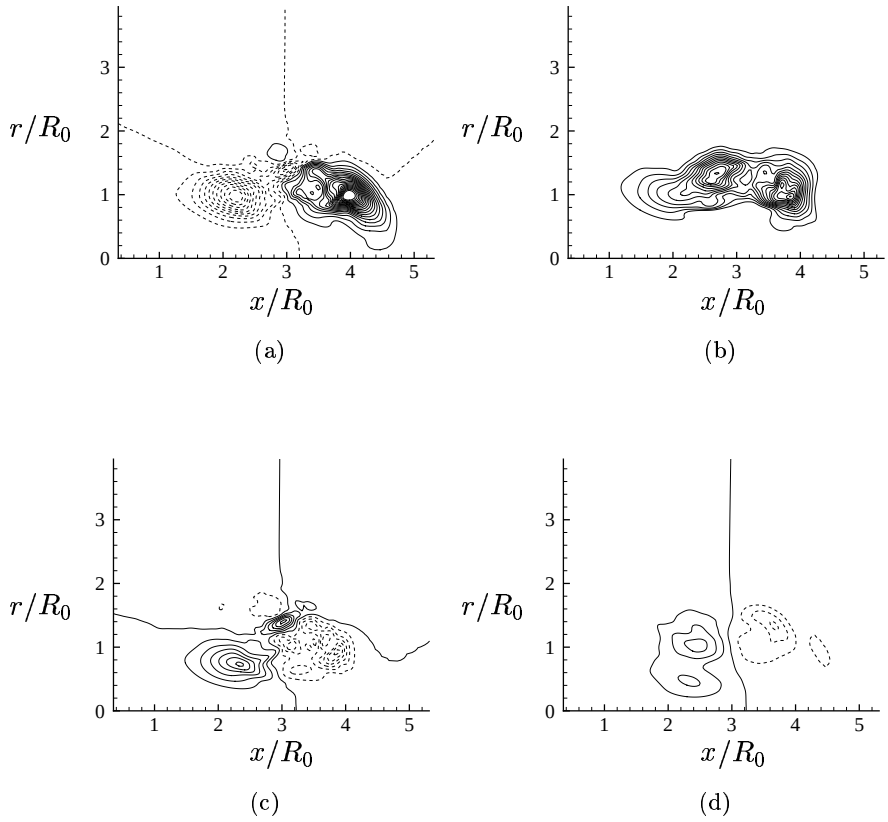

Figure 3.27: Contour plot of turbulence production terms, scaled with U^{*3}/R_0, (a) $< -\overline{u'_x u'_x}\frac{\partial \overline{u}_x}{\partial x} >$, min.$=-1\times10^{-4}$, max.$=1.8\times10^{-4}$, increment$=1\times10^{-5}$; (b) $< -\overline{u'_x u'_r}(\frac{\partial \overline{u}_x}{\partial r} + \frac{\partial \overline{u}_r}{\partial x}) >$, min.$=1\times10^{-5}$, max.$=1.4\times10^{-4}$, increment$=1\times10^{-5}$; (c) $< -\overline{u'_r u'_r}\frac{\partial \overline{u}_r}{\partial r} >$, min.$=-6\times10^{-5}$, max.$=6\times10^{-5}$, increment$=1\times10^{-5}$; (d) $< -\overline{u'_\theta u'_\theta}\frac{\overline{u}_r}{r} >$, min.$=-3\times10^{-5}$, max.$=3\times10^{-5}$, increment$=1\times10^{-5}$.

turbulent production is positive within the entire vortex ring core, and is stronger at the front half of the core. The major contribution to turbulent production is from the first two terms, and both terms are positive at the front of the core. Glezer & Coles (1990) suggested that the higher turbulent production at this region is due to vortex stretching. However, the last term in Eq. 3.9 is negative in the front region in the simulations. Another difference between simulation and the experiment is with the term $< -\overline{u'_r u'_r}\frac{\partial \overline{u}_r}{\partial r} >$. This term is dominant in the experiment because of the large radial velocity gradient across the thin core. With a thicker core in the simulation, this term has smaller contribution to the turbulent production.

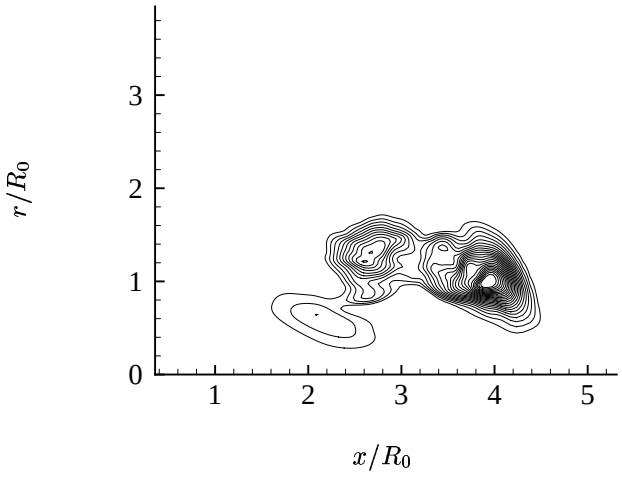

Figure 3.28: Contour plot of total turbulence production, scaled with U^{*3}/R_0, min.=2×10^{-5}, max.=2.4×10^{-4}, increment=1×10^{-5}.

3.6 Self-similar decay of vortex ring

During the turbulent stage, mean flow properties such as peak axial velocity, peak vorticity, vortex ring circulation decay in time, whereas the core radius and ring radius increase in time, both due to turbulent diffusion and entrainment of surrounding irrotational fluid. Maxworthy (1977) studied the decay of the vorticity inside the core. He separated the flow field into three distinct regions, ambient, outer flow and core region, with well-defined interface between them. He found that the ring growth rate was controlled by entrainment across the core/outerflow interface. The core fed the outer flow with vorticity, mainly through diffusion, and vorticity was mixed with irrotational fluid by turbulent fluctuations in the outer flow region. In the current study, Reynolds number is lower than in the experiments, and the core region is not well separated from the outer flow. This leads to higher vorticity diffusion and decay rate.

In a fully turbulent vortex ring, the evolution of statistical quantities will be independent of the kinematic viscosity and depend only on linear impulse I/ρ, where I is computed from the time integral of the forcing function. Then from dimensional analysis we can define a

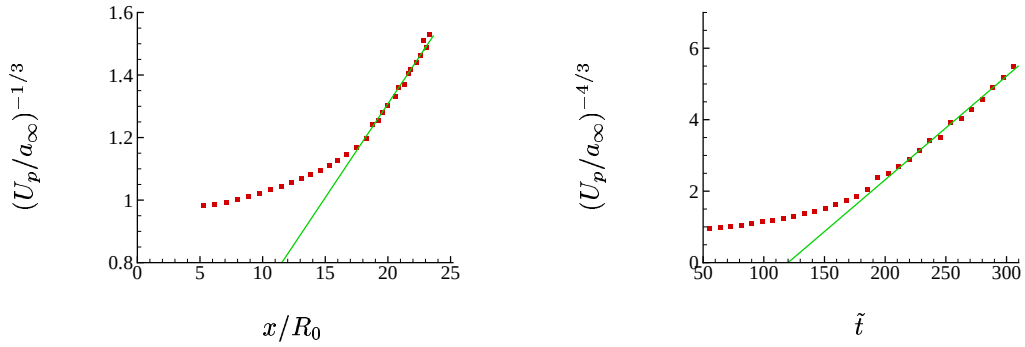

Figure 3.29: a) Peak axial velocity along the centerline vs. axial location, b) peak axial velocity along the centerline vs. time.

new velocity scale, u_s, and coordinates ξ and η with (Glezer & Coles 1990),

$$u_s = (I/\rho)^{\frac{1}{4}}(\tilde{t} - \tilde{t}_0)^{-\frac{3}{4}}, \tag{3.13}$$

$$\xi = (x - x_0)\left(\frac{\rho}{I(\tilde{t} - \tilde{t}_0)}\right)^{\frac{1}{4}}, \tag{3.14}$$

$$\eta = r\left(\frac{\rho}{I(\tilde{t} - \tilde{t}_0)}\right)^{\frac{1}{4}}, \tag{3.15}$$

which gives a power law,

$$u_p^{-\frac{1}{3}} \sim (\tilde{t} - \tilde{t}_0)^{\frac{1}{4}} \sim (x - x_0), \tag{3.16}$$

where x_0 and $\tilde{t}_0$ are virtual origins of the turbulent vortex rings.

The decay of peak axial velocity on the centerline u_p along the vortex ring trajectory, and against time, is plotted in Figure 3.29 (a) and (b), respectively. The figures demonstrate that during turbulent stage, the evolution of vortex ring approximately follow Eq. 3.16.

With least square fitting of Eq. (3.16), the virtual origins are found to be $\tilde{t}_0 = 130.0$, $x_0 = 0.064$. The virtual origin of time shows a large positive value, which is different than the experiments of Glezer & Coles (1990), where both x_0 and t_0 are negative, i.e, the origin in x is upstream of the orifice where the ring is generated, and the origin in time is earlier than the beginning of vortex ring formation. The difference is caused by the core thickness. For a thicker core (turbulent puff), the ring has larger growth rate and both origins tend to

be positive (Johnson 1970, Kovasznay, Fujita & Lee 1973); whereas for a thin cored vortex ring, the opposite is usually true (Turner 1957).To test the self-similarity, we plot velocity profiles in both original (x, r) and scaled coordinates (ξ, η) in Figure 3.30. We can compare Figure 3.30 (b) with Figure 6 in Glezer & Coles (1990). With a larger sample size, the ensemble averaged mean velocity profiles in the experiment are smoother. In addition, with higher Reynolds number, the collapse between the profiles are better then the low Reynolds number simulation. The different values of virtual origins lead to the different value of η and ξ. In the experiments, $x - x_0$ is larger due to the negative value of x_0, therefore η is larger than in the simulations. On the other hand, $(\rho/I(\tilde{t} - \tilde{t}_0))^{\frac{1}{4}}$ is smaller due to the negative value of $\tilde{t}_0$, therefore the variation of η in the vortex ring region is smaller than the simulations. Nevertheless, both axial profile and radial profile of velocity from simulation show good collapse in the similarity coordinate system. The plots show that self-similar decay is achieved for $\tilde{t} > 173$. the Self-similarity of the sound field will be studied in the next chapter.

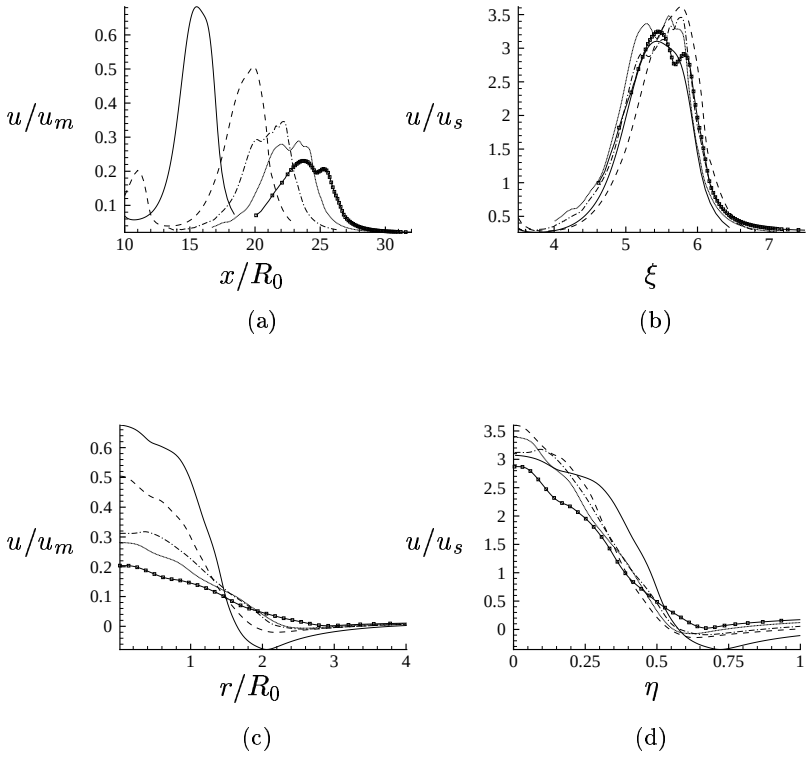

Figure 3.30: Centerline mean axial velocity. (a), in origin variables, scaled with the maximum axial velocity just after ring formation, u_m; (b) in similarity variables. Radial profile of mean axial velocity across the center of the vortex ring (c) in origin variables, scaled with u_m; (d) in similarity variables. (——) $\tilde{t} = 173$ (- - - -) $\tilde{t} = 216$, (—·—) $\tilde{t} = 259$, (·····) $\tilde{t} = 302$, (□) $\tilde{t} = 346$.

Chapter 4

Sound Field of a Turbulent Vortex Ring

In this chapter, we study the sound generation by a turbulent vortex through DNS. The simulated sound field is compared with experiments and theories, to help understand the sound generation process and evaluate different theories discussed in section 1.5.

4.1 The acoustic field

Figure 4.1 shows the acoustic field, measured with pressure perturbation p', in the far field. Recall that the far-field is computed by the Kirchhoff method described in Section(2.3). At $\tilde{t} = 138$, a large pressure pulse is generated by the vortex ring formation, and propagates out of the domain. After $\tilde{t} = 225$, sound with higher frequency is generated by the vortex ring instability, and the sound generation continues until the vortex ring become fully turbulent. The acoustic field is stronger in the downstream direction.

The acoustic field is measured around a circle at $|x| = 16.1R$, $\chi = 52^\circ$ for a particular realization of case 8. The initial pulse produced by the forcing is the same among all the realizations and can be removed by the ensemble average,

$$p' = p - < \bar{p} > \tag{4.1}$$

The acoustic field is then decomposed into azimuthal modes $n = 0$, 1, 2, 3 (Figure 4.2). The sound pressure level begins to grow during the linear stage, and peaks when the instability becomes nonlinear and the vortex ring starts to breakdown. The pressure signals have a distinct frequency at this stage. As the vortex ring transitions and vorticity begins to decay,

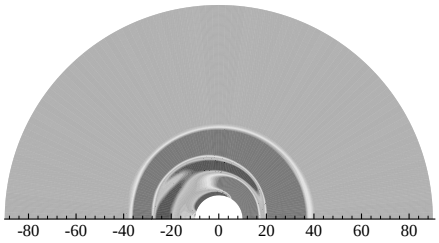

(a)

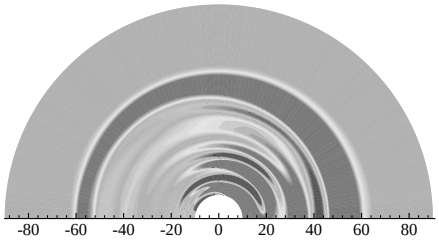

(b)

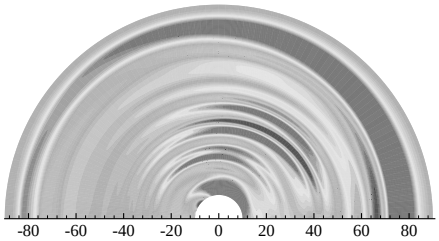

(c)

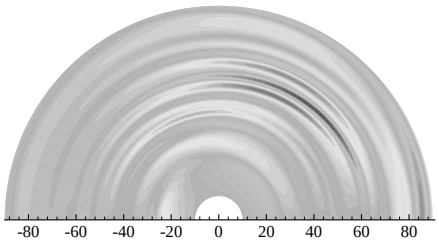

(d)

Figure 4.1: Contour plot of pressure $p'/\rho a_\infty^2$ at the far field, $|x|$ from $10R_0$ to $90R_0$, $\tilde{t} =$, a) 138, b) 225, c) 311, d) 380, with 20 levels evenly spaced between -1.5×10^{-6} and 1.5×10^{-6}.

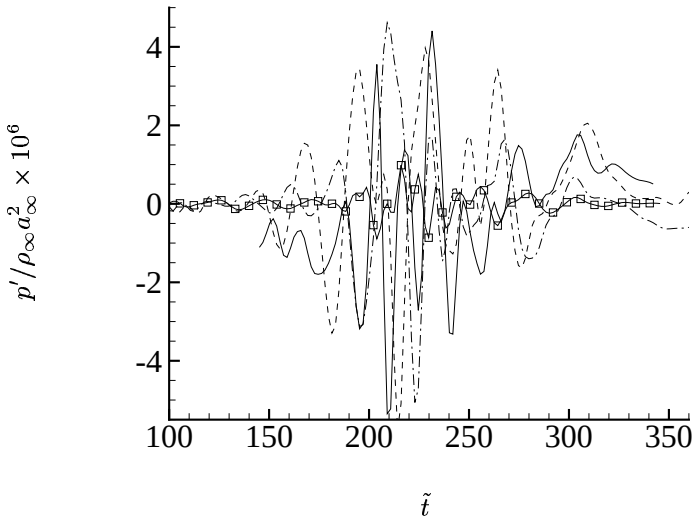

Figure 4.2: Azimuthal components of acoustic field at $|x| = 16.1R$, $\chi = 52°$, (——) $n = 0$, (----) $n = 1$, (—·—) $n = 2$, (□) $n = 3$, one realization in case 8.

both the amplitude and the frequency of the pressure disturbance decreases as well. The drift of the peak frequency to lower frequency is also detected in the experiments (Zaitsev et al. 1990). It is also found that at this location, the amplitudes of the first 3 azimuthal modes are roughly equal, whereas the peak amplitude of the $n = 3$ mode is less than 20 percent of the first 3 azimuthal modes. The $n = 1$ mode of the acoustic fields for three realizations of case 8 is plotted in Figure 4.3, and compared with case 10, which has a longer domain and enables acoustic measurement for longer time before the vortex ring interact with the boundary. It is observed that the phases of pressure disturbances have higher correlation during the laminar stage, and are less correlated after the turbulent transition. The sound pressure level decays rapidly after $\tilde{t} = 300$, and the vortex ring stops radiating sound after $\tilde{t} = 400$, suggesting that the core oscillations are suppressed.

4.2 Sound pressure level and spectrum

The sound pressure level (SPL) , which is defined as

$$\mathrm{SPL} = 20\log_{10}\left(\frac{\mathrm{p}'_{\mathrm{rms}}}{2 \times 10^{-5}}\right) \tag{4.2}$$

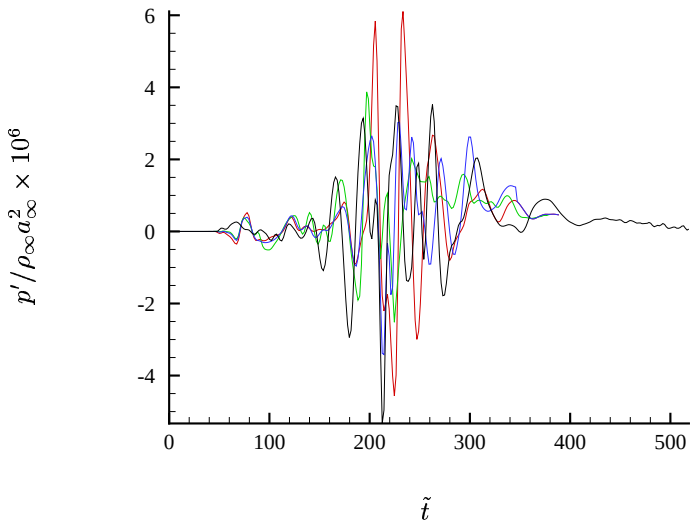

Figure 4.3: Azimuthal components $n = 1$ of the acoustic field at $|x| = 16.1R$, $\chi = 52°$, 3 realizations of case 8 (red, green, and blue lines) and 1 realization of case 10 (black line).

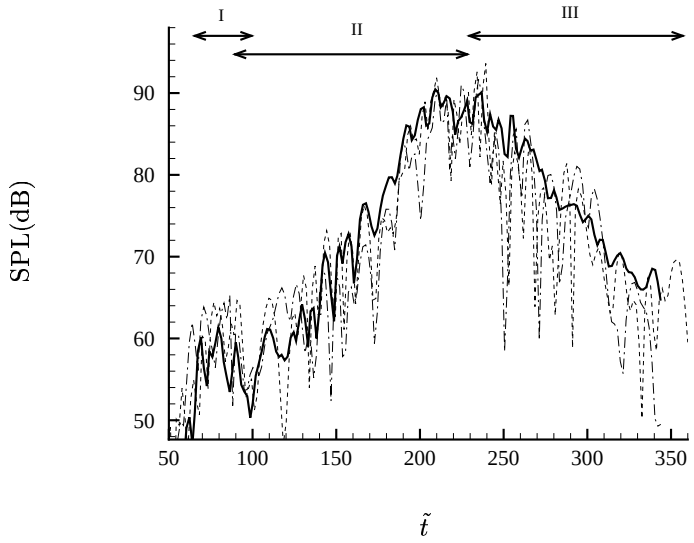

Figure 4.4: Sound pressure level measured at point $\chi = 52°$, $16.1R_0$, (——) ensemble averaged ($N = 12$); (—·—) realization 1; (----) realization 2.

is measured and ensemble averaged at $\chi = 52°$, $16.1R_0$ in case 8. This position corresponds to an acoustic delay of $\tilde{t} = 58.0$ from the nominal ring position. The averaged SPL and SPL from 2 realizations are plotted against time in Figure 4.4. For comparison with Figure 3.2, stages I, II and III of the circulation evolution is marked. The sound generation also consists of three stages, which are related to the dynamics of the vortex ring. Before $\tilde{t} = 200$, instability waves generate relatively weak sound, and the growth of the sound pressure level is related to the growth rate of the corresponding vortex ring instability modes. From $\tilde{t} = 200$ to 260 vortex breakdown occurs, and the sound pressure level is maximum. From $\tilde{t} = 260$ to 300, the turbulent decay of the ring leads to a decay in SPL by 30 dB.

The spectrum at four different polar angles for azimuthal mode $n = 0$, 1, 2 and the total is measured and plotted in Figure 4.5. Because the computational domain move with the vortex ring, there is no Doppler shift between different angles. In the laboratory, there would be a Doppler shift, but since we wish to compare to the very low Mach numbers ($M = 0.08$) experiments of Zaitsev et al. (1990), we made no Doppler correction here. The frequency is scaled with $f^* = \Omega_0/4\pi$, where Ω_0 is the equivalent vorticity if vorticity were uniformly distributed inside the core. For a laminar vortex ring, the equivalent vorticity can be calculated with the vortex ring translational velocity U_{tr} and μ, which is the ratio of core radius to ring radius, and the ring radius R. Although the vortex ring transitions to turbulence, its sound radiation peaks at the late stage of laminar ring, therefore we use formulas for laminar vortex ring to find the equivalent Ω. A laminar vortex ring with circulation Γ, ring radius R and core radius σ will translate with velocity (Kelvin 1867*b*)

$$U_{tr} = \frac{\Gamma}{4\pi R}\left[\log\frac{8R}{\sigma} - \frac{1}{4}\right], \tag{4.3}$$

with uniform vorticity Ω_0, the total circulation is

$$\Gamma = \int \Omega_0 dx dr = \pi\sigma^2\Omega_0, \tag{4.4}$$

finally

$$\Omega_0 = 4U_{tr}/\mu^2 RC(\mu), \tag{4.5}$$

where $C(\mu) = \log(8/\mu) - \frac{1}{4}$, and $\mu = \sigma/R$.

The peak of the spectrum is found to be close to 1.0, the value predicted by the model of

Kopiev & Chernyshev (1997), and the aforementioned experimental results. The spectrum is also narrow banded, but the band width is about 2 to 3 times larger than the experiments. A possible explanation can be obtained from the inviscid model (Kopiev & Chernyshev 1997). The bandwidth of the peak $\Delta f/f$ is proportional to the core to ring ratio μ, and the vortex rings in the simulation have $\mu = 0.34$, whereas μ =0.12 in the experiments. In addition, when the sound pressure level is scaled with $\rho M^4 R/|x|$, it also agrees well with experiment ($M \approx 0.074$). Another observation is that at different polar angles, each mode has different relative strength. For example, at shallow angles to the vortex ring axis, the axisymmetric mode dominants; at higher angles, modes $n = 1$ and 2 become relatively stronger, with mode $n = 1$ becoming dominant at $\chi = 55.9°$. The measured directivity of the total sound field is the sum of contributions from each azimuthal modes, and is more monotonic than the individual components. Like the sound field of an unforced jet, there is no angle of extinction. This is a major difference between the sound field of a turbulent vortex ring and an axisymmetric vortex ring, or with axisymmetric interactions such as vortex ring pairing (Bridges & Hussain 1992).

4.3 Comparison with vortex sound theory

From the vortex sound theory(Möhring 1978), the far-field sound generated by a compact vorticity field in a low-Mach number flow is

$$p'(\boldsymbol{x}, t) = \frac{\rho_0}{12\pi c_0^2} \frac{x_i x_j}{|x|^3} \frac{d^3}{dt^3} Q_{ij}(t - |x|/c_0), \tag{4.6}$$

where Q_{ij} is given by the second-order moments of vorticity

$$Q_{ij}(t) = \int (\boldsymbol{y} \times \boldsymbol{\omega}(\boldsymbol{y}, t))_i y_j dv. \tag{4.7}$$

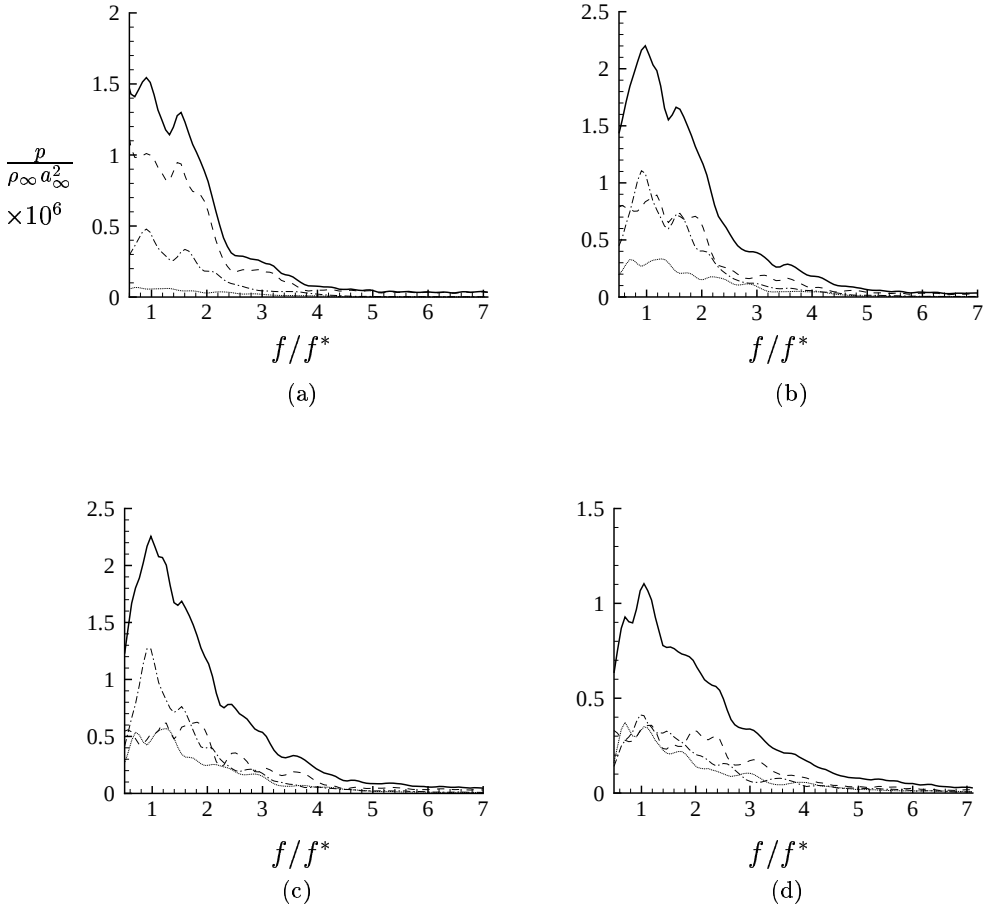

Figure 4.5: Spectrum of different azimuthal modes at different polar angles, $|x| = 15R$. a) $\chi = 18.6°$; b) $\chi = 37.2°$; c) $\chi = 55.9°$; d) $\chi = 93.1°$.(——) total spectrum; (----) $n = 0$; (—·—) $n = 1$, (·····) $n = 2$.

Transforming the coordinate system from (r, θ, z) to (x, y, z), we obtain

$$Q_{11} = -\int rz\omega\cos^2\theta \text{ dv} \qquad Q_{22} = -\int rz\omega\sin^2\theta \text{ dv} \quad Q_{33} = -\int rz\omega \, dv$$
$$Q_{12} = -\frac{1}{2}\int rz\omega\sin 2\theta \text{ dv} \qquad Q_{13} = -\int z^2\omega\cos\theta \text{ dv} \quad Q_{21} = -\frac{1}{2}\int rz\omega sin2\theta \, dv$$
$$Q_{23} = -\int z^2\omega\sin\theta \text{ dv} \qquad Q_{31} = \int r^2\omega\cos\theta \text{ dv} \qquad Q_{32} = \int r^2\omega sin\theta \, dv$$

.....

where

$$\int dv = \int_0^{2\pi} d\theta \int dx \int r dr$$

To a first approximation, we only examine the vorticity component ω_θ, and neglect ω_r and ω_z, which is a good approximation when the flow is nearly axisymmetric. We can then decompose the vorticity field into azimuthal Fourier modes

$$\omega(r, \theta, z, t) = \sum_{k=-n}^{n} \omega_k(x, r, t) e^{ik\theta}. \tag{4.8}$$

It is found that all the moments with $n > 2$ are zero. Plugging Eq. (4.8) into Eq. (4.6), we obtain

$$p_0(|x|, \chi) = \frac{\rho_0}{12c_0^2}\frac{1}{|x|}\frac{d^3Q_0}{dt^3}(3\cos^2\chi - 1), \tag{4.9}$$

$$p_1(|x|, \chi, \theta) = \frac{\rho_0}{24c_0^2}\frac{1}{|x|}\frac{d^3Q_1}{dt^3}\sin 2\chi\cos(\theta - \tilde{\theta}_1), \tag{4.10}$$

$$p_2(|x|, \chi, \theta) = \frac{\rho_0}{24c_0^2}\frac{1}{|x|}\frac{d^3Q_2}{dt^3}\sin^2\chi\cos 2(\theta - \tilde{\theta}_2), \tag{4.11}$$

for modes $n = 0$, 1 and 2, respectively, where

$$Q_0 = \int r^2 z\omega_0 \, dzdr, \qquad Q_1 = \int (rz^2 + r^3)\omega_1 \, dzdr, \qquad Q_2 = \int r^2 z\omega_2 \, dzdr. \tag{4.12}$$

At finite translational Mach number, corrections to these formulas should be made, as the pressure perturbation is intensified in the downstream direction. When we model the vortex ring as a simple quadrupole source convected with constant Mach number, M, the

pressure perturbation will change by the factor $(1 - M\cos\chi)^{-3}$.

Figure 4.6 (a) shows the polar distribution of sound pressure level associated with the total sound field, as well as contribution from azimuthal modes $n = 0$, 1, and 2. Also plotted as comparison is the convection amplification factor $p' \sim (1 - M\cos\chi)^{-3}$. When the convection term is suppressed from the sound pressure level, the directivity of each modes is closer to that predicted with Eq. (4.9), (4.10) and (4.11) . The directivity for the first 3 azimuthal modes, and for two vortex ring Mach numbers M=0.14 and 0.28, are depicted in Figure 4.6 (b) to (d), and are also compared with the theory. The pressure perturbation is scaled with $\rho_0 M^4 R/|x|(1 - M\cos\chi)^{-3}$, and the directivity from theory is plotted at arbitrary amplitude. The agreement between the simulation results and the simplified model is good. The deviation is likely due to the non-compactness of the acoustic source, and non-azimuthal components of the vorticity field. At $n = 2$, the contribution from the other two components of vorticity ω_z and ω_r become comparable with azimuthal component ω_θ, therefore the deviation is larger.

4.4 Vortex core oscillation

In section (4.2) we found a distinct peak frequency around $f/f^* = 1.0$. From the vortex sound theory, this peak frequency must be related to the vorticity oscillation inside the core. On the other hand, Eq. (4.9) to (4.11) relate the far field pressure fluctuations to the third order time derivative of moments of vorticity. To explore this connection, we compute terms d^3Q_0/dt^3, d^3Q_1/dt^3 and d^3Q_2/dt^3, and compute the far field pressure perturbation with Eq. (4.9) to (4.11). The predicted pressure field is compared with the DNS result in Figure 4.7 (a), (b) and (c) for mode $n = 0$, 1, 2, respectively. The result shows good agreement between the DNS result and prediction with vortex sound theory at earlier time. The deviation becomes larger after turbulent transition, again due to the increase of vorticity component ω_r and ω_z.

Among studies of unsteady motions of vortex ring core, Moore (1980) studied the velocity of a vortex ring with elliptic cross section and uniform vorticity Ω. When the core radius is much smaller than the ring radius, the core motion is, to leading order, locally two-dimensional Kirchhoff vortex in a plane normal to the ring axis. The boundary of the

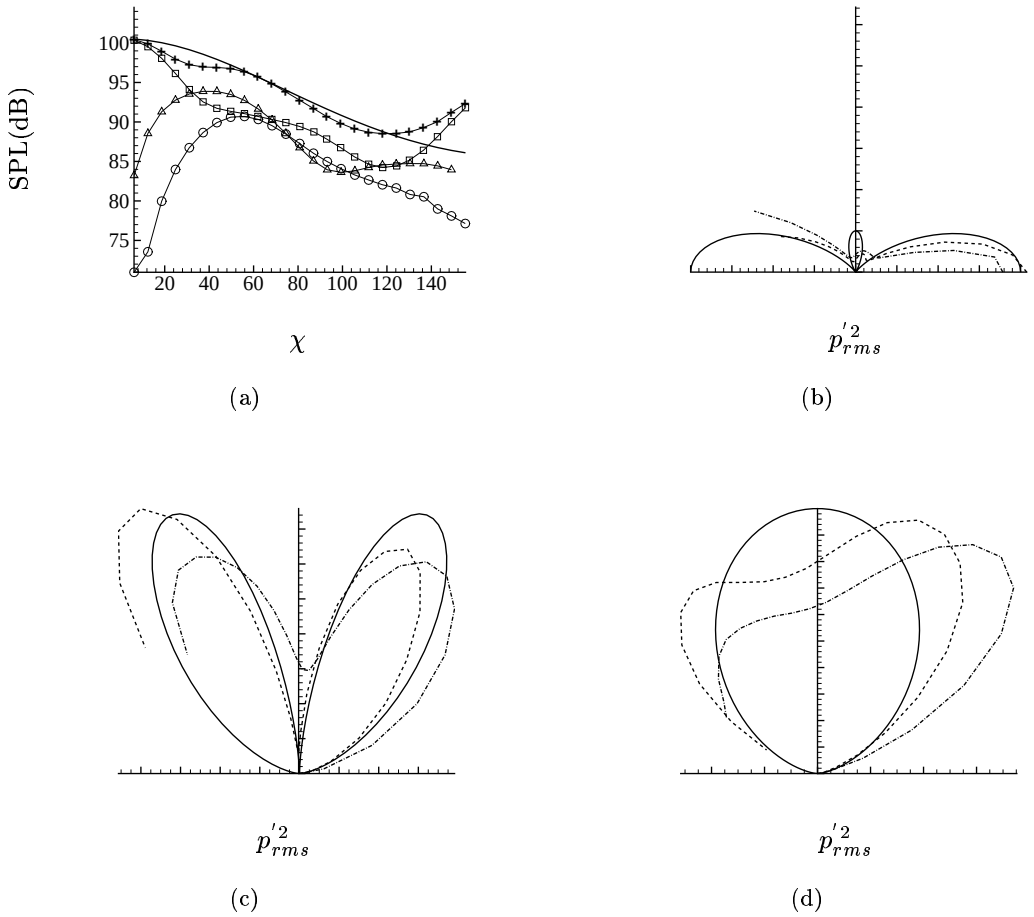

Figure 4.6: (a) Polar distribution of sound pressure level for M=0.28 in dB. (——) $(1 - \mathrm{M}\cos\chi)^{-3}$. (+) total pressure disturbance; (□) $n = 0$; (△) $n = 1$; (o) $n = 2$. (b) to (d), Polar plot of p^2_{rms}. (b) mode $n = 0$, (——) $(3\cos^2\chi - 1)^2$, (- - - -) $M = 0.14$, (—·—) M=0.28; (c) mode $n = 1$, (——) $\sin^2 2\chi$, (- - - -) $M = 0.14$, (—·—) M=0.28; (d) mode $n = 2$, (——) $\sin^4\chi$, (- - - -) $M = 0.14$, (—·—) M=0.28. Note that the theoretical directivities are plotted with an arbitrary overall amplitude.

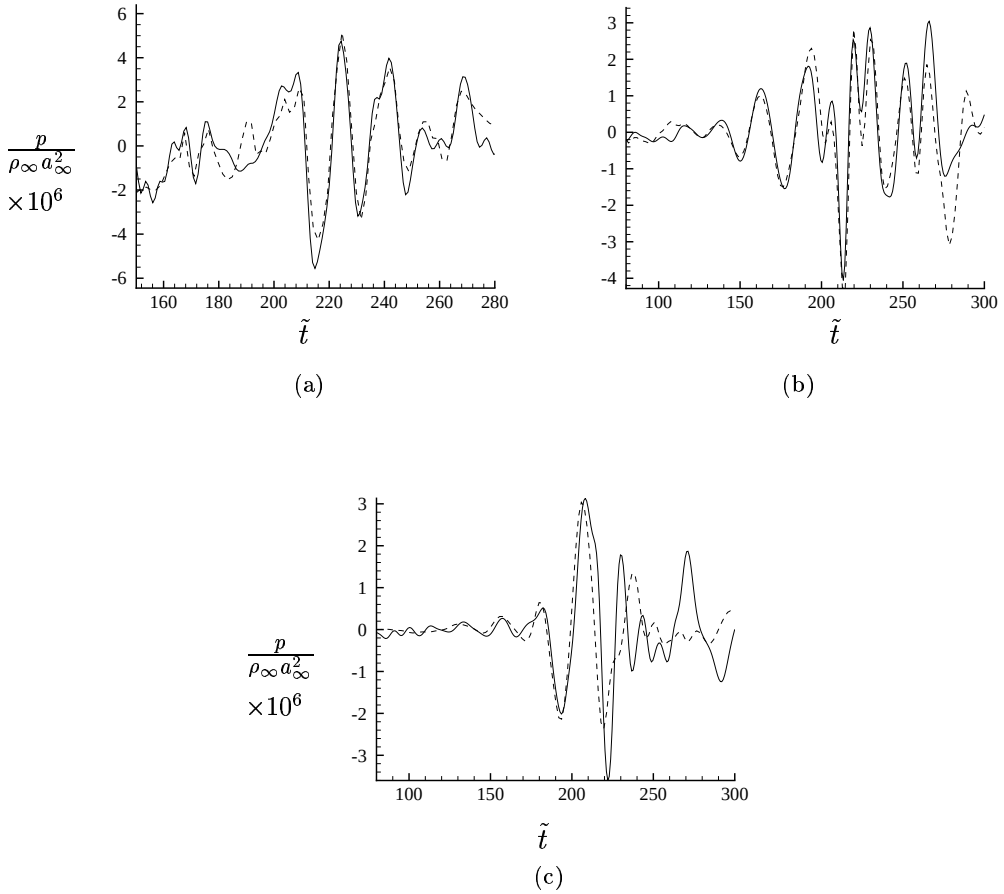

Figure 4.7: Pressure perturbation predicted with Möhring's formula at $|x| = 16.1R$, $\chi = 52°$ (——). DNS result (----). (a) $n = 1$, (b) $n = 2$, (c) $n = 3$.

core rotates with constant angular velocity,

$$\dot{\phi} = \frac{\Gamma}{\pi(a+b)^2} = \frac{\Omega\pi ab}{\pi(a+b)^2} = \frac{\Omega ab}{(a+b)^2}, \tag{4.13}$$

where a and b are the semi-major and semi-minor axes of the core cross section. Γ is the circulation of the ring, and ϕ is the angle between the major axis and the axis of symmetry of the vortex ring. When the aspect ratio is close to one, i.e. the core is nearly circular, the angular velocity is approximately $\Omega/4$.

The velocity of the vortex ring is

$$U(t) = \frac{\Gamma}{4\pi R}\left\{\ln\left(\frac{16\mathrm{R}}{\mathrm{a}+\mathrm{b}}\right) - \frac{1}{4} + \frac{3}{2}\frac{(\mathrm{a}-\mathrm{b})}{(\mathrm{a}+\mathrm{b})}\cos 2\phi\right\}. \tag{4.14}$$

Using Möhring's formula for the axisymmetric case, the acoustic source function become (Shariff et al. 1989)

$$\frac{d^3Q_0}{dt^3} = \frac{I}{\pi}\frac{d^2U}{dt^2}, \tag{4.15}$$

where I is the impulse of the ring, and finally

$$\frac{d^3Q_0}{dt^3} = -C\cos 2\phi, \tag{4.16}$$

$$C = \frac{3I^{\frac{1}{2}}\Gamma^{\frac{7}{2}}}{2\pi^{\frac{7}{3}}}\frac{(a-b)}{(a+b)^5}. \tag{4.17}$$

Therefore the frequency of the acoustic signal is twice the frequency of the core rotation, $\Omega/4\pi$, the same peak frequency of a turbulent vortex ring. However, this core rotation can not be sustained in real vortex ring with a peaked vorticity distribution. It tends to become nearly circular in just two eddy turnover time (Melander, McWilliams & Zabusky 1987). We propose that the turbulent vortex ring generates sound with a similar mechanism, however, the rotation of the core is in the form of concentrated vorticity region rotating around the core center, induced by the mean vorticity inside the core region. Figure 4.8 depicts the tangential velocity across the center of the vortex ring core at $\tilde{t} = 86.4$ and 172, the core region is between the two velocity peaks, and the induced velocity within the core is close to a solid body rotation. At $\tilde{t} = 172$, concentrated vorticity regions form at several spots in the

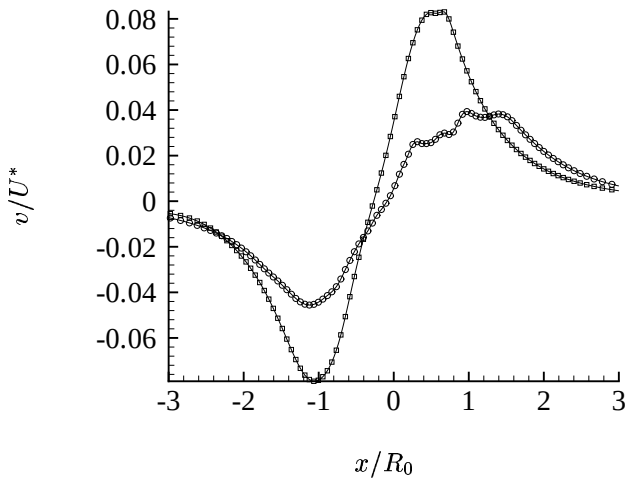

Figure 4.8: Tangential velocity v/U^* across the core at $\tilde{t} =$ (□) 86.4, (○) 172.

vortex ring, and begin to rotate around the core center with the induced angular velocity. Figures 4.9 and 4.10 plot the motion of vorticity inside the core during different stages. During laminar stage, the vorticity distribution is smooth and nearly steady, which results in nearly constant vorticity moments; during the nonlinear instability stage and transition stage, multiple vorticity peaks emerge and begin to rotate around the center of the core with angular velocity $\Omega/2$. The figures show qualitatively the unsteady dynamics of vortex patches in the vortex ring. However, further study is needed to quantitatively connect the vortex oscillations to the sound spectrum.

4.5 Asymptotic decay of the sound field

Another interesting phenomena is the temporal decay of the sound pressure level after the transition. Since the flow becomes self-similar and the vorticity field evolves with a similarity law, the acoustic field generated by the vorticity field would also follow a similarity law.

From Eq. (4.6), at a fixed position in space ($|x|$, χ), the pressure perturbation changes with $\frac{d^3}{dt^3}Q_{ij}(t - x/c_0)$. In addition, as shown in Eq. (3.13), during the turbulent stage there is a velocity scale u_s and a length scale $L_s = [\rho/I(\tilde{t} - \tilde{t}_0)]^{-1/4}$ upon which the flow is self-preserving.

Define nondimensional velocity $\boldsymbol{u}^* = \boldsymbol{u}/U_s$, $\boldsymbol{x}^* = \boldsymbol{x}/L_s$, which should be invariant in time, and then we get

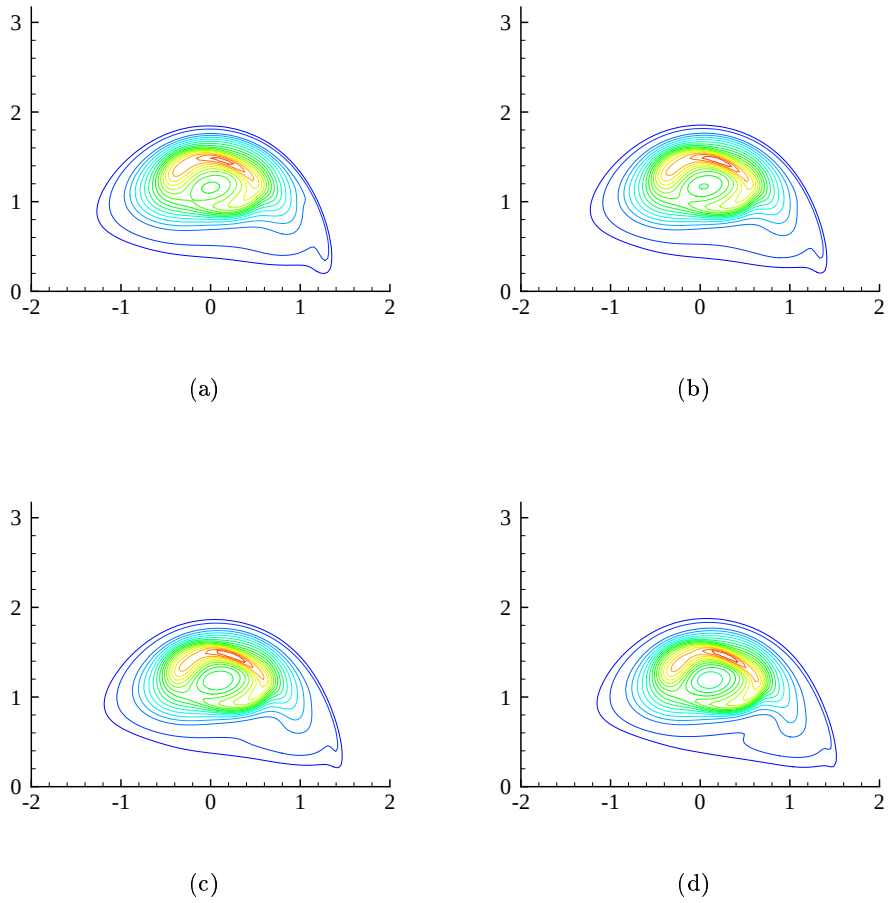

Figure 4.9: Azimuthal averaged vorticity contour at $\tilde{t} = 105$, 109, 112, 116, with 20 evenly spaced contours from 0.1 to 2.0.

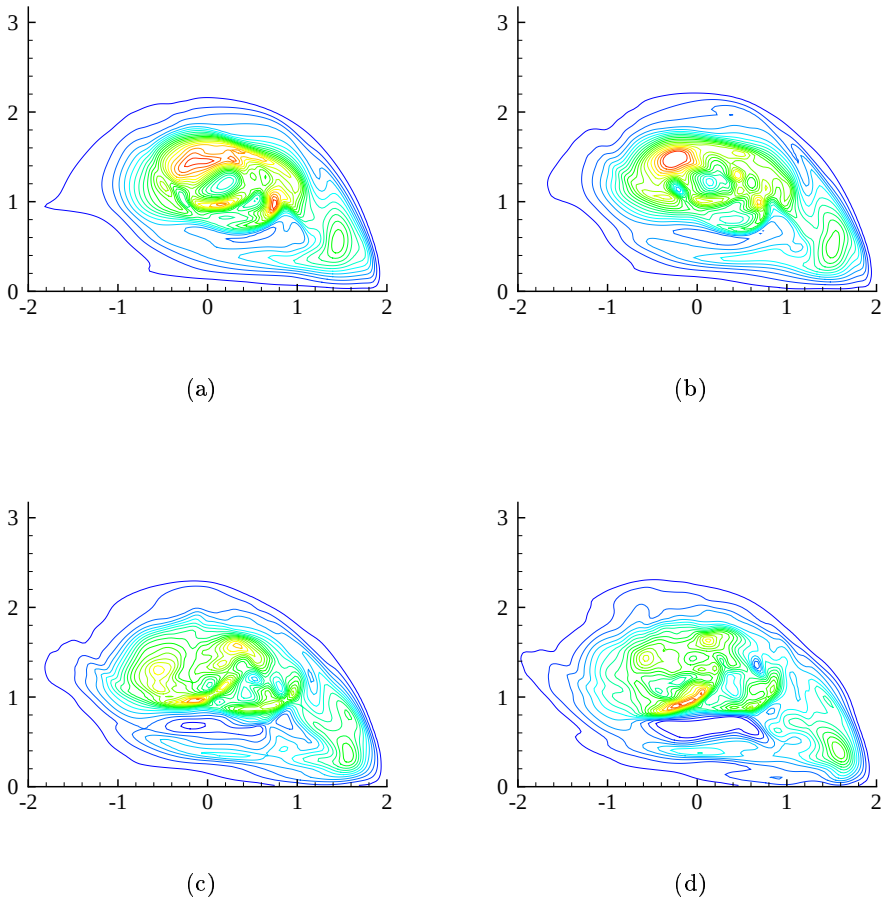

Figure 4.10: Azimuthal averaged vorticity contour at $\tilde{t} = 150$, 157, 166, 173, with 20 evenly spaced contours from 0.05 to 1.4.

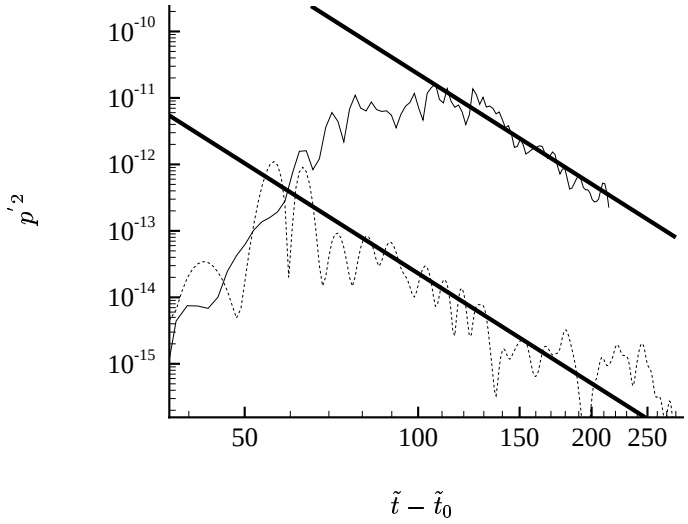

Figure 4.11: Decay of acoustic field at ($|x| = 15R_0$, $\chi = 37.2°$) (——) M=0.28, ensemble averaged ($N = 12$) (----) M=0.14, ensemble averaged ($N = 5$); (——) $p'^2 \sim (\tilde{t} - \tilde{t}_0)^{-\frac{11}{2}}$.

$$\boldsymbol{\omega} = \nabla \times \boldsymbol{u} = \frac{U_s}{L_s} \nabla^* \times \boldsymbol{u}^* = (t - t_0)^{-1} \boldsymbol{\omega}^*, \tag{4.18}$$

therefore

$$\begin{aligned} Q &= \int \big(\boldsymbol{x} \times \boldsymbol{\omega}(\boldsymbol{x}, t)\big)_i x_j dv = L_s^5 (t - t_0)^{-1} \int \big(\boldsymbol{x}^* \times \boldsymbol{\omega}^*(\boldsymbol{x}^*, t)\big)_i x_j^* dv^* \\ &= \big(\frac{I}{\rho}(t - t_0)^{-\frac{1}{4}}\big) \int \big(\boldsymbol{x}^* \times \boldsymbol{\omega}^*(\boldsymbol{x}^*, t)\big)_i x_j^* dv^*. \end{aligned} \tag{4.19}$$

Finally

$$\frac{d^3 Q}{dt^3} = (t - t_0)^{-\frac{11}{4}} \int \big(\boldsymbol{x}^* \times \boldsymbol{\omega}^*(\boldsymbol{x}^*, t)\big)_i x_j^* dv^*, \tag{4.20}$$

and

$$p'^2 \sim (\tilde{t} - \tilde{t}_0)^{-\frac{11}{2}} \tag{4.21}$$

Figure 4.11 presents the decay of p'^2 at point ($|x| = 15R_0$, $\chi = 37.2°$) for two Mach numbers $M = 0.14$ and 0.28. The agreement with the similarity scales is satisfactory.

4.6 Comparison with jet noise

In this section we try to compute the sound field generated by a train of de-correlated vortex rings, as a notional model of sound generation from coherent structures in a turbulent jet. For a single vortex ring, sound radiation is the strongest when the vortex ring breaks down and transitions. The vortex breakdown takes place at an approximately fixed downstream location of about 7 to 8 ring diameters, which is roughly the same location of the close of the potential core in a low Reynolds number jet. When a train of de-correlated vortex rings breaks down consecutively at the same location, the sound detected in the far field is the sum of each vortex ring sound field, with a delay time Δt between neighboring rings. We define a vortex ring replication Strouhal number $St_r = 2R/u_j\Delta t$, where u_j is the approximate exit jet velocity. A simple slug model predicts the translational velocity to be $U_{tr} = U_p/2$, where U_p is the piston velocity in the piston-cylinder mechanism, which is also the exit jet velocity from the cylinder. In practice, U_{tr} varied from $0.5U_p$ to $0.6U_p$, therefore the vortex rings with $M = 0.28$ correspond exit jet Mach number between 0.47 to 0.56. Analogously, this is the approximate convection velocity of a large scale structure in a jet with $U_{tr} = 0.5U_j$ to $0.6U_j$.

In the simulations, the reference frame moves with the vortex ring at a constant velocity, but in most jet noise experiments, the acoustic field is measured at fixed locations. For better comparison with jet noise measurement, we interpolate the data from the grid that is moving with speed M to a stationary grid. The sound pressure level at shallow angles will increase due to the translation of the vortex ring, whereas sound pressure level at downstream points will decrease. The frequency at downstream will also increase due to Doppler effect. Figure 4.12 demonstrates these effects at 3 points at $|x| = 60R$ and $\chi = 30°$, $60°$ and $90°$.

The pressure perturbations of 12 realizations are summed in random order with St_r varies from 0.08 to 0.4. Figure 4.13 depicts the replicated acoustic field with $St_r = 0.4$, 0.2 and 0.1. The total spectrum is plotted in Figure 4.14 for two polar angles $30°$ and $80°$. At $St_r = 0.4$, the pressure perturbation has the most overlap, therefore higher amplitude; whereas at $St_r < 0.1$, there is no overlap of pressure perturbation and the spectrum is the same as an individual vortex ring. Between 0.2 and 0.33, the spectrum is nearly invariant. On the other hand, the peak frequencies $St_j = 2fR/u_j$ are between 0.4 to 0.5, and are

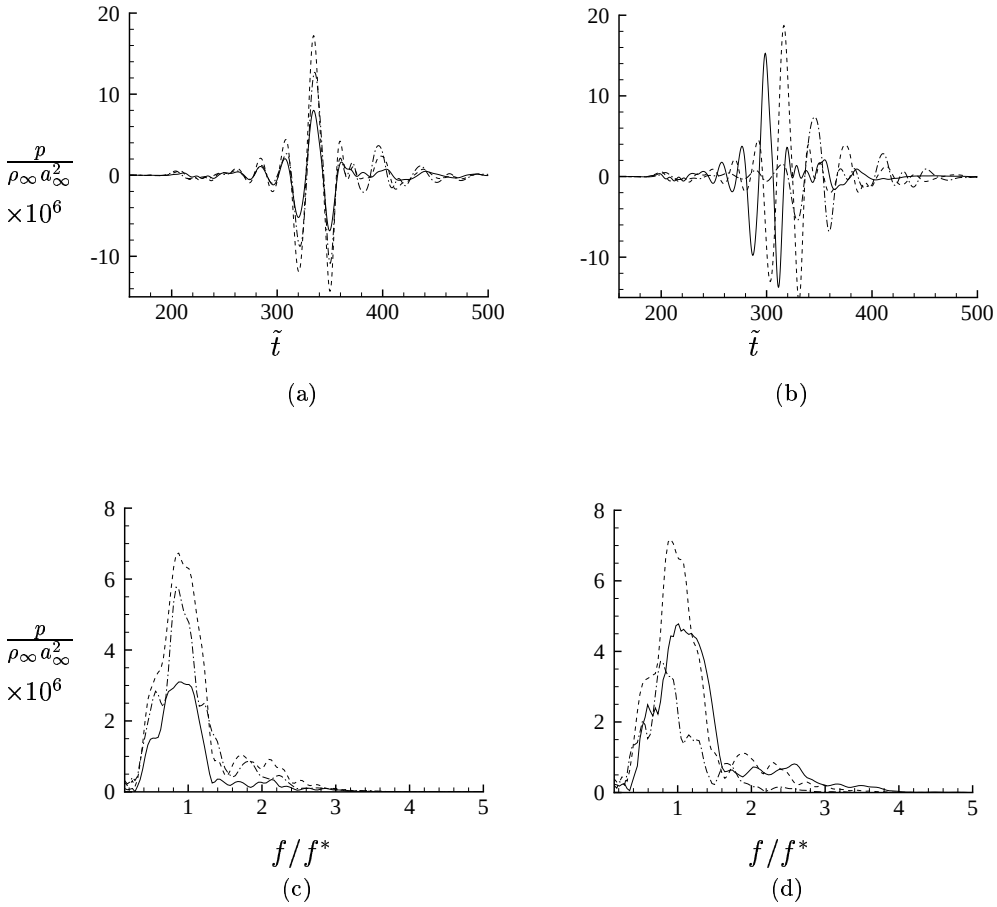

Figure 4.12: a) Pressure disturbance at 3 moving points at $|x| = 60R$; b) Pressure disturbance at 3 fixed points; c) spectrum at 3 moving points; d) spectrum at 3 fixed points. (——) $\chi = 30°$; (- - - -) $\chi = 60°$; (—·—) $\chi = 90°$.

independent of the replication frequency. The spectrum at $\chi = 30°$ from experimental data (Stromberg, McLaughlin & Troutt 1980) of a Mach 0.9 jet with a Reynolds number $Re_j = U_j D_j/\nu = 3600$ is overlaid on the spectrum in Figure 4.14 (a). The corresponding jet Reynolds number of the present vortex ring is 1900. The peak frequency of the jet noise is about 0.23, which is lower than the peak frequency of the vortex ring; however, the spectral shape at higher frequencies is quite similar between the jet and the train of vortex rings. In addition, the spectrum at $\chi = 80°$ is flatter than $\chi = 30°$, representing a larger contribution from higher frequency components.

To compare sound pressure level and directivity, the overall sound pressure level along a circle of $|x| = 15R$ for the sound field of a single vortex ring in moving frame, in stationary frame, and a train of vortex rings in stationary frame are depicted in Figure 4.15. The sound pressure level at shallow angle in the stationary frame is higher than the moving frame, but decays faster downstream. When the sound fields of a train of vortex rings are replicated, the overall sound pressure level increases by about 5dB. We compare it to the sound field of a subsonic jet measured by Lush (Lush 1971). The closest jet velocity in the experiments of Lush is 195 m/s, or Mach number 0.58. The SPL of the jet noise is scaled from the distance of 120 nozzle diameters to 7.5 diameters. At $\chi = 60°$, the sound pressure level of the train of vortex rings is about 4dB lower than the jet, likely due to slightly lower Mach number. To compare directivity, we plot the experimental data in Figure 4.15, with amplitude rescaled to agree with the train of vortex rings at 60°. The overall directivity patterns of the two curves are similar. A difference is that the sound radiation from the vortex rings is relatively stronger near the axis, and weaker at angle between 20° to 40^0. In jet noise, the sound propagating at shallow angles is refracted to larger angles, thus increasing the sound pressure level in this region. The steeper fall off in directivity for $\chi > 60°$ in the simulation is probably a low Reynolds number effect and is similar to that observed in jet experiments (Stromberg et al. 1980) and simulations at low Re (Freund 2001). The directivity of jet with Mach number 0.9 (Stromberg et al. 1980) is also plotted, with the sound pressure level scaled by $(0.9/0.54)^4$. The directivities of the jet and the train of vortex rings are nearly identical at angles higher than 60^o. However, at 30^o, the difference is about 8 dB. The difference is due to two factors: the first factor is the convective amplification, which is $(1 - M\cos\chi)^{-6}$ for compact source and $(1 - M\cos\chi)^{-5}$ for jet. For vortex ring with convection Mach number 0.28, convective amplification leads to

3.3 dB of increase from 60^o to 30^o, whereas for a jet with source convection Mach number 0.45, it leads to 5.2 dB of increase from 60^o to 30^o. A more important factor is the sound generated by the roll-up of vortices due to jet instabilities, and the interactions between these vortices upstream of the close of potential core. This component of the sound field has peak Strouhal number of about 0.2 and 0.3, and is large at shallow angles and decays fast at higher angles. This sound generation process is not captured with the de-correlated train of vortex rings, therefore the difference in SPL is larger at shallow angles and smaller at higher angles.

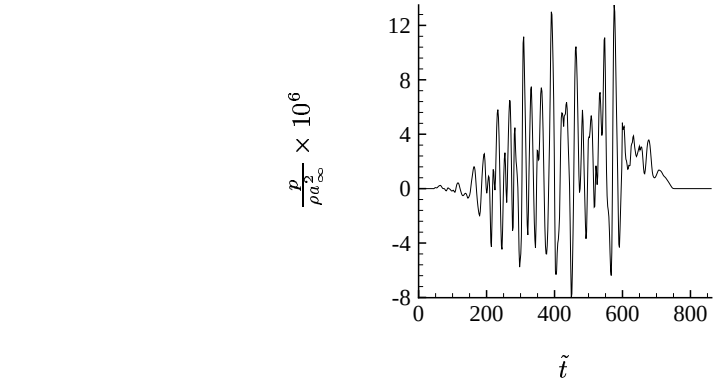

(a)

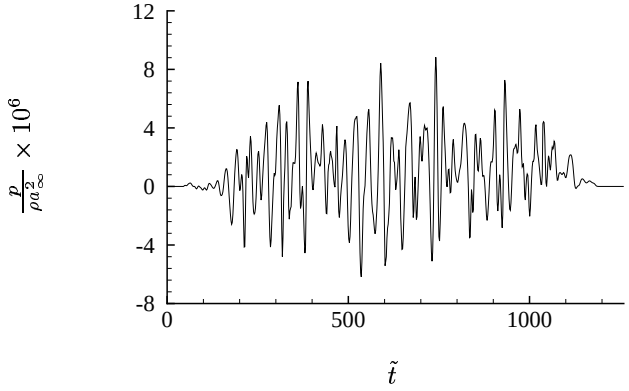

(b)

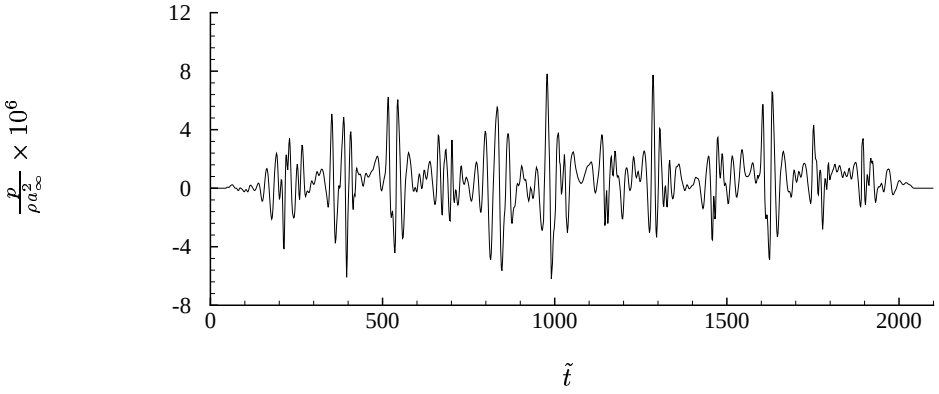

(c)

Figure 4.13: Acoustic field of a train of de-correlated vortex rings at $|x| = 60R$, $\chi = 30°$, (a) $St_r = 0.4$, (b) $St_r = 0.2$, (c) $St_r = 0.1$.

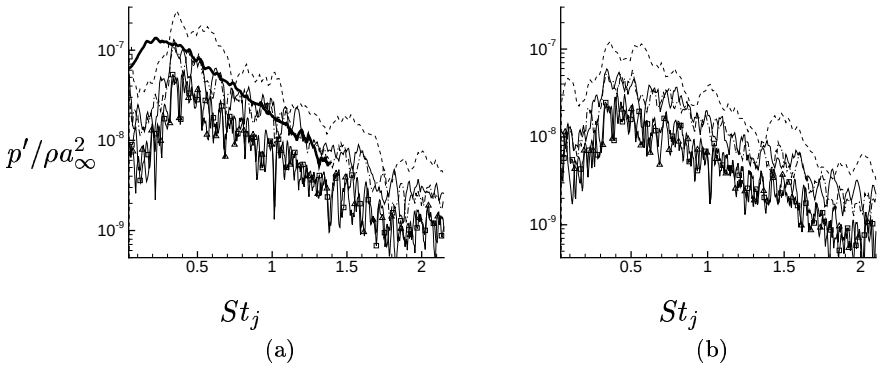

Figure 4.14: Spectrum of replicated vortex rings at $|x| = 60R$, (a) $\chi = 30°$, (b) $\chi = 80°$ (----) $St_r = 0.4$; (——) $St_r = 0.2$; (—·—) $St_r = 0.13$; (□) $St_r = 0.1$; (△) $St_r = 0.08$, (▬▬) from the experiment (Stromberg et al. 1980).

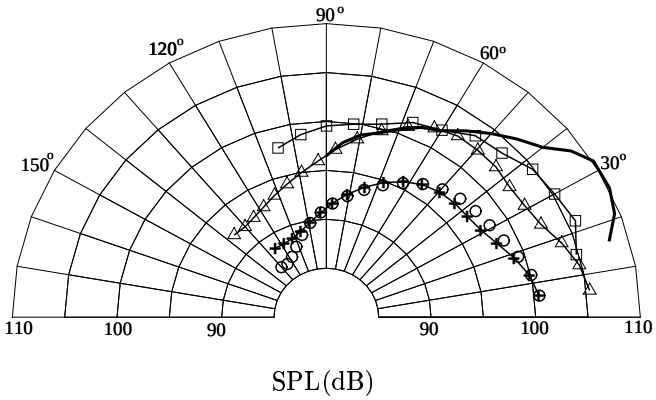

Figure 4.15: Polar distribution of total sound pressure level. (+) turbulent vortex ring with translational Mach number M=0.28 along a circle of $|x| = 15R$ moving with the vortex ring, (∘) along a stationary circle; (△), a train of de-correlated vortex rings with $St_r = 0.2$; (∘) experimental data (Lush 1971) for a subsonic jet with jet Mach number 0.58 scaled to agree with the train of vortex rings at 60^o, (——) experimental data (Stromberg et al. 1980), scaled with M^4.

Chapter 5

Conclusions and Future Work

We have computed transition and turbulent decay of an initially laminar vortex ring together with its radiated acoustic field. This is the first known numerical simulation of turbulent vortex ring and its acoustic field. Large number of realizations is computed to get accurate ensemble averaged mean flow properties and turbulent statistics. Detailed information on acoustic source is obtained.

After an initial transient, instabilities with specific azimuthal mode numbers (primarily $n = 6$ and $n = 7$) and a particular radial structure grow most rapidly, in accord with linear stability theory (Widnall & Tsai 1977). The growth rate of the unstable modes is dependent on Reynolds number. The mode shapes of each azimuthal modes are illustrated.

During later stages, nonlinear interactions excite harmonics of the most linearly amplified waves. The harmonics have larger growth rate and accelerate the vortex ring deformation. The initially smooth vorticity distribution developed sharp peaks inside the core and the Reynolds stresses increase rapidly. The mode interactions also bring about significant growth of the lower azimuthal modes (n = 0, 1, and 2). These modes are more efficient in turbulent mixing because they induce higher Biot-Savart velocity outside of the vortex ring core. During this stage, an axial flow is developed due to the uneven growth of waves around the ring. In addition, the three-dimensional instabilities produce streamwise vorticity, and some of the vorticity is elongated near the centerline and shed into the wake. Eventually the vortex ring breaks down and the turbulence decays due to cancellation of vorticity with opposite sign. The circulation of the vortex ring decays linearly in time, and the translational velocity decays in a stair-like fashion.

We documented all three components of normal Reynolds stresses. The azimuthal Reynolds stress (which is missing from previous studies) arises from the axial flow, and

its amplitude is of the same level as the other two components, suggesting that the turbulent field is nearly isotropic. The ensemble averaged turbulence production terms are also computed. We found that the production is stronger at the front region of the core, where vortex stretching is large. The major contribution is from the axial normal Reynolds stress and the shearing Reynolds stress. During turbulent decay, the flow properties become independent of viscosity and initial geometry of the vortex ring, and only depend on the total impulse of the flow. We can define a new velocity scale and a length scale, both functions of time, and find a good collapse of the azimuthally and ensemble-averaged velocity fields with the self-similar theory (Glezer & Coles 1990). From self-similarity, the velocity field decays with $\tilde{t}^{-3/4}$.

The acoustic field is solved together with the flow field, and is extended to the far field by solving a wave equation. Statistics and spectra of the sound field are gathered for an ensemble of 12 realizations. The sound field is dominated by azimuthal modes $n = 0$, 1 and 2 (which are the only radiating modes if the noise source is compact) that develops during the nonlinear stage of vortex ring instability. The evolution of sound pressure level follows the growth of these modes, and reaches a peak value when the modes saturate and the vortex begins to break down. Vortex sound theory predicts that for a vortex ring with low Mach number, the directivity of the first three azimuthal modes are $(3\cos^2\chi - 1)^2$, $\sin^2 2\chi$, and $\sin^4\chi$, respectively, where χ is the polar angle. However, since the vortex ring translates with finite Mach number, the acoustic field is adjusted by a convective amplification factor $(1 - \mathrm{M}\cos\chi)^{-3}$, which causes the acoustic field to be intensified at downstream direction. When we account for the convective amplification, the directivity of these modes agrees well with predictions of vortex sound theory. If a flow system consists of only axisymmetric vortices, the acoustic field directivity will be dominated by $(3\cos^2\chi - 1)^2$, which, unlike jet noise, has an extinction angle around 50°. On the other hand, for a turbulent vortex ring, all the azimuthal modes contribute to the directivity, and the overall directivity become more monotonic.

The spectra are peaked at a frequency that corresponds to $4\pi f/\Omega_0 = 1.0$, in agreement with experiments (Zaitsev et al. 1990). The rotation rate is half of the mean vorticity Ω_0. The theory of Kopiev & Chernyshev (1997) connects this frequency with linear eigenoscillations of a thin-cored vortex ring. Shariff et al. (1989) demonstrated that an axisymmetric vortex ring with elliptic core will radiate at the same frequency due to the rotation

of the vortex boundary. We found that at late nonlinear stage, concentrated vorticity regions form in the core, and rotate around the center with angular velocity induced by the mean vorticity. We conjecture that motion of the irregular vorticity leads to fluctuation of vorticity moments in Möhring's equation, and radiates sound with the specific frequency.

Based on the theory for self-similar decay of the near field, we use vortex sound theory to determine the decay rate for the acoustic field. The sound pressure level is found to decay with $\tilde{t}^{-\frac{11}{2}}$. Simulation results at two different Mach numbers 0.14 and 0.28 confirm the scaling.

Finally, we compare sound radiated by the vortex ring to jet noise. We heuristically model the jet as a de-correlated train of vortex rings with a fixed replication frequency. To compare frequencies between the ring and jet, we assume that the ring translates with a convection speed corresponding to $0.5U_j$ to $0.6U_j$. We find that the directivity and shape of the noise spectrum is nearly invariant to replication frequencies around the range $St = 0.2$ to $St = 0.3$, which corresponds to the frequency of peak amplification of linear instability waves to the jet mean flow field. The primary effect of replication is to enhance SPL by about 5 dB.

The peak frequency of the single vortex ring is preserved in the train of rings. It corresponds to about $St = 0.4$, which is somewhat higher than the peak frequency of jet noise, especially at low Mach and Reynolds numbers. Nevertheless, the spectral shape at higher frequencies is quite similar to low Reynolds number experiments (Stromberg et al. 1980) for a M=0.9 jet. The directivity also shows substantial agreement with jet noise data. The sound pressure level (of the replicated ring) is within about 4 dB of a higher-Reynolds number jet(Lush 1971) with a slightly higher Mach number than our simulations. The directivity is nearly identical with jet noise data with similar Reynolds numbers (Stromberg et al. 1980) at higher polar angle.

In future work we plan to further explore the connections between vortex ring and jet noise. The train of de-correlated rings appears to capture the main features of the low-Reynolds number acoustic field *except* perhaps the sound radiated by instabilities of the mean jet profile that lead to vortex roll-up upstream of the close of the potential core and the peak frequency with $St = 0.2$ to 0.3. However, once formed, the vortex ring instabilities and breakdown may be reasonable models of the sound generation toward the close of the potential core. An intriguing possibility is that excitation of higher azimuthal modes in

a jet (say with chevron nozzles) amplifies the most unstable modes (say with n = 6-7) of vortices that are formed by the instabilities of the mean jet profile. This may lead to more rapid breakdown of the vorticity toward the close of the potential core in a process similar to that observed for the present isolated vortex ring.

Appendix A

Comparison of nonimpulsive forcing with the cylinder/piston mechanism

Here it is shown that the long duration forces discussed in Section 2.4.1 produce a flow which is very similar to flow produced by pushing a column of fluid through an orifice. Didden (1979) found that for short times, the trajectory of the leading vortex ring follows $x_c \sim t^{3/2}$ (up to a stroke length $L/D = 0.6$), and this result was confirmed in previous computations, which attempted to model the roll up of the vortex sheet explicitly (Nitsche & Kransy 1994), and which specified an inlet velocity profile (James & Madnia 1996). In order to demonstrate the similarity of the present generation mechanism to the cylinder/piston mechanism, we plot in Figure A.1 the trajectory of the leading vortex ring as the duration of the non-impulsive forcing is varied from $TC/R^2 = 1.58$ to 25.3. For early times, the $t^{3/2}$ behavior is also obtained for generation by nonconservative force. After the forcing is turned off, the ring translates at nearly steady velocity $x_c \sim t$.

The axial velocity profile at the center of the forcing region is plotted in figure A.2, at several instances during and slightly after the forcing. These plots are typical of all our runs with long duration forces. Comparing these to similar plots from previous computations and experiments (James & Madnia 1996, Nitsche & Kransy 1994, Didden 1979), it is evident that the nonconservative forcing produces an axial velocity profile that has the same qualitative features as those measured at the discharge plane in the cylinder/piston mechanism.

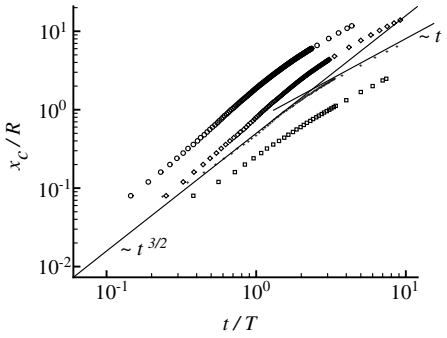

Figure A.1: Distance of the vortex center from the forcing location for different duration of forces. Case 1, $TC/R^2 = 1.58$ (□); Case 2, $TC/R^2 = 4.05$ (+); Case $TC/R^2 = 3$, 9.11 (◇); Case 4, $TC/R^2 = 25.3$ (○).

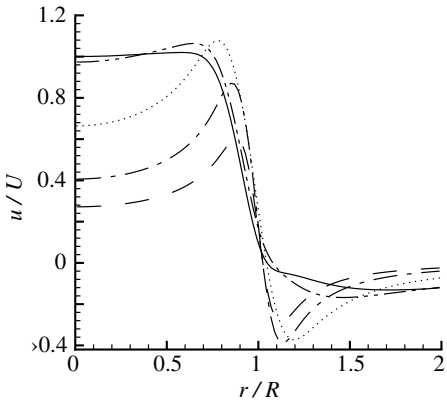

Figure A.2: Axial velocity at the center of the forcing region. $tC/R^2 = 8.86$ (– – – –); $tC/R^2 = 11.4$ (—·—); $tC/R^2 = 16.4$ (·····); $tC/R^2 = 26.6$ (—··—); $tC/R^2 = 31.6$ (——). The velocity is normalized with the maximum axial velocity at time $tC/R^2 = 31.6$.

Bibliography

Akhmetov, D. (1980), 'Extinguishing gas and oil well fires by means of vortex rings', *Combust. Explos. Shock Waves* **16**, 490–494.

Auerbach, D. (1990), 'Stirring properties of vortex rings', *Phys. Fluids* **3**(5), 1351–1355.

Bayliss, A. & Turkel, E. (1982), 'Radiation boundary conditions for wave-like equations', *Comm. Pure and Appl. Math* **33**, 707–725.

Bridges, J. & Hussain, F. (1992), 'Direct evaluation of aeroacoustic theory in a jet', *J. Fluid Mech.* **240**, 469–501.

Brown, G. & Roshko, A. (1974), 'On density effect and large structure in turbulent mixing layers', *J. Fluid. Mech.* **64**, 775–816.

Chahine, G. & Genoux, P. (1983), 'Colapse of a cavitating vortex ring', *J. Fluid Mech.* **105**, 400–405.

Colonius, T. (2004), 'Modeling artificial boundary conditions for compressible flow', *Ann. Rev. Fluid Mech.* **36**, 315–345.

Colonius, T., Lele, S. & Moin, P. (1993), 'Boundary conditions for direct computation of aerodynamic sound generation', *AIAA J.* **31**(9), 1126–1133.

Colonius, T., Lele, S. & Moin, P. (1997), 'Sound generation in a mixing layer', *J. Fluid Mech.* **330**, 375–409.

Colonius, T. & Ran, H. (2002), 'A super-grid-scale model for simulating compressible flow on unbounded domains', *J. Comput. Phys.* **182**(1), 191–212.

Constantinescu, G. & Lele, S. (2002), 'A highly accurate technique for the treatment of flow equations at the polar axis in cylindrical coordinates using series expansions', *J. Comput. Phys.* **182**(1), 165–186.

Crighton, D. & Huerre, P. (1990), 'Shear-layer pressure fluctuations and superdirective acoustic sources', *J. Fluid Mech.* **220**, 355–368.

Crow, S. (1970), 'Aerodynamics sound emission as a singular perturbation problem', *Stud. Appl. Maths.* **49**, 21–44.

Crow, S. C. & Champagne, F. (1971), 'Orderly structure in jet turbulence', *J. Fluid. Mech.* **48**, 547–591.

Didden, N. (1979), 'On the formation of vortex rings: Rolling-up and production of circulation', *Z. Angew. Mech. Phys.* **30**, 101–116.

Dyke, M. V. (1982), *An Album of Fluid Motion*, Parabolic, Stanford, CA.

Engquist, B. & Majda, A. (1979), 'Radiation boundary conditions for acoustic and elastic wave calculations', *Comm. Pure and Appl. Math* **32**, 313–357.

FfowcsWilliams, J. E. (1963), 'The noise from turbulence convected at high-speed', *J. Fluid. Mech.* **21**, 641–657.

Freund, J. (1997), 'Proposed inflow/outflow boundary condition for direct computation of aerodynamic sound', *AIAA J.* **35**(4), 740–742.

Freund, J. (2001), 'Noise sources in a low-reynolds-number turbulent jet at mach 0.9', *J. Fluid Mech.* **438**, 277–305.

Freund, J., Lele, S. & Moin, P. (1997), Compressibility effects in turbulent annular mixing layer, Technical Report TF-72, Dept. Mech. Eng., Stanford University.

Giles, M. (1990), 'Nonreflecting boundary-conditions for euler equation calculations', *AIAA J.* **28**(12), 2050–2058.

Givoli, D. (1991), 'Non-reflecting boundary conditions', *J. Comp. Phys.* **94**(1), 1–29.

Glezer, A. (1988), 'The formation of vortex rings', *Phys. Fluids* **31**, 3532–3541.

Glezer, A. & Coles, D. (1990), 'An experimental study of a turbulent vortex ring', *J. Fluid Mech.* **211**, 243–283.

Howe, M. (1975), 'Contribution to the theory of aerodynamic sound, with application to excess jet noise and the theory of the flute', *J. Fluid Mech.* **71**, 625–673.

Hu, F. Q. (1996), 'On absorbing boundary conditions for linearized euler equations by a perfectly matched layer', *J. Comput. Phys.* **129**(1), 201–219.

Huang, W. & Sloan, D. (1993), 'Pole conditions for singular problems: the pseudospectral approximation', *J. Comp. Phys.* **107**, 254–261.

James, S. & Madnia, C. (1996), 'Direct numerical simulation of a laminar vortex ring', *Phys. Fluids* **8**, 2400–2414.

Johnson, G. (1970), Researches on the propagation and decay of vortex rings, ARL Rep. 70-0093, Aerospace Res. Labs., Wright-Patterson Air Force Base, Ohio.

Kambe, T. (1986), 'Acoustic emissions by vortex motions', *J. Fluid Mech.* **173**, 643–666.

Kambe, T. & Minota, T. (1981), 'Sound radiation from vortex systems', *J. Sound Vib.* **74**, 61–72.

Kambe, T. & Minota, T. (1983), 'Acoustic wave radiated by head-on collision of two vortex rings', *Proc. R. Soc. London Ser. A* **386**, 277–308.

Kelvin, L. (1867*a*), 'On vortex atoms', *Phil. Mag.* **34**, 15–24.

Kelvin, L. (1867*b*), 'The translatory velocity of a circular vortex ring', *Phil. Mag.* **33**, 511–512.

Kibens, V. (1979), 'Discrete noise spectrum generated by an acoustically excited jet', *AIAA J.* **18**, 434–441.

Knio, O. & Ghoniem, A. (1990), 'Numerical study of a three-dimensional vortex method', *J. Comp. Physics* **86**, 75–106.

Kopiev, V. & Chernyshev, S. (1997), 'Vortex ring eigen-oscillations as a source of sound', *J. Fluid Mech.* **341**, 19–57.

Kovasznay, L., Fujita, H. & Lee, R. (1973), 'Unsteady turbulent puffs', *Adv. Geophys.* **18B**, 253–263.

Krueger, P. & Gharib, M. (2003), 'The significance of vortex ring formation to the impulse and thrust of a starting jet', *Phys. Fluids* **15**(5), 1271–1281.

Küchemann, D. (1965), 'Report on the i.u.t.a.m. symposium on concentrated vortex motions in fluids', *J. Fluid Mech.* **21**, 1–20.

Laufer, J. & Yen, T. (1983), 'Noise generation by a low-mach-number jet', *J. Fluid Mech.* **134**, 1–31.

Lele, S. K. (1992), 'Compact finite difference schemes with spectral-like resolution', *J. Comp. Physics* **103**(1), 16–42.

Lighthill, M. (1952), 'On sound generated aerodynamically i. general theory', *Proc. Roy. Soc. Lond. Ser. A* **211**, 564–587.

Lighthill, M. (1954), 'On sound generated aerodynamically ii. turbulence as a source of sound', *Proc. Roy. Soc. Lond. Ser. A* **222**, 1–32.

Lugt, H. (1983), *Vortex Flow in Nature and Technology*, Wiley-Interscience, New York.

Lundgren, T. & Mansour, N. (1991), 'Vortex ring bubbles', *J. Fluid Mech.* **224**, 177–196.

Lundgren, T., Yao, J. & Mansour, N. (1992), 'Microburst modeling and scaling', *J. Fluid Mech.* **239**, 461–488.

Lush, P. (1971), 'Measurement of subsonic jet noise and comparison with theory', *J. Fluid Mech.* **46**(3), 477–500.

Mankdabi, R. & Liu, J. T. C. (1984), 'Sound generated aerodynamically revisited: Large-scale structures in a turbulent jet as a source of sound', *Phil. Trans. R. Soc. Lond. A* **311**, 183–217.

Maxworthy, T. (1972), 'The structure and stability of vortex rings', *J. Fluid Mech.* **51**, 15–32.

Maxworthy, T. (1974), 'Turbulent vortex rings', *J. Fluid Mech.* **64**, 227–239.

Maxworthy, T. (1977), 'Some experimental studies of vortex rings', *J. Fluid Mech.* **81**, 465–495.

McCormack, P. & Crane, L. (1973), *Physical Fluid Dynamics*, Academic Press, New York.

Melander, M., McWilliams, J. & Zabusky, N. (1987), 'Axisymmetrization and vorticity gradient intensification of an isolated two-dimensional vortex through intensification', *J. Fluid Mech.* **178**, 137–159.

Mitchell, B., Lele, S. & Moin, P. (1995), Direct computation of the sound generated by subsonic and supersonic axisymmetric jets, Technical Report TF-66, Dept. Mech. Eng., Stanford University.

Mitchell, B., Lele, S. & Moin, P. (1999), 'Direct computation of the sound generated by vortex pairing in an axisymmetric jet', *J. Fluid Mech.* **383**, 113–142.

Möhring, W. (1978), 'On vortex sound at low mach number', *J. Fluid Mech.* **85**, 685–691.

Mohseni, K. & Colonius, T. (2000), 'Numerical treatment of polar coordinate singularities', *J. Comp. Phys* **157**, 787–795.

Mohseni, K., Ran, H. & Colonius, T. (2001), 'Numerical experiments on vortex ring formation', *J. Fluid Mech.* **430**, 267–282.

Moore, C. (1977), 'The role of shear-layer instability in jet exhaust noise', *J. Fluid Mech.* **80**, 321–367.

Moore, D. (1980), 'The velocity of a vortex ring with a thin core of elliptical cross section', *Proc. R. Soc. Lond. A* **370**, 407–415.

Moore, D. & Saffman, P. (1975), 'The instability of a straight vortex filament in a strain field', *Proc. R. Soc. London Ser. A* **346**, 413–25.

Müller, E. & Obermeier, F. (1988), 'Vortex sound', *Fluid Dyn. Res.* **3**, 43–51.

Nitsche, M. & Kransy, R. (1994), 'A numerical study of vortex ring formation at the edge of a circular tube', *J. Fluid Mech.* **276**, 139–161.

Norbury, J. (1973), 'A family of steady vortex rings', *J. Fluid Mech.* **57**, 417–431.

Obermeier, F. (1985), 'The influence of solid bodies on low mach number vortex sound', *J. Sound Vib.* **72**, 39–49.

Rayfield, G. & Reif, G. (1963), 'Evidence for teh creation and motion of quantized vortex rings in superfluid helium', *Phys. Rev. Lett.* **11**, 305–308.

Rivoalen, E., Huberson, S. & Knio, O. (2003), 'Numerical study of sound radiated by axisymmetric vortex rings', *J. of Comp. Acoustics* **11**(1), 11–45.

Rogers, W. (1958), 'On the formation of rotating rings by air and liquids under certain conditions of discharge', *Am. J. Sci. Arts (Second Ser.)* **26**, 246–258.

Rosenfeld, M., Rambod, E. & Gharib, M. (1998), 'Circulation and formation number of laminar vortex rings', *J. Fluid Mech.* **376**, 297–318.

Rowley, C. & Colonius, T. (2000), 'Discretely nonreflecting boundary conditions for linear hyperbolic systems', *J. Comput. Phys.* **157**, 500–538.

Saffman, P. (1970), 'The velocity of viscous vortex rings', *Stud. Appl. Math.* **49**, 371–80.

Saffman, P. (1978), 'The number of waves on unstable vortex rings', *J. Fluid Mech.* **84**, 625–639.

Saffman, P. (1981), 'Dynamics of vorticity', *J. Fluid Mech.* **106**, 49–58.

Saffman, P. (1992), *Vortex Dynamics*, Cambridge University Press.

Seiner, J. & Krejsa, E. (1989), 'Supersonic jet noise and the high speed civil transport', *AIAA paper* (89-2358).

Shariff, K. & Leonard, A. (1992), 'Vortex rings', *Ann. Rev. Fluid Mech.* **34**, 235–279.

Shariff, K., Leonard, A. & Ferziger, J. (1989), Dynamics of a class of vortex rings, NASA TM 102257, NASA.

Shariff, K., Verzicco, R. & Orlandi, P. (1994), 'A numerical study of the three-dimensional vortex ring instabilities: viscous corrections and early nonlinear stage', *J. Fluid Mech.* **279**, 351–375.

Stanaway, S. & Cantwell, B. (1988), A numerical study of viscous vortex rings using a spectral method, NASA TM 101041, NASA.

Stromberg, J., McLaughlin, D. & Troutt, T. (1980), 'Flow field and acoustic properties of a mach number 0.9 jet at a low reynolds number', *J. Sound Vib.* **72**, 159–176.

Swearingen, J., Crouch, J. & Handler, R. (1995), 'Dynamics and stability of a vortex ring impacting a solid boundary', *J. Fluid Mech.* **297**, 1–28.

Tam, C. (1995), 'Supersonic jet noise', *Annu. Rev. Fluid Mech.* **27**, 17–43.

Tam, C. & Auriault, L. (1999), 'Jet mixing noise from fine-scale turbulence', *AIAA Journal* **37**(2), 145–153.

Tam, C. & Chen, P. (1994), 'Turbulent mixing noise from supersonic jets', *AIAA J.* **32**, 1774–1780.

Tam, C., Golebiowski, M. & Seiner, J. (1996), 'On the two components of turbulent mixing layers', *AIAA paper* (96-1716).

Tam, C. & Webb, J. (1993), 'Dispersion-relation-preserving finite difference schemes for computational acoustics', *J. Comput. Phys.* **107**, 262–281.

Tang, S. & Ko, N. (2000), 'Sound sources in the interactions of two inviscid two-dimensional vortex pairs', *J. Fluid Mech.* **419**, 117–201.

Tang, S. & Ko, N. (2003), 'Basic sound generation mechanisms in inviscid vortex interactions at low mach number', *J. Sound Vib.* **262**(1), 87–115.

Thompson, K. (1987), 'Time dependent boundary conditions for hyperbolic systems', *J. Comp. Phys.* **68**, 1–24.

Thompson, P. (1991), *Compressible Fluid Dynamics*, McGraw-Hill.

Tsynkov, S. (1998), 'Numerical solution of problems on unbounded domains, a review', *Appl. Numer. Math* **27**(4), 465–532.

Turner, J. (1957), 'Buoyant vortex rings', *Proc. R. Soc. London Ser. A* **239**, 61–79.

Verzicco, R., Orlandi, P., Eisenga, A., van Heijst, G. & Carnevale, G. (1996), 'Dynamics of a vortex ring in a rotating fluid', *J. Fluid Mech.* **317**, 215–239.

Weigand, A. & Gharib, M. (1994), 'On the decay of a turbulent vortex ring', *Phys. Fluids* **6**(12), 3806–3808.

Weigand, A. & Gharib, M. (1997), 'On the evolution of laminar vortex rings', *Experiments in Fluids* **22**, 447–457.

Widnall, S., Bliss, D. & Tsai, C. (1974), 'The instability of short waves on a vortex rings', *J. Fluid Mech.* **66**, 35–47.

Widnall, S. & Sullivan, J. (1973), 'On the stability of vortex rings', *Proc. R. Soc. London Ser. A* **332**, 335–353.

Widnall, S. & Tsai, C. (1977), 'The instability of the thin vortex rings of constant vorticity', *Phil. Trans. R. Soc. London A* **287**, 273–305.

Winant, C. & Broward, F. (1974), 'Vortex paring: The mechanism of turbulent mixing layers growth at moderate reynolds number', *J. Fluid. Mech.* **63**, 237–255.

Yuan, H. (1973), Ph.d. thesis, California Institute of Technology.

Zaitsev, M., Kopiev, V. & Kotova, A. (2001), 'Representation of the sound field of a turbulent vortex ring as a superposition of quadrupoles', *Acoustical Physics* **47**(6), 793–801.

Zaitsev, M., Kopiev, V., Munin, A. & Potokin, A. (1990), 'Sound radiation by a turbulent vortex ring', *Sov. Phys. Dolk.* **35**, 488–489.